Development of a novel gerotor pump
For lubrication systems of aeronautic engines

By

Andrea De Martin

******

Supervisor(s):
Prof. M. Sorli,Supervisor
Prof. G. Jacazio, Co-Supervisor

Politecnico di Torino
2017

Declaration

I hereby declare that, the contents and organization of this dissertation constitute my own original work and does not compromise in any way the rights of third parties, including those relating to the security of personal data.

Andrea De Martin

2017

* This dissertation is presented in partial fulfillment of the requirements for **Ph.D. degree** in the Graduate School of Politecnico di Torino (ScuDo).

To my lil' brother, keep up with the good work!

Acknowledgment

Abstract

The technology of lubrication systems for aircrafts engines has seen significant development during the history of aeronautics and has progressed in parallel with the evolution of the engines themselves. Starting from the first, wet-sump schemes derived from automotive applications, more complex systems and components have been introduced. The progressive increase of aeronautic engines' power and speed, as well as that of the maximum operative altitude of the aircraft, have increased the lubricant flow rate required to avoid severe mechanical issues that can cause dangerous conditions for the vehicle and its users. Currently, the main focus on the development of novel lubrication pumps is aimed at reducing the pumps' weight and envelope while maintaining, or possibly increasing, their reliability. The first two objective could be pursued by searching for novel pump types and/or increasing the pump speed in order to downsize its required capacity, but the low-pressure environment, typical of the lubrication circuits, over imposes a few, severe, limitations to avoid cavitation occurrence that decrease the effectiveness of this approach.

The central aim of the presented research, performed within the program "Greening the Propulsion", is to provide a theoretical framework to help in the development of a novel gerotor pump for the lubrication of aeronautic engines. The first step of the research involves the study of the state of the art of aeronautic engines' lubrication systems, providing particular care to the effect that any design choice and possible operational condition may have on the lubrication pump design. Hence, the state of the art for gerotor pumps is investigated; results of this study are used, along with catalogue comparisons, to build simplified sizing tools to perform a benchmarking activity involving gerotors and other low-pressure pumps type. This activity, performed to position gerotor pumps in the aeronautic engine lubrication market, is then used as a starting point to highlight the weak points of gerotors traditional design and to propose some possible solutions to enhance the pumps performances. To study the outcomes of these modifications, a rigorous theoretical framework is required; sizing and modeling criteria, based on the theory of gearing and compressible fluids, are hence detailed

and used to build an Automatic Design and Simulation Framework, able to automatically design, validate and simulate a novel gerotor pump given a minimum number of geometrical and physical input parameters. This design and simulation tool is then used to evaluate the performance boost provided by the proposed variations and to optimize the gears profiles by pairing it with a multi-objective algorithm based on evolutionary strategies.

Another critical component of any lubrication system is the pressure relief valve used to avoid the occurrence of dangerous conditions for the pipes integrity. A side activity involving the study of a preliminary sizing tool for pressure relief valve is hence performed. A preliminary design framework is presented and discussed, highlighting the importance of the valve discharge coefficient. To study its dependence on the valve's geometry, a lengthy CFD simulation campaign is performed varying the poppet shape and the fluid Reynolds' number. Results are hence discussed and used inside the design framework.

\

Contents

\

List of Figures

\

List of Tables

\

Chapter 1

Introduction

1.1 Introductory statements and research aim

The work presented in this thesis is part of the "Greening the Propulsion" research program, encouraged by Italian Government and lead by GE Avio Aero with the participation of several industrial partners, such as Secondo Mona S.p.A. and BSim s.r.l. The main aim of this project is to develop novel technologies for the next generation of aircraft engines for civil applications[1]. Inside this framework, a significant effort has been dedicated to the research of novel components to push the performance of a few aircraft subsystems; as for the work presented in this thesis, the aim has been to develop and analyze a novel concept of low-pressure pump dedicated to the lubrication of mobile systems.

In this work, we define as "low-pressure pumps" those devices used to generate flow-rate inside variably complex system which main purpose is not to convey power to one or more mechanical users. The pressure they sense at the inlet port is often lower than 1 bar; the delivery environment pressure varies widely depending on the application, but remains usually in the order of 10 bar. In example, (U.S.Army, MIL-PRF-62180D(AT), 1997) performance specification requires fuel pumps to be tested when dealing with a delivery environment pressure of 65 psi for automotive application and 120 psi for aeronautic engines,

---

[1] For more information on the research program please visit:
https://www.researchitaly.it/en/national-technology-clusters/aerospace/greening-the-propulsion

while more recent specification can be found in (U.S.Army, MIL-PRF-32080F, 2014). For lubricating pumps, the old (U.S.Army, MIL-P-19131(SHIPS), 1956) specifies delivery pressures between 10 and 100 psi.

The thesis is organized as follows. In Chapter 1 the most common configuration of the lubrication systems employed in civil aircrafts are described and discussed, while the role of the used low-pressure pumps is highlighted. The general issues they face during their operative life are described and their possible effects on the pumps behavior highlighted. Chapter 2 presents an overview of the low-pressure pump types currently available on the market, while providing the method and the results of a few benchmarking operations performed over catalogues' data and analytic considerations. Starting from those results, the traditional gerotor pumps is discussed and novel design concepts are proposed in Chapter 3. In Chapter 4 a general mathematical description of the gears geometry based on the theory of gearing is provided, while Chapter 5 provides the theoretical basis of gerotor pumps sizing and simulation. These basis are hence applied in the definition of a novel Automatic Design and Simulation Framework, which implementation and performance are discussed in Chapter 6. This framework is hence applied in Chapter 7 and Chapter 8 to study the influence of the rotors geometry over the pump performance; at the same time, the new concept of asymmetric teeth for gerotor profiles is proposed and justified. In Chapter 9 the optimization of the newly proposed asymmetric profiles is carried on; a brief discussion over the optimization method in engineering is provided, hence results are presented and discussed to highlight the benefits of the new geometry, while an alternative approach to wear reduction is described in Chapter 10. To avoid the insurgence of critical pressure values inside the lubrication system, and hence the delivery side of the pump, pressure relief valves are applied; typically single-stage valves, they represent a critical, albeit theoretically understudied, component of the circuit. Chapter 11 and Chapter 12 cover the description of a side-activity focused on the definition of a simple rule-set to design conical poppet valves. In particular, Chapter 11 revolves around a new investigation of the effect of the poppet geometry over the valve discharge coefficient via CFD simulation, while Chapter 12 is focused on the definition of a design framework.

Please notice that due to previous agreements with our industrial partners, no experimental results can be provided to support the present work; moreover, details of the pump's geometry, prototypes design and performance won't be disclosed. Input parameters to the analysis presented in this thesis have been

altered with respect to those used for the industrial partners and are hence not representative of their work.

1.2 Introduction to gerotor pumps

Gerotor units are one of the most common solutions for pumping low pressure fluids, being often employed in lubricating circuits of motorbike (Frosina, Senatore, Buono, Manganelli, & Olivetti, 2014), automotive (Mancò, Mancò, Rundo, & Nervegna, 2000) and aerospace applications (Ippoliti & Hendrick, 2013), as well as in fuel distribution systems (Meyr, Cardé, Nitta, & Garas, 2002) due to their simple and compact design.

Gerotor pumps are obtained by coupling two gears, traditionally of cycloidal geometry, rotating around two parallel eccentric axes. The external rotor features N lobes, while the inner one features $N - 1$ teeth. The variable volume chambers generated by the gaps between the two gears are responsible for the fluid suction and delivery.
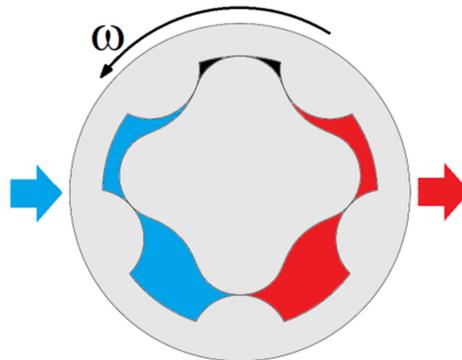
Figure 1: Simple scheme of a gerotor pump

To ensure the theoretical isolation of each variable volume chamber, the geometry of the two meshing rotors is such that there is continuous contact between them; rotors' profiles also define the shape of the chambers and their evolution during a complete rotation, hence contributing in a critical way to the device behavior. Traditionally, the fluid enters and exits the pump along its axial direction through properly shaped ports, allowing for obtaining extremely compact devices.

\

1.3 Literature review

Gerotor pumps technology is mature and well known; its origins come from the first intuition of (Colbourne, 1974), who first proposed the use of trochoid envelopes to define gears geometry for rotary pumps. Published research can be roughly divided into two main categories, that are the search for mathematical expression and automatic procedure to describe and design gerotors profile and the effort to find novel shapes optimizing performances for several application fields.

Starting from (Beard, Hall, & Soedel, Comparison of hypotrochoidal and epitrochoidal gerotors, 1991), who defined the superiority of the epitrochoidal profile over the hypotrochoidal one, and (Shung & Pennock, 1994), who provided a set of compact equations to describe several types of trochoid, many authors proposed modifications and improvements to the traditional cycloidal solution. Traditional profile performances and their dependence on geometrical parameters have been deeply investigated in (Beard, Yannitell, & Pennock, The effects of the generating pin size and placemen on the curvature and displacement of epitrochoidal gerotors, 1992), (Hsieh, 2009) and (Hsieh, Fluid and dynamic analyses of a gerotor pump using various span angle designngs, 2012), while an interesting optimization algorithm can be found in (Kim, Kim, & Chang, 2006). (Mimmi & Pennacchi, 1997) provided a comparison between a wide selection of alternative profiles, covering elliptic, sinusoidal and poly-circular cases. (Mancò, Mancò, Rundo, & Nervegna, 2000) proposed a novel gerotor profile based on parabolic teeth, while (Hsieh, Hwang, & Chang, 2007) provided some studies regarding novel profiles geometries, their properties and their effects over the pump performance. (Bonadrini, Mimmi, & Rottenbacher, Theoretical analysis of an original rotary machine, 2010), (Bonadrini, Mimmi, & Rottenbacher, 2012) as well as (Demenego, Vecchiato, Litvin, Nervegna, & Mancò, 2002) published the results of theoretical and numerical analysis for a few novel gerotor profiles, designed to limit the wear of the mating teeth. (Adams & Beard, 1997) provided theoretical justification to the proposal of helical and skewed axis gerotors, while alternative design concepts based on non-circular pitch and deviation functions can be found in papers from (Tong, Yan, & Yang, 2009), (Yan, Yang, & Tong, 2009), (Yang, Yan, & Tong, 2010). Several multiple profiles geometries have been proposed with the aim of obtaining better pressure angles during teeth meshing; a comprehensive literature can be found in (Litvin, Demenego, & Vecchiato, 2001), (Yan, Tong, & Yang, A new gerotor design method with switch angle assignability, 2007), (Yung, Bae, Kim, & Kim, 2011), (Choi, Kim, Lee, Yung, Bae, & Kim, 2012), (Bae, Kwak, San, & Kim, 2015). A different approach

for rotors design making use of straight line-conjugated profile can be found in (Lizhen, 2004), (Xu & Song, 2007), (Xu & Song, 2008) while a new interesting solution to reduce profiles wear through the use of variable clearances design has been recently proposed by Hsieh (Hsieh C. F., Flow characteristics of gerotor pumps with novel variable clearance design, 2015).

Meanwhile, important efforts were made to assess the most convenient mathematical expressions to describe the geometrical properties of gerotor pump profiles, paying particular attention to the determination of conditions leading to undercut problems. (Litvin & Feng, Computerized design and generation of cycloidal gearings, 1996) applied the theory of gearing (Litving, 1989) to a common cycloidal gerotor, defining the mathematical conditions that lead to singularities in the inner gear profile. Different formulations starting from these studies can be found in papers by (Vecchiato, Demenego, Argyris, & Litvin, 2001) and (Hwang & Hsieh, 2007), while an interesting geometrical interpretation has been provided by (Mimmi & Pennacchi, Non-undercutting conditions in internal gears, 2000). With regard to pump modelling, it is of particular interest the research work by (Ivanovic & Jositovic, 2006), (Ivanovic, Devedzic, Cukovic, & Miric, 2012) and (Ivanovic, Devedzic, Miric, & Cukovic, 2010).

1.4 Lubrication systems for aeronautic engines

To properly investigate the issues and the design constraints affecting low-pressure pumps it is firstly necessary to contextualize their behavior within their possible application fields; in the case under study, as stated in the introduction, the lubrication system for a new aeronautic engine has been considered.

The purposes of an engine lubrication system are:

- To avoid direct contact between mechanical bodies in relative motion (engine shaft bearings, gearbox…).
- To cool down the mechanical bodies in relative motion, often exposed at very high temperatures.
- To drive away and filter any wear debris in the lubricated components, to avoid the formation of dangerous deposits.
- To eventually pre-heat the fuel using the hot lubricant oil coming back from the engine.

To achieve these goals, it is possible to choose between a few possible configurations of the lubrication circuits; the optimal solution mainly depends on the aircraft class and purpose (tourism, civil transport, military) and on the engine

\

type. The users served by the lubrication system may differ depending on the engine design; in case of turbine engine, users are the compressor/turbine bearings and the whole gearbox, comprising both the main and the accessory line. For alternative thermal engine, nowadays limited only to tourism aircrafts, the lubrication system serves the piston chambers and the mechanical transmission connected to the engine shaft.

1.4.1 Dry-sump systems

Dry-sump circuits are by far the most used configuration in both civil and military aviation. A general scheme for a turbo-fan engine is reported in Figure 2, where three main lines can be appreciated:

- A pressure line (blue).
- A return line featuring hot (red) or cold (light blue) fluid.
- A breather conduct (grey).

The breather line senses the air pressure at the engine intake and keeps the tank pressure slightly above the atmospheric one. Under normal operative conditions, the "pressure" pump (also called "lube" pump), driven by the accessory gearbox takes the lubricant from the tank and conveys it through a filter and hence to the users. Here oil heats up and tends to deposit on the bottom of the engine sump; to avoid its deposit and ensure its return to the tank, a proper number of scavenge pump are used. Since their main purpose is to completely avoid the formation of oil deposits inside the engine, scavenge pumps are sized to generate an overall flow-rate higher than the one provided by the "lube" pump.
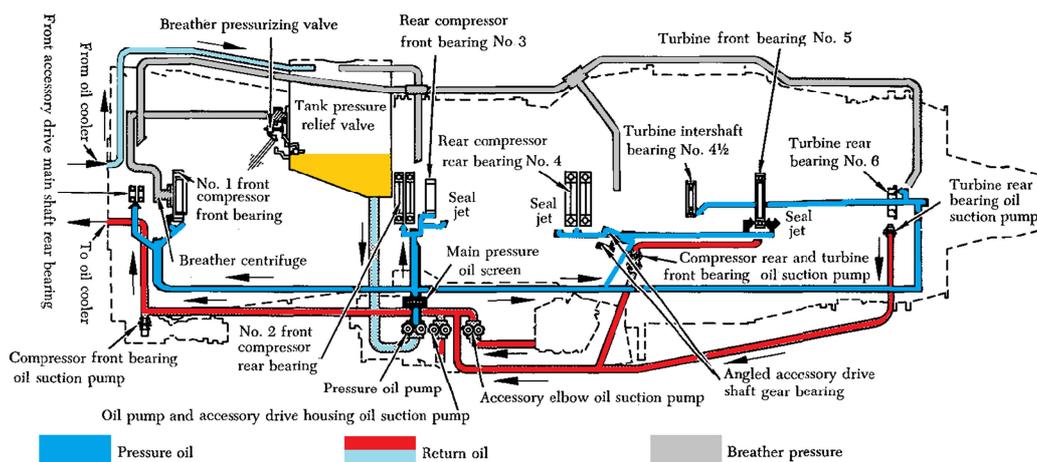
Figure 2: Scheme of a wet-sump lubrication system for turbo-jet engines

This, coupled with the lubrication process, causes the inclusion of a significant amount of air inside the oil in the return line; to avoid issues in the non-redundant lube pump, tanks are equipped with a de-aerator that separates the oil-air mixture (Steimes, Gruselle, & Hendrick, 2013). In most cases, it is preferred to avoid to send high temperature oil directly to the tank; as such, return oil is often forced to pass through an oil/fuel heat exchanger that is used to cool down the lubricant fluid while pre-heating the carburant. In other cases, such as the Dornier 328 jet engine, the oil/fuel heat exchanger is instead placed on the pressure line, as shown in Fig. 3. Whatever is its position, the heat exchanger is coupled with a thermostatic valve that regulate the oil temperature by defining which portion of the flow rate passes through the exchanger and which part can instead by-pass it. The scheme provided in Fig. 3 allow to highlight a few components related to a particularly stressing condition, that is the cold start of the engine. Since oil viscosity is strongly dependent on temperature, the pressure perceived at the delivery port of the lube pump can significantly rise and damage the system. To avoid this occurrence, two valves are introduced. A pressure relief (or cold start valve) is used to recirculate the fluid in excess, while an anti-surge valve avoids the filter occlusion by opening a by-pass path.
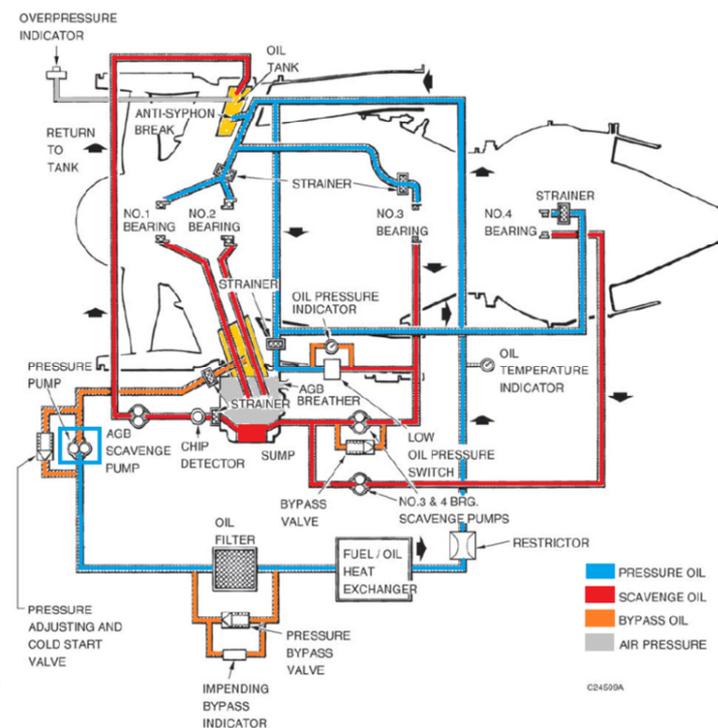
Figure 3: Scheme of the lubrication system for the Dornier 328 jet engines

\

1.4.2 Wet-sump systems

Wet-sump systems offer architecturally simpler solutions than the dry-sump configuration; they can be easily distinguished from the first type due to the absence of the tank and of the scavenge pumps. Oil is simply collected in the engine sump and recirculated by the pressure pump. A few disadvantages make this solution less attractive than the dry-sump option:

- Since no scavenge pumps are present, aircraft cannot perform quick maneuvers, roll angle must be limited and flight at negative $\vec{g}$ is usually prohibited
- Safety issues may rise in case of fire inception, since there is no way to separate the tank from the rest of the engine

They are more easily found in small tourism aircrafts driven by alternative thermal engines, while their use in turbine or turbo-jet configurations is almost negligible.

1.5 General definitions for (low-pressure) pumps

Before stepping in the application-specific issues affecting low-pressure pumps, we provide a brief reminder about a few basics expressions commonly used to describe the performances and the characteristics of any rotary pumps.

We define as *displacement* or *capacity* Δ the volume of fluid that the pump is theoretically able to convey at each complete revolution of its driving shaft. It linked to the *mean theoretical flow-rate* over one pump cycle $Q_{th,m}$ through the following expression.

$$Q_{th,m} = \Delta\, n \tag{1}$$

Where *n* is the *rated speed* of the pump. Given the pressure drop between the pump inlet and delivery environment, the *average theoretical torque* $T_{th,m}$ required to drive the pump at speed *n* can be computed as follows.

$$T_{th,m} = \Delta\, (p_{out} - p_{in}) \tag{2}$$

We define as *hydraulic efficiency* η_h the following ratio:

$$\eta_h = \frac{Q_m}{Q_{th,m}} = \frac{Q_{th,m} - Q_{leak,m}}{Q_{th,m}} \tag{3}$$

Where Q_m is the measured average flow rate over one pump revolution and $Q_{leak,m}$ is the average flow-rate lost due to leakages. In a similar fashion, we define as *mechanical efficiency* of the pump the ratio between the theoretical and the measured torque at the driving shaft as follows.

$$\eta_m = \frac{T_{th,m}}{T_m} = \frac{T_{th,m}}{T_{th,m} + T_{fr,m}} \tag{4}$$

Where $T_{fr,m}$ is the average friction torque developed inside the pump and the pump's supports due to sliding between bodies in relative motion. The overall efficiency associated with the power consumption of the operating device can be hence computed as follows.

$$\eta_p = \frac{T_{th,m}Q_m}{T_m Q_{th,m}} = \eta_h \eta_m \tag{5}$$

1.6 General issues for mobile low-pressure pumps

Considering both the dry-sump and the wet-sump configurations, it stands out that the lube pump is usually not redundant in civil applications, meaning that its eventual failure would immediately lead to the engine malfunction. As such, it is common practice to switch off the engine with the failed lube pump to avoid fire inception and mechanical breakage due to missing lubrication in critical components. In military application, the Defense Federal Acquisition Regulation treats this device as a Critical Safety Item (CSI) since its loss is associated with *"an uncommanded engine shutdown that jeopardizes safety"* (U.S.Army, Aviation Critical Safety Item Management Handbook, 2011). Although civil aircraft are nowadays designed to sustain the loss of one (or more) engine(s), this situation should be avoided since it causes the worsening of the vehicle's handling while introducing additional challenges to the pilots. As such, the issues that the lube pump may face or will face during its operative life must be carefully investigated. In this subsection, we illustrate the challenges to be faced and the problems to be considered when approaching the design of a new low-pressure pump for aeronautic applications.

1.6.1 Wide temperature range

The first significant issue for low-pressure pumps operating in aeronautic applications is the wide temperature range that they have to face. Lubrication pumps are particularly prone to this issue, since they must be able to work at both extremely low temperature, such as -40°C during the so called "cold-start" conditions, and extremely high temperatures, in the order of 100°C, when the

\

engine runs at full power. The wide temperature range affects both the mechanical and the hydraulic performance of the pump; friction forces and gap sizes are in fact depending on temperature, as well as the lubricating fluid properties such as viscosity, Bulk modulus, air solubility and fluid density (Stachowiak & Batchelor, 2005).

In particular, the viscosity of lubricating oils tends to vary widely due to temperature, hence strongly influencing the pump leakages during its operational life. As a simple example of this, we may consider a generic aeronautic oil for the lubrication of turbine engines. According to the MIL-L-23699E standard (U.S.Army, 1994) the kinematic viscosity v at -40°C must be below or equal to 13000 cSt; the minimum value at 40°C must be higher than 24.5 cSt, while at 100°C it must be within the 4.90-5.40 cSt interval. Please notice that similar oil characteristics are recommended also for the lubrication of helicopter transmission systems (U.S.Army, DOD-PRF-85734A, 2004). For a small gap of rectangular section, leakage flow rate is usually expressed through the Hagen-Poiseulle law.

$$Q_{leak} = (p_{up} - p_{down}) \frac{b h_g^3}{12 \mu l_g}$$ (6)

Whereas p_{up} and p_{down} are the fluid pressure upstream and downstream the gap, b is the gap width, h_g its height and l_g its length; μ is instead the fluid dynamic viscosity. For generic unitary values of the geometrical and pressure variables, it is possible to observe the viscosity and hence the leakage variation depending on temperature depicted in Fig. 4.
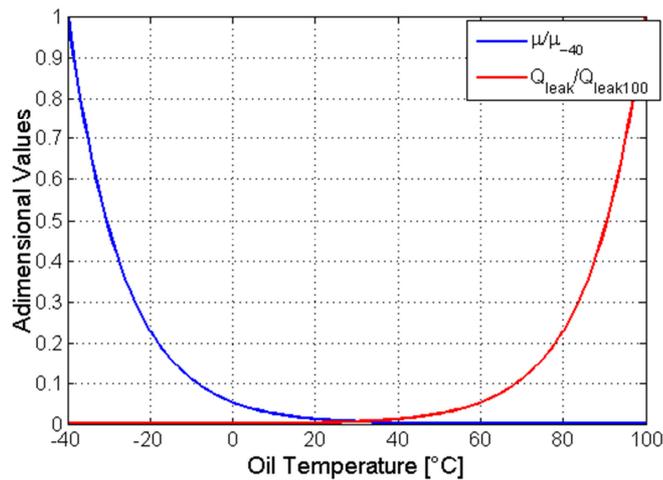
Figure 4: Viscosity and leakage behavior on oil temperature

1.6.2 Cavitation

Cavitation is an extremely dangerous phenomenon that may interest low-pressure pumps dealing with air-oil mixtures and/or with lubricating fluid at very low pressures. Cavitation is a phase change process from liquid to vapor which occurs at constant, if not slightly decreasing, temperature (Franc, 2006). Apart from a few secondary factors that may slightly delay it, such as the fluid superficial tension, cavitation can be considered incipient and hence developing whenever the fluid pressure p falls below the vapor tension p_v (Brennen, 1995).

$$p \leq p_v \qquad (7)$$

Those generated bubbles will implode if subjected to external pressures higher than the internal one. (Franc, 2006), considering vapor-only, perfectly spherical bubbles, provided a few simplified but explicative equation about the bubble collapse process. In particular, we can identify a collapse time τ_b function of the fluid density ρ_{oil}, the initial bubble radius $R_{b,0}$ and the fluid pressure far from the bubble p_∞.

$$\tau_b \cong 0.915 R_0 \sqrt{\frac{\rho_{oil}}{p_\infty - p_v}} \qquad (8)$$

Defining as r_b the distance from the bubble center and with R the bubble radius at the time instant t, the fluid pressure $p(r_b, t)$ can be in first approximation computed as:

$$p(r_b, t) = p_\infty + (p_\infty - p_v)\frac{R}{3r}\left[\frac{R_0{}^3}{R^3} - 4\right] - \frac{R^4}{3r^4}\left[\frac{R_0{}^3}{R^3} - 1\right] \qquad (9)$$

For rotary pumps operating at low pressure and high speed cavitation usually takes place in the suction side (Mancò, Nervegna, & Rundo, 2001). The small vapor and/or gas bubbles, dragged by the pump motion, tend hence to quickly collapse once they reach the high-pressure delivery zone. To highlight the damaging capability of the cavitation phenomenon, results for a reference case featuring a hydraulic fluid with density equal to 910 kg/m³ and considering an external pressure of 10 bar are reported in figures 5 and 6. It is worth to notice that bubble collapse can be extremely rapid (in the order of 10-300 µs at 10 bar) and may give origin to pressures comparable to the yield modulus of the most common metallic materials. Moreover, the maximum pressure is located nearby the walls of the collapsing bubble (for *r/R* ratios between 1 and 1.5 circa), meaning that cavitation is more dangerous if the bubbles are attached to the pump components.

\

According to (Singh, 1991) and (Mancò, Nervegna, & Rundo, 2001), low-pressure rotating pumps have essentially three main preferred sites for cavitation inception, that are

- Cavitation at the rotor(s) tips; due to high linear speed associated with excessive rotary frequency of the driving shaft
- Cavitation at the inlet port; due to narrow inlet ports
- Cavitation caused by incomplete filling of the chambers; due to low pressure at the suction port and/or excessive speed of the driving shaft, often occurring in scavenge pumps.
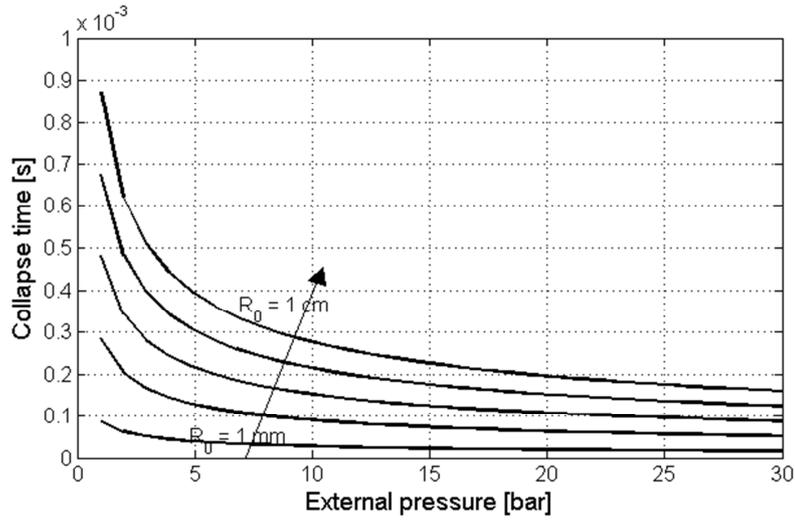
Figure 5: Example of cavitation bubbles collapse time
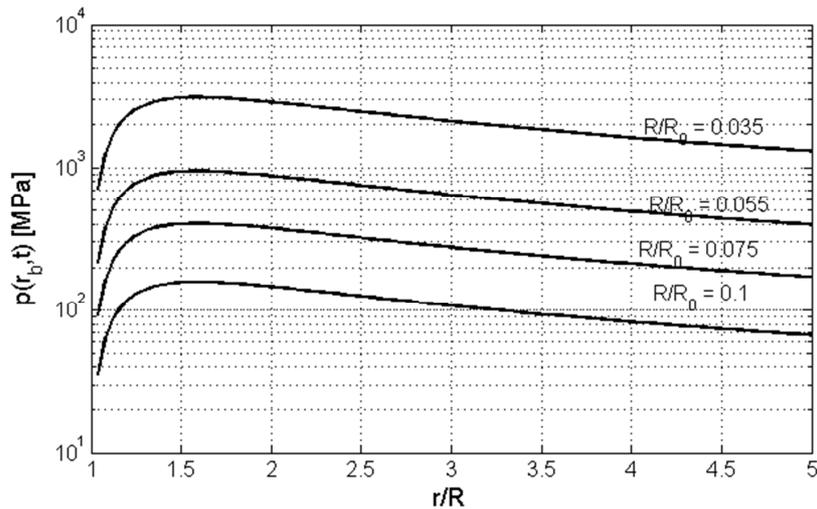
Figure 6: Pressure in the fluid surrounding a collapsing cavitation bubble

1.6.3 Wear

Wear is a critical issue for low pressure pumps and for the whole system in which they operates. (Stachowiak & Batchelor, 2005) identified three main wear mode, that are:

- Abrasive wear: due to the contact between a surface and a harder body.
- Adhesive wear: due to adhesion between portion of the mating surfaces of two bodies in relative motion, usually associated with direct metal-on-metal contact.
- Fatigue wear: due to repeated Hertzian contact, also known as pitting outside of the tribology community.

The main effect of wear in rotary pumps is the increase of the gap size between elements in relative motion, that would lead to increased leakages and hence reduced hydraulic efficiency, especially in combination with high-temperature fluids. Secondary effects would be the worsening of the pump's dynamics and the occurrence of impacts between meshing components. Moreover, the produced metallic debris may accelerate abrasive wear inside the pump itself or in the other system's components and accelerate the oil oxidation process (Stachowiak & Batchelor, 2005). Wear can effectively limit the pump operative life, forcing the pump flow rate capability outside of the minimum acceptability threshold; as such it must be properly mitigated by acting on the mechanical design of the moving components of the device.

1.6.4 Mass and envelope

Requirements for mobile applications' equipment are often highly demanding in terms of containing the mass and the overall envelope of the employed components. Common reasons behind this are the need to reduce the fuel consumption and hence the power demanded to the engines, limited availability of space, easier storage and transportability of the spare parts.

The simplest operation to reduce the mass and overall volume occupied by the pump is to increase the reference speed of the driving shaft. As shown by Equation (1) pump displacement tends in fact to decrease linearly with the speed while considering constant flow rate requirements. In a similar fashion, the required theoretical torque at the driving shaft decrease linearly while keeping constant the overall pressure drop across the device.

\

Pump downsizing is however limited by a few issues that make it difficult to increase the driving speed shaft over certain limitations. The first issue is related to cavitation; since higher values of reference speed would translate into higher linear velocity of the fluid in the pump's periphery, stricter limitations on the diametral dimension of the device must be imposed. The reduced diametral dimensions directly affect the maximum size of the rotating components shaft(s); although the theoretical torque tends to decrease, the static pressure drop acting on the shafts and their supports is still the same. Hence situations may happen in which the maximum available dimension of the shaft is not enough to survive to static and/or rotary bending fatigue. Moreover, the required axial length of the pump might be too high to avoid incomplete filling of the chambers and/or excessive bending of the shaft(s).

1.6.5 Jamming of the pump and debris behavior

Another issue affecting the low-pressure pumps, especially those operating within a lubrication system, is the risk of jamming due to the ingress of hard metallic particles which size is comparable to that of the variable volume chambers. Since the consequences of this event may be critical for the lubricated system and for the users' safety, jamming issues should be investigated and considered in the choice of the filter eventually positioned between the tank/sump and the pump.

Debris may come from the pump itself or more commonly from the lubricated system; in aeronautic applications debris size and number is often monitored for diagnostic purposes (Tauber, 1981), (Muir & Howe, 1996) and (Higgins & Crow, 1997).

Chapter 2

Low-pressure pumps benchmark

2.1 Benchmarking reasons

To assess the capability of the current state of the art of the gerotor pump we carried out a comparison with other rotary pumps commonly employed in low-pressure systems. This chapter is organized as follows: at first a few pump technologies alternative to gerotor pumps are presented and discussed; a functional comparison is performed and it is integrated with the results of a literature research over the catalogues of several industrial suppliers. The benchmarking activity is hence finalized through analytic tools based on simplified sizing procedures; its results of this process are hence used to highlight the advantages and limitations of the traditional gerotor pumps.

2.2 Considered pump types

The pump types considered in the benchmarking process are compliant with the following requirements:

- Rotary driven
- Fixed displacement configuration
- Suitable for low-pressure systems
- Simple design (low number of moving components)
- Suitable for mobile applications

\

Apart from gerotor devices, we identified four more pump types for this analysis; external and internal gear pumps, lobe pumps and vane pumps (both balanced and unbalanced).

2.2.1 External gears pump

External spur gears devices are a common choice to lubricate turbine assemblies such as aeronautic engine and wind power systems. Fluid is moved by the combined action of two meshing gears with spur teeth; one of them is driven by an outside power source (may it be the accessory gearbox, an electric motor etc.), while the other is mounted over a foul shaft. The inlet and delivery ports are positioned along a direction orthogonal to the inter-axis between the two gears; fluid is sucked inside the pump due to the generation of a negative pressure drop between the inlet chamber of the pump and the tank environment.

Hence it is convoyed by the two gears towards the high-pressure delivery environment by means of fixed-volume chambers theoretically isolated one from another. When the fluid reaches the delivery environment its pressure is forced to raise and its majority is hence expelled towards the users; a usually small portion of the fluid may instead remain trapped between the meshing teeth and hence be sent back to the pump entrance. This volume of fluid can be considered as a loss of the theoretical pump capacity and is often addressed as "dead volume".

The theoretical displacement of the pump depends on the teeth number of the two gears Z, on the fixed chamber volume V_{max} and on the trapped volume V_{min} (Nervegna & Rundo, 2016).

$$\Delta_{eg} = Z(2V_{max} - V_{min}) \tag{10}$$

Leakages are mainly located in the functional gaps between the gears and the housing; their theoretical increase with temperature can be partially compensated using different materials in the rotors and in the housing.

From an envelope perspective, the use of two meshing gears mounted on parallel axis can be a fair disadvantage with respect to other solutions; moreover, they tend to become noisy once that wear takes place. On another note, the maturity of the technological processes needed to produce this pump type allows to obtain extremely robust and reliable devices.

Figure 7: An external spur gears pump[2]

2.2.2 Internal gears pump with crescent

Internal gears pumps with crescent follow a design philosophy similar to that used in gerotor devices; however, the difference between the number of teeth in the inner and outer rotors is higher than   It is as such impossible to ensure the isolation of the suction and delivery environment without inserting an additional component, the crescent, which moon-shaped scheme can be easily observed in Fig. 8.

Inlet and outlet port of the pump may be placed either in the radial or in the axial direction, while its theoretical displacement can be computed given the teeth number of the inner gear Z_i, the maximum isolated volumes defined by both the inner ($V_{max,i}$) and the outer ($V_{max,e}$) gear with the crescent and the dead volume V_{min}:

$$\Delta_{ic} = Z_i\left(V_{max,i} + V_{max,e} - V_{min}\right) \tag{11}$$

Internal gears pumps with crescents tend to provide more regular flow rates than the gerotor pumps, while providing a compact solution that can be extremely miniaturized (Nervegna & Rundo, 2016). However, the small size of the chambers make them less suitable to work in presence of metallic debris.

---

[2] From http://www.e4training.com/

\
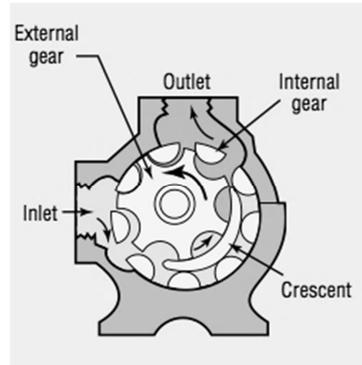
Figure 8: An internal gear pump with crescent[3]

2.2.3 Lobe pumps

Lobe pumps make use of two rotors with conjugate profiles to convey fluid between low and high pressure environments. On contrary with the pump types presented so far, these rotors are not responsible of any motion transmission between the two axis; the number of lobes usually employed (two or three) is in fact too low to allow for regular power transmission. As such, their only function is to convey the fluid avoiding as much as possible back-flow issues from delivery to the tank. The motion transmission is instead ensured by two synchronizing gears, usually featuring helical teeth; this solution makes the lobe pumps an extremely quiet solution, that has found a good diffusion in medical applications.

The pump displacement can be computed as the external gear case, given the lobe number N :

$$\Delta_{ic} = N(2V_{max} - V_{min}) \tag{12}$$

Figure 9: An industrial lobe pump[4]

---

[3] Adapted from http://hydraulicspneumatics.com/

2.2.4 Vane pump

Vane pumps differ from the previously described devices due to the use of only one rotary element. As shown in Fig. 10, the variable volume chambers responsible for the flow rate generation are described by the space comprised between the rotor, the stator (or cam ring) and two adjacent sliding vanes. During operations, vanes are forced by centripetal acceleration to remain in contact with the race obtained in the stator, hence avoiding back-flow issues. In some designs the delivery pressure is brought back at the base of the vanes and here used to ensure the contact with the stator. The shape of the cam ring is hence responsible of the chambers behavior and so of the pump performances.

Two main types of vane pumps can be identified, that are balanced and unbalanced. In balanced vane pumps the design allows to compensate for the pressure drop between inlet and outlet of the device, hence reducing the load on the rotor shaft and on its supports. The unbalanced version is not able to provide the same features, but offers a more compact solution and a simpler design of both the stator race and of the admission/delivery ports; since in low-pressure applications the pressure drop between delivery and suction sides is moderate, this solution if the most common for lubrication systems of mobile applications.

Vane pumps, depending on the vanes design, feature a significant advantage over every other device described so far, that is their capability to recover from wear up to a certain extent. The backlash that would be created by wear occurrence at the tip of the vanes is in fact compensated by the pump design, which forces the vanes against the cam ring.
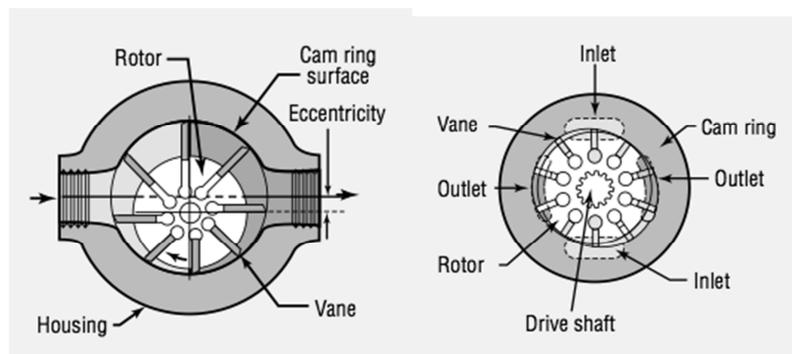
Figure 10: Unbalanced and balanced vane pumps[5]

---

[4] Adapted from http://www.wastecorps.com/
[5] Adapted from http://hydraulicspneumatics.com/

\

Vane pump displacement for the balanced and the unbalanced case can be computed given the number of vanes N, their volume V_{vane}, the minimum and maximum volume of each chamber and the number of pumping cycles for shaft revolution n_c.

$$\Delta_{bvp} = N n_c (V_{max} - V_{min} - V_{vane}) \tag{13}$$
$$\Delta_{uvp} = N (V_{max} - V_{min} - V_{vane}) \tag{14}$$

2.3 Functional comparison

A first functional comparison based on the simple observation of the major design peculiarities of each pump type can be performed. The considered criteria here reported can be related to the common issues affecting low pressure pumps described in Chapter 1. We have:

- Number of moving component: related to design complexity
- Number of rotors on parallel axis: related to pump envelope
- Wear recovery capability

Results are reported in Table 1.

Table 1: Functional comparison

Pump type	# Moving components	# Rotating axis	Wear recovery
Gerotor	2	2 (internal coupling)	No
External gears	2	2 (external coupling)	No
Internal gears	2	2 (internal coupling)	No
Lobe	4 (2 rotors) (2 gears)	2 (external coupling)	No
Vane (balanced /unbalanced)	$1+N_v$ (1 rotor) (N_v vanes)	1	Yes

Vane pumps have the lowest number of rotating axis and are the only type providing a certain extent of wear recovery, but suffer from a possibly high number of moving components. Lobe pumps features a high number of rotating components on two parallel axes moved through two external gears, which lead to non-compact design. From a brief examination, it is possible to observe that gerotor pumps are positioned in the middle of these extremes, featuring a compact design with only two moving components.

2.4 Comparison of catalogues data

To support the preliminary results of the functional comparison, a deep analysis based on the catalogues of the main low-pressure pumps providers has been performed. This second analysis is intended to provide some additional indications but remains fairly limited. Most of the available data regards industrial applications and no information on the sizing inlet pressure value are provided. Moreover, most of the pumps used on mobile applications are customized solutions which specifications are not publicly available.

A few results are reported in Figs. 11-13. In Fig. 11, the displacement values for the previously selected pump types are reported as function of the reference speed of the driving shaft. A few takeaways can be provided; lobe pumps are limited to very low reference speed due to the need of reducing their wear rate, while gerotor pumps and external gears devices work over a wider span of angular frequencies and were the only types for which a good amount of data for mobile applications were available. Data regarding internal gears pumps and vane pumps were instead limited to industrial cases, so that no conclusive information can be deducted. In Fig. 12 are instead reported the obtained data on the delivery environment rated pressure and the pump's nominal flow-rate. The examination is limited to a maximum value for the pressure at the outlet port of 500 psi.

\
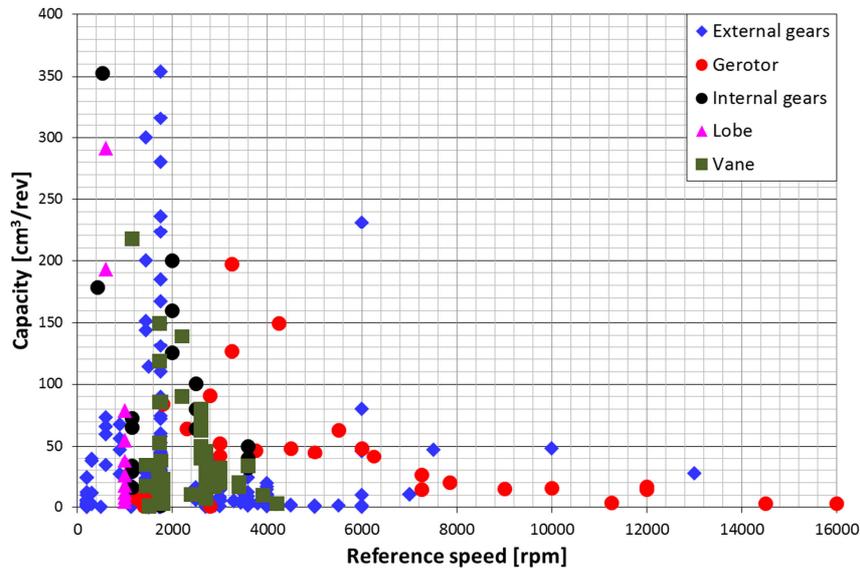
Figure 11: Catalogues data – capacity vs rated speed
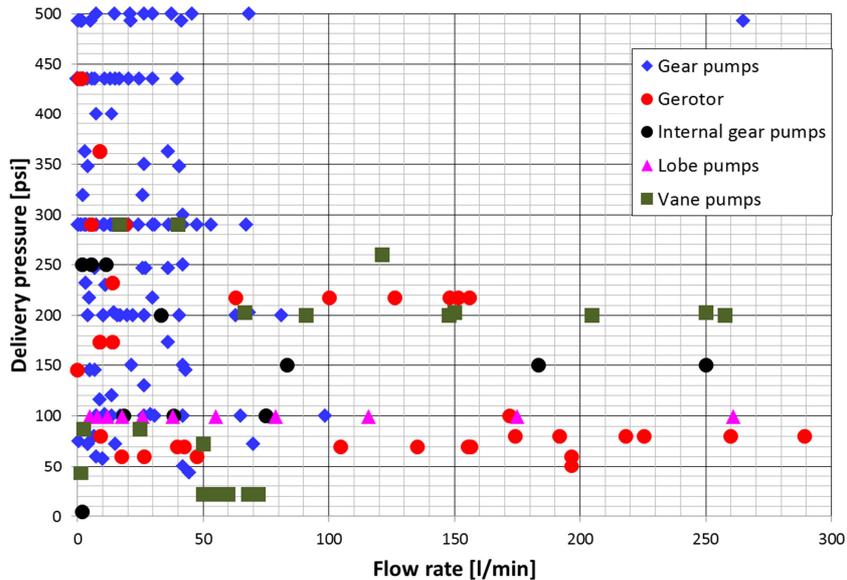
Figure 12: Catalogues data – delivery pressure vs flow rate

External gears pumps are the most used type for pressures approaching the 500 psi limit, while the other pump types are mostly used in the low-pressure and high flow-rate operating field. By crosschecking these results with those reported in Fig. 11, it is possible to further distinguish between, in example, gerotor and lobe devices; in the first case, the high flow rate is associated with low capacities and high rotating speeds, while the opposite occurs in the latter.
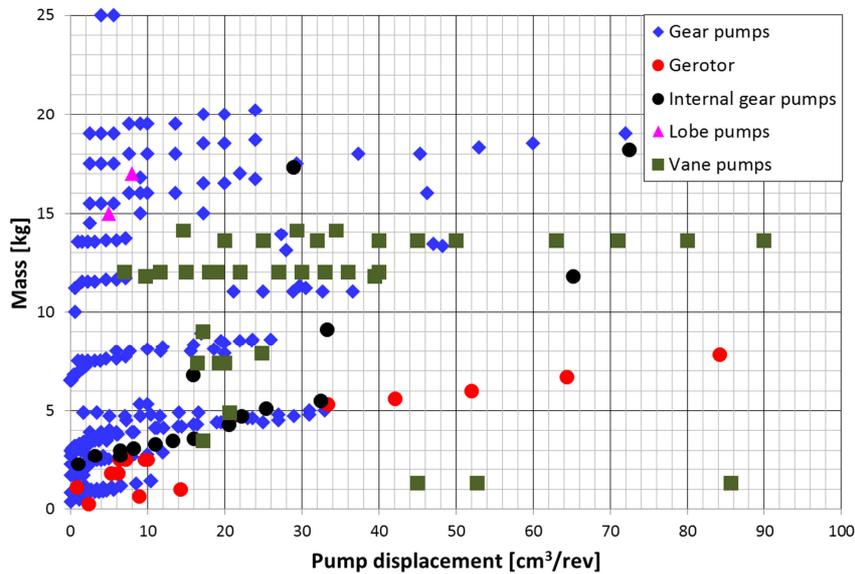
Figure 13: Catalogues data – pump's mass vs displacement

Finally, Fig. 13 depicts the behavior of the pumps' overall mass reported in the catalogues in dependence of the device capacity. Although a significant data dispersion is observable due to the differences in the rated pressure drop, some trend can be still observed and a few comparison may be carried out. Results are limited at a maximum weight of 25 kg. It can be observed that vane and gerotor pumps appears to be able to provide a fairly noticeable advantage with respect to external gear pumps, while lobe devices looks less attractive (most of their data are outside the 25 kg threshold). Internal gear pumps with crescent appears to be in line, if not slightly worse, than gerotor pumps, but the scarcity of data doesn't allow to perform an in-depth comparison.

Summing it up, the conclusive remark for this first assessment of the low-pressure pumps state of the art are:

- Gerotor pumps are suitable for high-speed, high-flow rate and low delivery pressure situation
- External gears pumps are more used in high-flow rate and high delivery pressure cases
- Vane pumps seem the best option to limit the pump's weight
- Lobe pumps are complex, heavy and limited in rated speed
- Internal gear pumps with crescent are in line with gerotor pumps, but features an additional layer of complexity (the crescent)

\

2.5 Analytical trade-off

The first trade-off analysis described in this chapter provided some early indication regarding the state of the art of low-pressure pumps. In order to get more accurate and meaningful results, we set up another comparison based on the outputs of simplified sizing frameworks prepared for a few selected pump types.

Given the results of the first trade-off analysis discussed in Chapters 2.3 and 2.4, the trade-off process investigate the performances and main constructive features of gerotor pumps, external gear pumps and unbalanced vane pumps (with 4 and 6 vanes).

This trade-off activity makes use of some simplifying assumptions to reduce the computational effort and avoid second-approximation details. As such:

- Fluid is considered uncompressible
- Only the theoretical displacement is considered
- Leakages are neglected
- Pumps are always working in steady-state conditions
- Meshing is ideal and no backlash is considered

2.5.1 Simplified design framework for traditional gerotor

The simplified design framework employed in this benchmarking activity is based on the analytical description of the gerotor profiles provided by (Mancò, Mancò, Rundo, & Nervegna, 2000) and on the equations to handle the suction and delivery ports reported by (Singh, 1991) and (Mancò, Nervegna, & Rundo, 2001). The framework works through four sequential steps; at first, given the design input parameters, it computes the geometrical parameters describing the rotors profiles. Hence it verifies their validity, estimate the maximum axial length of the pump and evaluate its capacity. The mathematical expressions are here reported and their physical interpretation discussed.

Traditional gerotor pumps makes use of circular lobes in the external gear and of an epitrochoidal profile in the inner rotor; the geometrical parameters defining the pump's shape are observable in Fig. 14 (Mancò, Mancò, Rundo, & Nervegna, 2000). Between those, the most important are the eccentricity e, equal to the difference between the two centrodes radiuses r_1 and r_2, and the non-dimensional ratio λ defined as:

$$\lambda = \frac{a}{r_1}$$

(15)

Given these two input parameters is possible to derive every other meaningful quantity; addressing with r_i and r_e the minimum radius of the inner rotor and the maximum radial dimension of the external profile we can write the following expressions.

$$3e = r_e - r_i \tag{16}$$

$$r_e = a - \rho + 2e \tag{17}$$
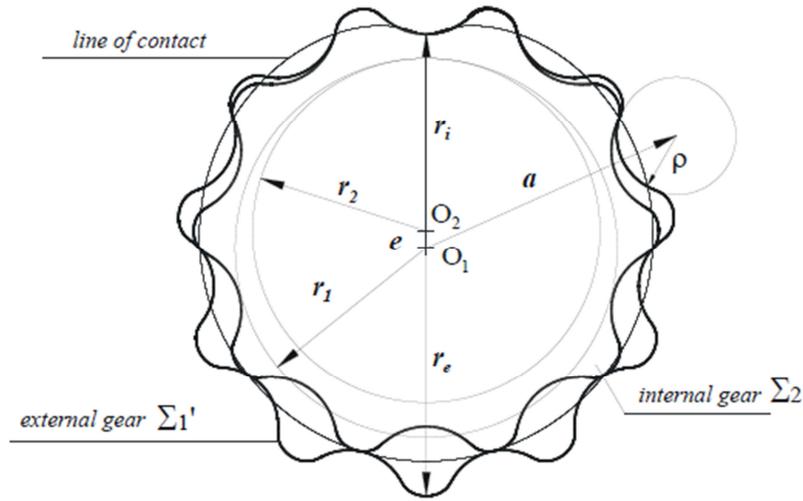
Figure 14: Geometrical parameters for epitrochoidal gerotor pumps

In first approximation, the threshold value for the pump linear speed associated with cavitation inception can be computed through the application of the Bernoulli equation at the inlet port:

$$v_{max} = \sqrt{\frac{2p_{in}}{\rho_f}} \tag{18}$$

Where ρ_f is the fluid density and p_{in} the pressure upstream the inlet port; this limitation on the admissible fluid velocity translates into a limit on the maximum linear speed of the rotors tips. Defining the reference speed of the pump's driving shaft for the design process as ω and considering the limit conditions we have:

$$r_e = \frac{v_{max}}{\omega} \tag{19}$$

Hence, given a certain inlet pressure and a defined reference speed, each (e, λ) couple mathematically identifies a possible rotors profile, provided the

\

number of lobes in the external rotor N. Not every (e, λ) is able to generate valid profile, since badly defined parameters may give origin to geometrical discontinuities in the gears shape. For the traditional geometry, (Mancò, Mancò, Rundo, & Nervegna, 2000) provided simple closed form expression to ensure the profiles validity. The first condition regards the non-dimensional parameter λ, which value must be comprised between:

$$1 \le \lambda \le N \tag{20}$$

The second condition affects the lobes curvature radius ρ which must satisfy:

$$\frac{r_1 \left(\frac{r_1}{r_2} - 1\right)(\lambda - 1)^3}{\lambda^2 \left(1 - \frac{r_1}{r_2}\right) - \frac{r_1}{r_2} + \left(2\frac{r_1}{r_2} - 1\right)\lambda} \le \rho \le \frac{\left(\frac{r_1}{r_2} - 1\right)\sqrt{27(a^2 - r_1^2)}}{\left(2\frac{r_1}{r_2} - 1\right)^{3/2}} \tag{21}$$

According to (Mancò, Nervegna, & Rundo, 2001) there exists a precise limitation over the axial length of the pump that can ensure the complete filling of the chambers given a defined pressure drop on the inlet port and a reference speed of the rotors. This maximum value H_{lim} depends in first approximation on the evolution of the frontal area of the variable volume chambers A_{ch} over angular position of the inner rotor α:

$$H_{lim} = A_p \frac{n_s \sqrt{\frac{p_{in}}{\rho_{oil}}}}{\omega \frac{dA_{ch}}{d\alpha}} \tag{22}$$

Where p_{in} is the pressure at the inlet port, ρ_{oil} the fluid density and $A_p \le A_{ch}$ the inlet port area. n_s is instead the number of feeding sides, that can be equal to 1 or 2, depending if the ports are present on one or both of the gerotor's frontal plates. Once that the axial length of the pump $H \le H_{lim}$ has been defined it is possible to compute the theoretical capacity of the device as:

$$\Delta = (N - 1)A_{ch}H \tag{23}$$

These equations, along with the mathematical description of the profiles geometry provided by (Mancò, Mancò, Rundo, & Nervegna, 2000), have been implemented in one Excell program that requires as input the inlet and delivery port pressures, reference speed, required flow rate and the (e, λ) couple. Through Equation (1) it computes the required capacity; given the input parameters it designs and draws the rotors' profiles, numerically evaluates the chambers frontal area and calculates the required axial length, while verifying the necessary

conditions reported in Equations (20), (21) and (22). Hence it estimates the overall envelope and weight of the pump, given the materials density for each major component, such as inner rotor, outer rotor and case. As an example of the simplified sizing procedure we provide in Fig. 15 the profiles for two gerotor pump operating with 15 psi at the suction port, driven at 7000 rpm and 5000 rpm, while featuring 5 and 7 teeth in the external rotor.
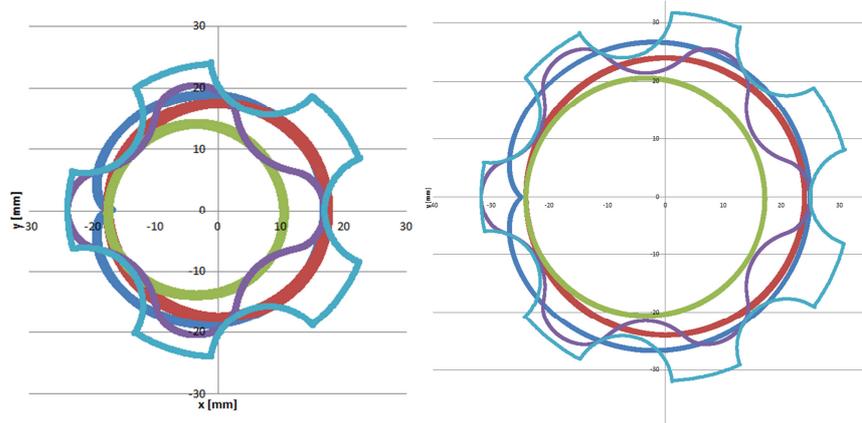
Figure 15: Examples of gerotor profiles (simplified design tool)

To verify the simplified design tool behavior, a comparison between its results and the data publicly available in catalogues by Nichols' is carried on. Reporting in Fig. 16 the theoretical flow rate of the pumps in dependence of the reference speed, it is possible to observe a good agreement between catalogue's and computed data.
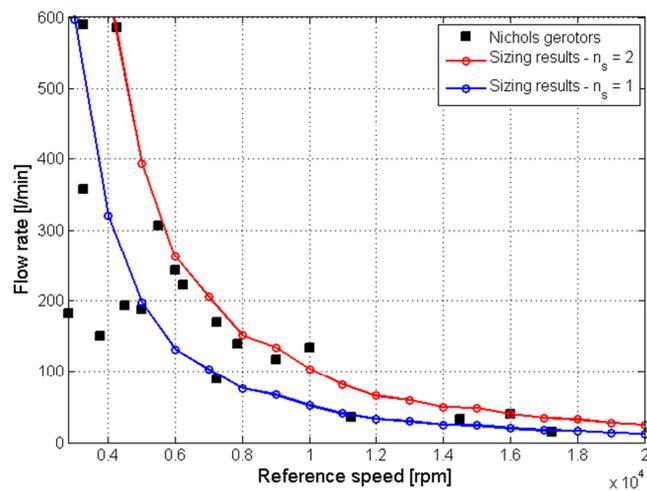
Figure 16: Simplified design tool: comparison with Nichols catalogue

\

2.5.2 Simplified design framework for external gear pumps

The simplified design framework for external gear pumps has been kindly provided by the leading companies of this research program. As such, no details will be disclosed and every result associated with this tool will be provided in a non-dimensional format.

2.5.3 Simplified design framework for unbalanced vane pumps

The tool used to design in first approximation the unbalanced vane pumps used in the trade-off activity makes use of a few significant geometrical parameters highlighted in Fig. 17. Those are the length (or semi-length) of the vanes L, the cam radius $R_e(\propto)$, function of the angular coordinate, and the rotor radius R_i.

The cam radius varies between a theoretical minimum equal to R_i and a maximum value equal to R_e along the suction and delivery ports, while it remains constant along the angular span associated with the isolated chamber condition. To avoid backflows issues, each of the two angular spans at constant cam radius must extend for at least a minimum value $\Delta\alpha_{min}$ defined as:

$$\Delta\alpha_{min} = \frac{2\pi}{N_v} \tag{24}$$

Where N_v is the vanes number. The more the vanes, the longer the angular span that might be dedicated to the suction and delivery ports. The maximum lift of the vanes h is equal to the difference between R_e and R_i; R_e is limited by the same Equation (19) used for gerotors, while R_i value is obtained through static and fatigue sizing of the shaft.
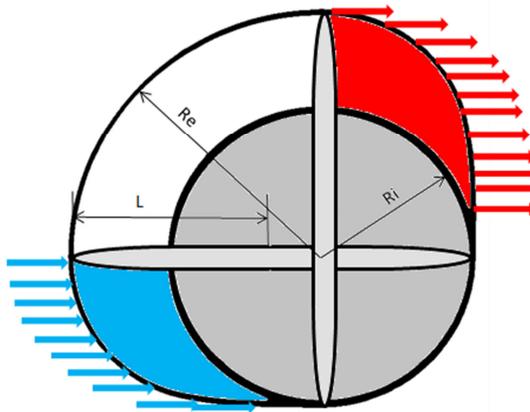
Figure 17: Unbalanced vane pump scheme

The cam shape is hence designed according to the classical synthesis methods based on the motion law equations paying attention that additional requirements may come from the vanes design. In example, if the four vanes are obtained with only two translating elements such as in Fig. 17, the following condition must be respected:

$$r_e(a) - r_e(a + \pi) = 2L \tag{25}$$

This requirement can be satisfied only by symmetric laws of motion, hence imposing a significant design constraint over the cam definition. In this simplified design tool we make use of linear speed laws similar to the example reported in Fig. 18. The maximum geometrical speed h'_{max} and acceleration h''_{max} for the vanes lift can be computed given the dedicated angular span $\Delta\alpha_{cam}$:

$$\begin{cases} h'_{max} = 2\dfrac{h}{\Delta\alpha_{cam}} \\ h''_{max} = 2\dfrac{h'_{max}}{\Delta\alpha_{cam}} \end{cases} \tag{26}$$

Hence, defined the geometrical acceleration shape, the cam radius can be obtained as:

$$r_e(a) = r_i + \iint_\alpha h'' d\alpha d\alpha \tag{27}$$
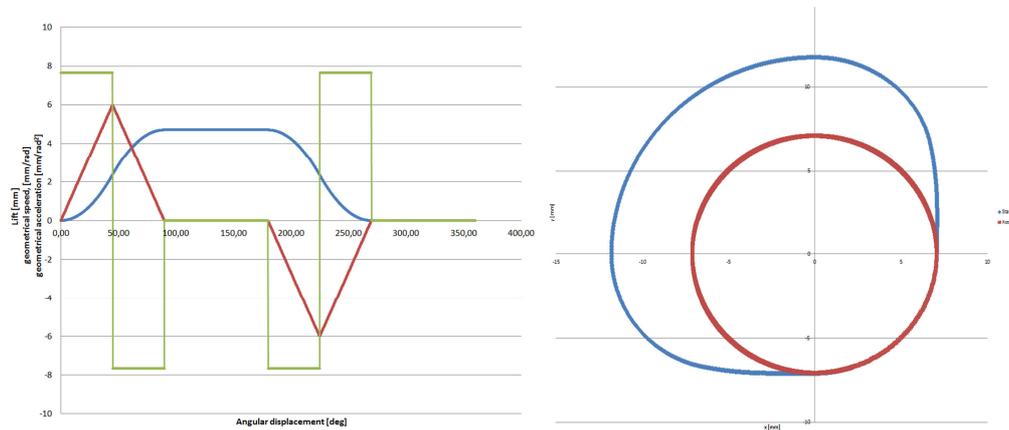
Figure 18: Example of motion law for the vanes lift and resulting geometry

Once that the cam shape has been defined, the simplified design tool perform the sizing of the vanes. To do so, it follows the approximation proposed by (Inaguma & Hibi, 2005) who associated the vane behavior to that of a cantilever

\

beam. As shown in Fig. 19 (Inaguma & Hibi, 2005), vane width is hence determined through static and fatigue calculation against pure bending phenomenon due to distributed, uniform load. In first approximation, the effect of the real pressure distribution of the fluid inside the chamber is neglected and the minor normal stresses due to the forced contact between the vane and the cam are not considered. Once that the vane size has been defined, the pump capacity is computed through Equation (14). Finally, two more verification are performed; the first one regards the radial suction port area A_p which must satisfy the condition that ensure the complete filling of the chamber considering a null vapor pressure.

$$C_d A_p \sqrt{\frac{2\,p_{in}}{\rho_{oil}}} \geq \omega \frac{dV_{ch}}{d\alpha} \tag{28}$$

The second condition regards the torsional strain of the rotor shaft $\Delta\vartheta_{max}$ which must be limited to avoid the jamming of the vanes due to the closure of the functional gap g. The maximum admissible strain can be computed as:

$$\Delta\vartheta_{max} = \frac{H}{R_i} \arctan\left(\frac{g}{H}\right) \tag{29}$$

Hence, assuming purely elastic strains and addressing with τ_v the overall torque for unit of axial length acting on the shaft, the following expression must be satisfied:

$$\Delta\vartheta_{max} > k_\vartheta \frac{\tau_v H^2}{2GJ} \tag{30}$$

Where k_ϑ is a corrective factor, G is the material shear modulus and J the moment of inertia of the resistant section.
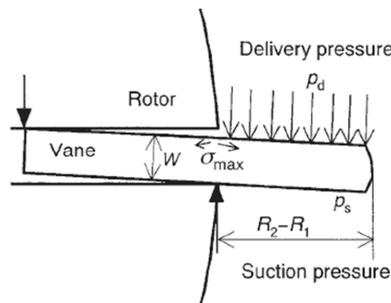
Figure 19: Simplified theory for vanes structural behavior

2.5.4 Benchmark results

A few comparison have been object of the benchmarking activity; at first, a trade-off on the maximum flow rate capability of each examined pump type is proposed as function of the reference speed and of the fluid pressure at the suction port. The delivery pressure is considered constant and equal to 400 psi. The investigation is performed ranging the reference speed from 4000 rpm to 15000 rpm.

Introducing the non-dimensional flow rate $\Theta = Q/(Q_{EG})_{n=4000rpm}$ as the ratio between the computed flow rate and the maximum flow rate capability for the external gears pumps at 4000 rpm, results are reported in Fig. 20 (a) for a pressure at the suction port equal to 15 psi and in Fig. 20 (b) for an inlet pressure of 5 psi.

For relatively high inlet pressures, the simplified design tools assess two prevalent pump types, that are the external gears pumps for low reference speed and the unbalanced vane pumps for high angular frequencies. Gerotor pumps with two feeding sides remains anyway competitive over the whole angular frequency span. Lowering the pressure at the suction port things change and vane pumps becomes more and more attractive. It is interesting to notice that gerotor devices remain competitive with the external gear pumps, while vane pumps with 6 vanes tends to provide higher values of non-dimensional flow-rate.
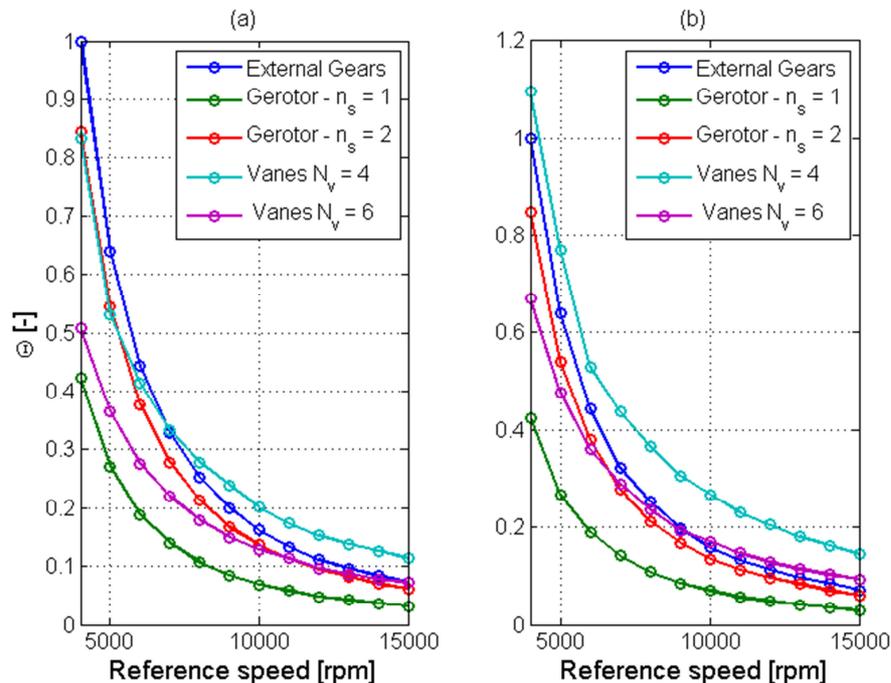
Figure 20: Flow-rate comparison: suction pressure 15 psi (a) – 5 psi (b)

\

The second comparison is carried out considering a fixed desired flow rate of 200 l/min, constant suction pressure of 14 psi and reference speeds in the range between 5000 and 10000 rpm. Objects of this comparison are the estimated weight and envelope of each selected pump types. Results are again reported in non-dimensional format as the ratio of each value over the reference obtained for the external gear pump at 5000 rpm. Looking at the results reported in Fig.21 (a), it is possible to notice that the estimated mass for the unbalanced vane pumps for the case under exam is inferior to the one computed for the gerotor and external gears options. It must be noted however that no particular care has been given to the design and weight optimization of the pumps' case and shafts; as such, the values of the non-dimensional mass parameter Ω should be used just to make a first, rough comparison between the selected pump types. This exam is moreover affected by the high value of required flow-rate, that might cause the need of pump stacking for some type of devices.

In Fig.21 (b) are reported the results of the envelope comparison, which highlight the most compact design of the gerotor and vane pumps with respect to the external gears type.
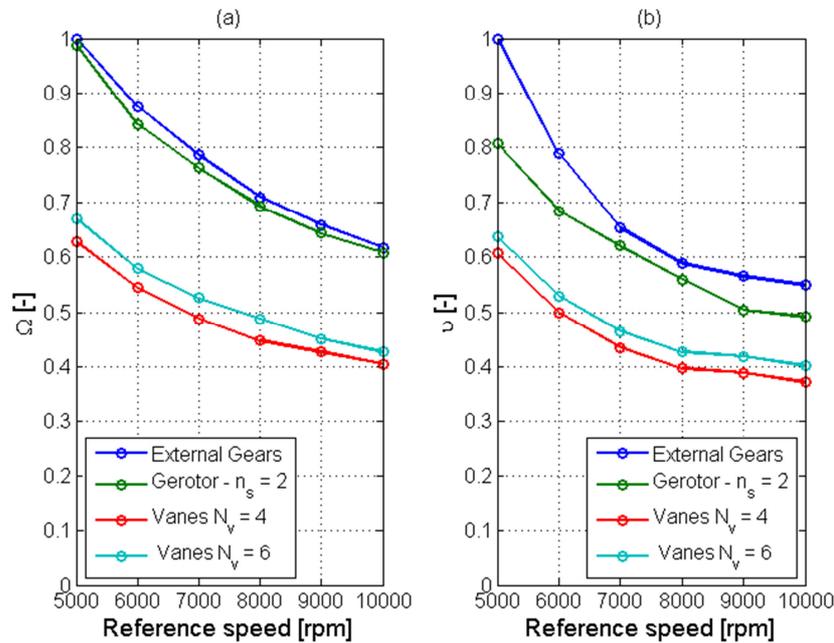
Figure 21: Mass (a) and envelope (b) comparison

Chapter 3

Novel concepts for gerotor pumps

3.1 Problem statement

The pumps trade-off performed in Chapter 2 highlighted the current capabilities of traditionally designed gerotor devices with respect to other solutions commonly employed in low-pressure systems. According to these analysis, gerotor pumps tend to be at disadvantage when searching for solutions able to provide high flow rate, since their maximum displacement for a given reference speed is between the 15% and the 40% less than the most performing option for the considered cases.

To increase the pump's maximum capacity it is necessary to find a way to increase the maximum volume of the fluid chambers, as per Equation (23). Since the radial dimension of the pump can't be overextended to avoid cavitation occurrence, as described by Equation (19), only two options remain: to act on the profile, or to find a way to generate axially longer pumps.

A few study to maximize the pump capacity working over the rotors profiles can be found in literature, such as (Beard, Yannitell, & Pennock, The effects of the generating pin size and placemen on the curvature and displacement of epitrochoidal gerotors, 1992), (Hsieh, Hwang, & Chang, Geometric design for a gerotor pump with high area efficiency, 2007) and (Bonadrini, Mimmi, & Rottenbacher, Design and simulation of meshing of a particular internal rotary pump, 2012). The improvements provided with the changes on the rotor profiles are however not enough to overcome the significant gap with other pump types.

\

On the other hand, to obtain gerotor pumps with increased axial length would be ideal to provide more significant advantages in generating higher flow-rates.

3.2 Introduction to radial-ports gerotor

For gerotor pumps, the main limitation in the definition of the axial length H of the rotors is the condition associated with the complete filling of the chambers. According to (Singh, 1991), applying the momentum conservation law in correspondence of a generic inlet port we obtain the following limit condition:

$$C_d A_p \sqrt{\frac{2 (p_{in} - p_v)}{\rho_{oil}}} \geq \frac{dV_{ch}}{dt} \tag{31}$$

Where V_{ch} is the volume at the time instant t of the considered pump chamber. Slightly modifying the expression to put in evidence the geometrical dependencies and considering a constant angular frequency, we have,

$$C_d A_p(\alpha) \sqrt{\frac{2 (p_{in} - p_v)}{\rho_{oil}}} \geq \omega H \frac{dA_{ch}(\alpha)}{d\alpha} \tag{32}$$

A_{ch} is the frontal area of the variable volume chamber for the angular position α. Considering the traditional axial port configuration, we have to consider that $A_p(\alpha) \leq A_{ch}(\alpha)$, while obtaining Equation (22) used in the simplified design tool described in Chapter 2. Let's consider now the hypothesis of a novel configuration where radial ports are obtained in the gap between two adjacent teeth of the outer rotor, as shown in the example of Fig. 22. Please notice that the geometry of the port is not the final one as the figure is purely intended to highlight their placement.
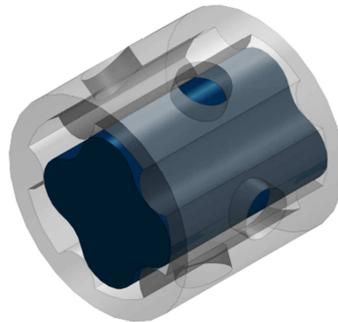
Figure 22: Concept of radial ports for gerotor pumps

Under the stated conditions, we have:

$$A_p(\alpha) = \Gamma_p H k_p(\alpha) \tag{33}$$

Γ_p is the length of the arc of circumference comprised within two adjacent lobes of the external rotor, H is the axial length and $k_p(\alpha)$ a factor theoretically ranging between 0 and 1, possibly function of the angular position.

Substituting Equation (33) inside Equation (32) we have:

$$C_d \Gamma_p H k_p(\alpha) \sqrt{\frac{2\,(p_{in} - p_v)}{\rho_{oil}}} \geq \omega H \frac{dA_{ch}(\alpha)}{d\alpha} \tag{34}$$

Finally leading to the limiting condition to ensure the complete filling of the chamber, described by Equation (35).

$$\begin{cases} \Gamma_p k_p(\alpha) \geq \dfrac{1}{C_d} \omega \dfrac{dA_{ch}(\alpha)}{d\alpha} \sqrt{\dfrac{\rho_{oil}}{2\,(p_{in} - p_v)}} \\ 0 \leq k_p(\alpha) \leq 1 \end{cases} \tag{35}$$

A few comments regarding the implications of Equation (35) must be provided. Comparing it with Equation (32), the first significant change is the disappearance of the axial length H; this means that the axial dimension of the pump is (theoretically) no more limited by issues related to incomplete filling of the chambers. The second significant observation is that the object of the condition, no more the axial length, is now the space available between the lobe of the outer rotor. Finally, it should be noted that the discharge coefficient C_d is not constant and mainly depends on the Reynolds' number of the fluid passing through the suction port and hence on the geometry of the port itself.

3.3 Design issues

Gerotor pumps overall performances are determined by the gears profile, since the rotors' shape defines:
- The maximum and minimum volume of the fluid chambers (pump capacity)
- The evolution of the fluid chambers' volume along a complete rotation (flow-rate profile and regularity)
- The contact stresses in the contact areas between the two rotors (pitting behavior)

\

- ▪ The sliding speed between the two rotors in the contact areas (wear rate and lubrication effectiveness)

Moreover, with the introduction of the radial ports configuration, the rotors profile also determines the final output of the condition regarding the complete filling of the chambers expressed by Equation (35), hence adding a further layer of complexity to their design. As such, rotors profiles need to be carefully and comprehensively studied and optimized. In the following chapters, the general mathematical framework used to describe gerotors profiles will presented while the tools developed to completely design and simulate a generic gerotor pump will be introduced. Hence, a first study showing the effect of the rotors shape over the pump performance is presented and its results discussed. Later on, profiles optimization is carried out; the employed methods described and the results highlighted.

Chapter 4

General theory for gerotors profiles

4.1 External rotor profile determination

To define the rotors geometry, the most efficient methods make use of closed form equations specific of certain profile type, as the one by (Mancò, Mancò, Rundo, & Nervegna, 2000) used for the simplified sizing tool in Chapter 2. Although being simple to implement in automatic procedures without requiring a heavy computational effort, those methods have limited applicability since it is not always possible to describe the inner gear profile through implicit functions (Mimmi & Pennacchi, Rotor design and optimization in internal lobe pumps, 1997). As such, the work proposed in this doctoral thesis makes use of a more general approach based on the Theory of Gearing by (Litving, 1989) and reported by authors such as (Litvin & Feng, Computerized design and generation of cycloidal gearings, 1996) and (Demenego, Vecchiato, Litvin, Nervegna, & Mancò, 2002) for its flexibility in describing non-circular profiles.

Following this approach and looking at Fig. 23, we introduce three reference frames:

- $(x, y)_{ext}$: reference system of the external (driven) rotor
- $(x, y)_{in}$: reference system of the inner (driving) rotor
- $(x, y)_f$ is the fixed reference frame of an external observer

The $(x, y)_{ext}$ frame and the fixed axis have their origin O_{ext} on the rotation axis of the external gear, while the origin O_{int} of $(x, y)_{in}$ sits on the rotation axis

\

of the inner gear. The gerotor eccentricity e can hence be defined as the distance between O_{ext} and O_{int}.
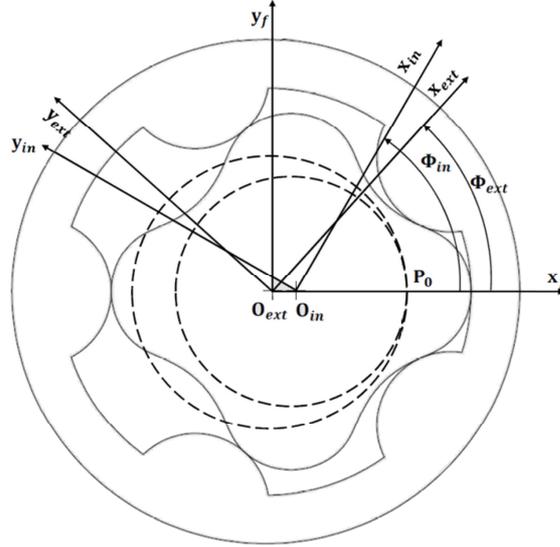
Figure 23: Reference systems for gerotor profile definition

The kinematics of two perfectly meshing gears can be described through a constant transmission ratio τ_{ie} equal to the ratio between the two pitch dimensions r_{ext} and r_{in}, and hence strictly dependent on the eccentricity e as shown through Equation (36).

$$\tau_{ie} = \frac{\omega_{in}}{\omega_{ext}} = \frac{r_{ext}}{r_{in}} = \frac{r_{ext}}{r_{ext} - e} = \frac{N}{N-1} \tag{36}$$

As shown in Fig. 24, it is possible to add a local reference system (χ, ψ) which origin C is related to the rotors geometry through its distance with O_{ext} $(\overline{CO_{ext}})$ and the eccentricity e. Defining the vectors $\boldsymbol{\Gamma}_{in}$ and $\boldsymbol{\Gamma}_{ext}$ as the inner rotor profile in the $(x,y)_{in}$ reference system and the external rotor geometry in its $(x,y)_{ext}$ frame, the following conditions must be verified:

$$\begin{cases} max(\|\boldsymbol{\Gamma}_{in}\|) = r_{lim,in} = \overline{CO_{ext}} - \rho_\chi + e \\ min(\|\boldsymbol{\Gamma}_{in}\|) = \overline{CO_{ext}} - \rho_\chi - e \\ max(\|\boldsymbol{\Gamma}_{ext}\|) = r_{lim,ext} = \overline{CO_{ext}} - \rho_\chi + 2e \\ min(\|\boldsymbol{\Gamma}_{ext}\|) = \overline{CO_{ext}} - \rho_\chi \end{cases} \tag{37}$$
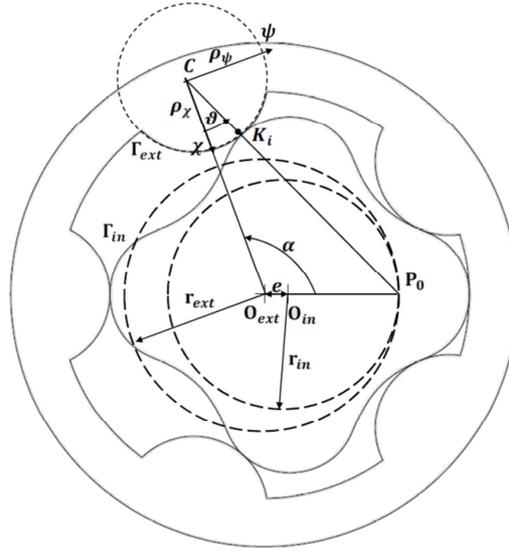
Figure 24: Geometrical parameters for gerotor profile definition

The ratio between $\overline{CO_{ext}}$ and r_{ext} can be addressed as λ and is of critical importance for the profile design. According to (Mimmi & Pennacchi, Rotor design and optimization in internal lobe pumps, 1997), the most convenient way to define the lobes geometry is through the use of parametric equations expressed in the local reference system (χ, ψ). In example, a good way to describe both circular and elliptic lobes in dependence of the factor k_{ell} can be considered.

$$\begin{cases} \chi = \rho_\chi cos(\xi) \\ \psi = k_{ell}\, \rho_\chi sin(\xi) \end{cases} \tag{38}$$

$$\begin{cases} tan(\vartheta) = k_{ell}\, tan(\xi) \\ \quad 0 \leq \xi \leq \pi \end{cases} \tag{39}$$

Hence, the distance r_k of the generic point K_i from the origin C of the local reference system can be computed as:

$$r_k = \overline{CK_\iota} = \rho_\chi \sqrt{cos^2(\xi) + k^2 sin^2(\xi)} \tag{40}$$

We now define the angular pitch $\Delta\alpha$ as:

$$\Delta\alpha = \frac{2\pi}{N} \tag{41}$$

\

Finally, the expression of the external profile $\boldsymbol{\Gamma}_{ext}$ in its own reference frame can be found given as the repetition of the lobes profiles around the external centrode axis.

$$\boldsymbol{\Gamma}^{ext}_{ext} = \begin{bmatrix} x_{ext} \\ y_{ext} \end{bmatrix} = \begin{bmatrix} cos(i\Delta\alpha) & -sin(i\Delta\alpha) \\ sin(i\Delta\alpha) & cos(i\Delta\alpha) \end{bmatrix} \begin{bmatrix} \overline{CO_{ext}} - r_k cos(\vartheta) \\ r_k sin(\vartheta) \end{bmatrix} \tag{42}$$

With $i = 1, \dots, N - 1$.

4.2 Internal rotor profile determination

The determination of the internal rotor profile is less straightforward, as it is obtained starting from the established geometry of the outer gear. By design, gerotor pumps are such that each point of the driving gear profile becomes a contact point in the meshing process once during its complete rotation. Hence, the profile of the internal rotor can be defined as the locus of the contact points between the two gears during a complete pump cycle expressed in the reference frame of the inner element.

According to the Theory of Gearing (Litving, 1989), the most convenient approach is to make use of homogeneous coordinates to express the external profile $\boldsymbol{\Gamma}_{ext}$ in the $(x, y)_{in}$ frame by means of the transformation matrix $\boldsymbol{M}_{in,ext}$:

$$\boldsymbol{\Gamma}^{in}_{ext} = \boldsymbol{M}_{in,ext} \begin{bmatrix} x_{ext} \\ y_{ext} \\ 1 \end{bmatrix} \tag{43}$$

The transformation matrix is function of the angular positions of the reference frames of the two rotors, namely ϕ_{in} and ϕ_{ext}, as shown in Fig. 23; its expression is given in Equation (44).

$$\boldsymbol{M}_{in,ext} = \begin{bmatrix} cos(\phi_{in} - \phi_{ext}) & sin(\phi_{in} - \phi_{ext}) & -e\,cos(\phi_{in}) \\ -sin(\phi_{in} - \phi_{ext}) & cos(\phi_{in} - \phi_{ext}) & e\,sin(\phi_{in}) \\ 0 & 0 & 1 \end{bmatrix} \tag{44}$$

Given the definition of the speed ratio for an ideal meshing given in Equation (36), we have:

$$\phi_{in} = \tau_{ie}\phi_{ext} \tag{45}$$

And hence the transformation matrix can be rewritten as a function of ϕ_{ext} and of the known parameter τ_{ie}.

$$\boldsymbol{M}_{in,ext} = \begin{bmatrix} cos[\phi_{ext}(\tau_{ie} - 1)] & sin[\phi_{ext}(\tau_{ie} - 1)] & -e\,cos(\tau_{ie}\phi_{ext}) \\ -sin[\phi_{ext}(\tau_{ie} - 1)] & cos[\phi_{ext}(\tau_{ie} - 1)] & e\,sin(\tau_{ie}\phi_{ext}) \\ 0 & 0 & 1 \end{bmatrix} \quad (46)$$

With $0 \leq \phi_{ext} \leq 2\pi$.

To define the contact points without having one of the gears, we exploit the gearing rule according to which, *during meshing, the normal to the gears profiles in the contact point(s) always passes through the instantaneous centre of rotation of the relative motion between the two gears* (Litving, 1989).

For gerotor devices, the centre of rotation P_0 is at the intersection between the two centrodes; its coordinates (X_0, Y_0) in the reference system $(x, y)_{ext}$ can be expressed as follows.

$$\begin{cases} X_0 = r_{ext}cos(\phi_{ext}) \\ Y_0 = -r_{ext}sin(\phi_{ext}) \end{cases} \quad (47)$$

For a given external profile $\boldsymbol{\Gamma}_{ext}$, we can compute the normal to each point of its lobes as

$$\boldsymbol{N}_{ext} = \begin{bmatrix} N_X \\ N_Y \\ 1 \end{bmatrix} = \frac{\partial \boldsymbol{\Gamma}_{ext}^{ext}}{\partial \xi} \times \boldsymbol{k}_{ext} \quad (48)$$

Where $\boldsymbol{k}_{ext}$ is a unit vector directed along the direction normal to the $(x, y)_{ext}$ plane and right-handed verse. To be valid, Equation (48) demands the satisfaction of a few requirement, that are:

- $\boldsymbol{\Gamma}_{ext}$ is continuous over its entire domain
- $\boldsymbol{\Gamma}_{ext}$ first derivative is continuous over its entire domain
- $\partial\boldsymbol{\Gamma}_{ext}/\partial\xi \neq 0$ over its entire domain

Given the previously mentioned rule, a generic point on the external rotor of coordinates (X_{ext}, Y_{ext}) in the $(x, y)_{ext}$ reference system is a contact point for the ϕ_{ext} angular position of the external gear if the normal to the profile in that point passes through the centre of rotation P_0 of the relative motion between the two gears. Expressed in mathematical form, this condition becomes

$$f(\xi, \Phi_{ext}) = \frac{X_0 - X_{ext}}{Y_0 - Y_{ext}} - \frac{N_X}{N_Y} = 0 \quad (49)$$

\

The final expression of the inner rotor profile $\boldsymbol{\Gamma}_{in}$ is hence provided combining Equations (43) and (49):

$$\boldsymbol{\Gamma}_{in}^{in} : \begin{cases} \boldsymbol{\Gamma}_{ext}^{in}(\xi, \Phi_{ext}) = \boldsymbol{M}_{in,ext}\boldsymbol{\Gamma}_{ext}^{ext} \\ f(\xi, \Phi_{ext}) = 0 \end{cases} \qquad 0 \leq \phi_{ext} \leq 2\pi \qquad (50)$$

An alternative approach can be found in (Mancò, Mancò, Rundo, & Nervegna, 2000)

4.3 Handling of undercutting conditions

Undercutting occurs when the geometry of the outer gear is such to generate singular points in the inner rotor profile. Such points are obviously unacceptable; as such, conditions that lead to undercutting must be detected and avoided.

According to (Litvin & Feng, Computerized design and generation of cycloidal gearings, 1996) and (Vecchiato D. , Demenego, Argyris, & Litvin, 2001), singular points can be detected by studying the velocity $\boldsymbol{v}_k^{in}$ of the generic k-th contact point in its own motion over the inner rotor profile $\boldsymbol{\Gamma}_{in}$. Undercutting occurs wherever the velocity is null. This condition can be expressed as the combined motion of the contact point velocity over the outer profile $\boldsymbol{v}_k^{out}$ and the relative motion between the two gears $\boldsymbol{v}_r$ as:

$$\boldsymbol{v}_k^{in} = \boldsymbol{v}_k^{out} + \boldsymbol{v}_r = \boldsymbol{0} \qquad (51)$$

Expressed in the reference system $(x, y)_{ext}$, Equation (51) becomes:

$$\begin{cases} \dfrac{\partial x_{ext}}{\partial \vartheta} \dfrac{\partial \vartheta}{\partial t} = -v_{r,x} \\ \dfrac{\partial y_{ext}}{\partial \vartheta} \dfrac{\partial \vartheta}{\partial t} = -v_{r,y} \end{cases} \qquad (52)$$

While differentiating the equation of meshing reported in Equation (49) we may have:

$$\frac{\partial f}{\partial \vartheta} \frac{\partial \vartheta}{\partial t} = -\frac{\partial f}{\partial \Phi_{ext}} \frac{\partial \Phi_{ext}}{\partial t} \qquad (53)$$

Combining Equations (52) and (53) we get a system of three linear equations in the only unknown $\partial \vartheta / \partial t$, which admit a valid solution only if the rank of its augmented matrix, reported in Equation (54), is one.

$$
\begin{bmatrix}
\dfrac{\partial x_{ext}}{\partial \vartheta} & \dfrac{\partial y_{ext}}{\partial \vartheta} & \dfrac{\partial f}{\partial \vartheta} \\[2em]
-v_{r,x} & -v_{r,y} & -\dfrac{\partial f}{\partial \Phi_{ext}}\dfrac{\partial \Phi_{ext}}{\partial t}
\end{bmatrix}^{T}
\qquad (54)
$$

This condition, further manipulated, allows to obtain Equation (21) for the cycloidal case.

\

Chapter 5

Theory for gerotor pump design and simulation

5.1 Design loop concept

In Chapter 4 we introduced a general mathematical description for the gerotor pumps profiles and the theoretical bases to check its geometrical validity. Although necessary to draw formally correct profiles, geometrical validity alone is not sufficient to design a properly operating gerotor pump.

We hence introduce the concept of design loop for gerotor pumps with the aid of Fig. 25, while a more accurate description of each passage will be provided in the remaining sections of this chapter. The information required to start the design loop can be divided in two main categories, that are: the design inputs and the design parameters. Design inputs are the information related to the expected operating conditions that the pump will have to face. In first approximation, we may have:

- p_{in}: minimum pressure at the suction port
- p_{out}: maximum pressure at the delivery port
- n_{ref}: reference speed of the driving gear
- Q_{ref}: the expected flow-rate for reference conditions
- T_{ref}: fluid temperature for the reference condition
- Fluid type and characteristics

On the other hand, design parameters are those geometrical quantities that can be defined by the pump designer and that determine the geometry of the rotors' profiles. At least three parameters, the non-dimensional λ, the eccentricity e and the teeth number in the outer rotor N, can be identified for the cycloidal profile, while any addition depends on the selected geometry for the outer gears' lobes.

Chosen the design parameters, the rotors geometry is determined an checked for singularities while the suction and delivery ports can be designed. Hence several design constraints related with the pump dimensions can be checked:

- Complete filling of the variable volume chambers
- Eventual envelope limitations over the axial length of the pump
- Minimum diameter of the driving shaft

If every check is passed, the pump can be studied as a dynamic system to predict its performance under nominal and off-nominal operating conditions. If the performance requirements are met, the rotors can be considered acceptable and exit the design loop. If any of the design checks (geometrical constraints, requirements over the projected performances in nominal or off-nominal conditions etc.) are not met, a novel set of design parameters must be defined.
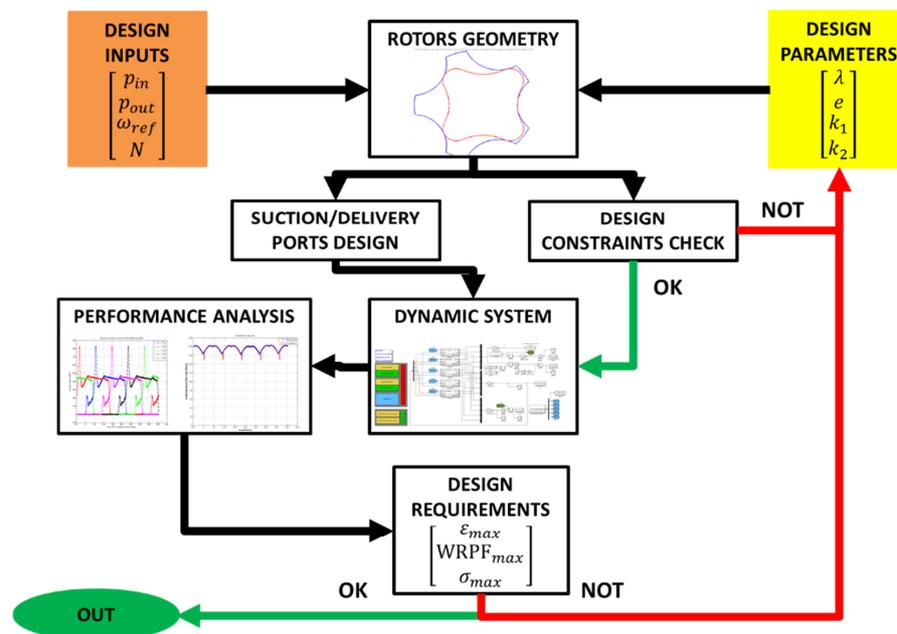
Figure 25: Design loop for gerotor pumps

\

5.2 Major design constraints

Other than the geometrical issues described in Chapter 4, the design of the rotors profiles is also determined by the pump operating conditions. To avoid cavitation is in fact necessary to keep the fluid velocity under a limiting value that can be defined as,

$$v_{lim} = \frac{1}{k_s} \sqrt{\frac{2(p_{in} - p_v)}{\rho_{oil}}} \tag{55}$$

This value mainly depends on the fluid pressure at the inlet port p_{in}, the fluid vapour tension at operating temperature p_v and its density ρ_{oil}; a safety factor $k_s \geq 1$ is added to consider the occurrence of unpredictable off-nominal conditions. The dependence of the fluid density over its temperature T is usually described trough proper maps provided by the fluid supplier, while the vapour pressure can be in first approximation computed through the Antoine equation:

$$\log p_v = A - \frac{B}{C + T} \tag{56}$$

In gerotor pumps the highest fluid velocity zones are in proximity of the rotors maximum radial dimension and since the fluid velocity can be considered in first approximation equal to the linear speed of the pump gears, the maximum radius for the inner rotor $r_{lim,in}$ and the external gear $r_{lim,ext}$ at the reference speed ω_{in} can be computed as:

$$\begin{cases} r_{lim,in} = \dfrac{v_{lim}}{\omega_{in}} = \dfrac{1}{k_s} \sqrt{\dfrac{2(p_{in} - p_v)}{\rho \omega_{in}^2}} \\[4mm] r_{lim,ext} = \dfrac{v_{lim}}{\omega_{ext}} = \dfrac{1}{k_s} \sqrt{\dfrac{2(p_{in} - p_v)}{\rho \left(\dfrac{\omega_{in}}{\tau_{ie}}\right)^2}} \end{cases} \tag{57}$$

Combining equations (37) and (57) an important design constraint linking the pump geometry to its operating conditions can be found.

$$r_{lim,in} + e \leq r_{lim,ext} \leq \sqrt{\frac{2(p_{in} - p_v)}{\rho \left(\dfrac{\omega_{in}}{\tau_{ie}}\right)^2}} \tag{58}$$

This constraint is easily verified after the definition of the rotors profiles.

Low inlet pressure is also responsible of another design limitation, related to the occurrence of incomplete filling of the chambers. Depending on the employed ports type, this condition has an effect on the maximum axial length (axial ports) or a strict requirement over the space available between the lobes of the external rotor (radial ports). In the first case, the condition can be expressed by slightly modifying Equation (22)

$$H \leq \frac{1}{k_{ch}} A_p \frac{n_s \sqrt{\frac{(p_{in} - p_v)}{\rho_{oil}}}}{\omega \frac{dA_{ch}}{d\alpha}} \tag{59}$$

Where $k_{ch} \geq 1$ is a safety coefficient. Given the rotors profiles, the axial length needed to supply the required flow-rate Q_{ref} at the reference speed ω_{ref} can be easily computed inverting Equation (23). Equation (59) becomes as such a condition over the required flow rate.

$$\frac{Q_{ref}}{\omega_{ref}(N-1)A_{ch}} \leq \frac{1}{k_{ch}} A_p \frac{n_s \sqrt{\frac{(p_{in} - p_v)}{\rho_{oil}}}}{\omega_{ref} \frac{dA_{ch}}{d\alpha}} \tag{60}$$

Which can be rewritten as:

$$Q_{ref} \leq \frac{(N-1)A_{ch}A_p}{k_{ch}} \frac{n_s \sqrt{\frac{(p_{in} - p_v)}{\rho_{oil}}}}{\frac{dA_{ch}}{d\alpha}} \tag{61}$$

This constraint is hence easily verified once that the rotors profiles have been defined. On the other side, the condition to respect to endure complete filling of the chamber in the radial ports case is described by Equation (35), here reported for clarity.

$$\begin{cases} \Gamma_p k_p \geq \frac{1}{C_d} \omega \frac{dA_{ch}}{d\alpha} \sqrt{\frac{\rho_{oil}}{2(p_{in} - p_v)}} \\ 0 \leq k_p \leq 1 \end{cases} \tag{62}$$

To compute the available circumferential space Γ_p we consider the situation described in Fig. 26. The generic extreme of the external rotor's lobe A_i, has coordinates (x_A, y_A) in the reference frame $(x, y)_A$. Since it can be identified as

\

the intersection between the external lobe described by Equations (38,39) and the circumference with radius r_e and center in O_{ext}, we have:

$$\begin{cases} x_A = \dfrac{\overline{CO_{ext}}k_{ell}^2 + \sqrt{r_e^2(1 - k_{ell}^2) + \rho_\chi^2 k_{ell}^2(k_{ell}^2 - 1) + \overline{CO_{ext}}^2 k_{ell}^2}}{(k_{ell}^2 - 1)} \\ y_A = \sqrt{r_e^2 - x_A^2} \end{cases} \qquad (63)$$

Hence the angle $\Delta\alpha_i$, that is the angular span occupied by half a tooth, can be identified as:

$$\Delta\alpha_i = \arcsin\left(\frac{y_A}{r_e}\right) \qquad (64)$$

And finally the available space between the teeth of the external rotor can be computed as follows:

$$\Gamma_p = \frac{2\pi r_e - 2\Delta\alpha_i r_e N}{N} \qquad (65)$$

As such, once that the profile has been defined, the condition on the radial ports can be easily verified through the implementation of algebraic equations in the simulation tool's code.
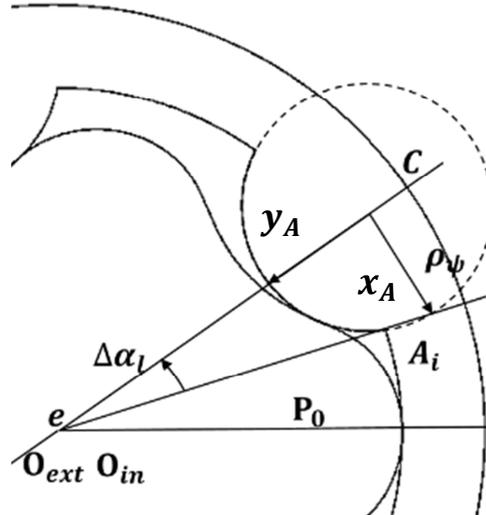
Figure 26: Determination of the circumferential length for radial ports

5.3 Pump dynamic model

The pivotal point of the whole design loop is the study of the gerotor pump as a dynamic system. This passage can be performed by realizing and testing a prototype or by preparing a model of the system to simulate the gerotor behaviour. As shown in Fig. 27, three flow rates affecting a generic *i-th* chamber of V_i volume can be identified. $Q_{p,i}$ is the flow rate exchanged with the external environment, while $Q_{i-1,i}$ and $Q_{i,i+1}$ are the leakages between the *i-th* chamber and the adjacent ones.
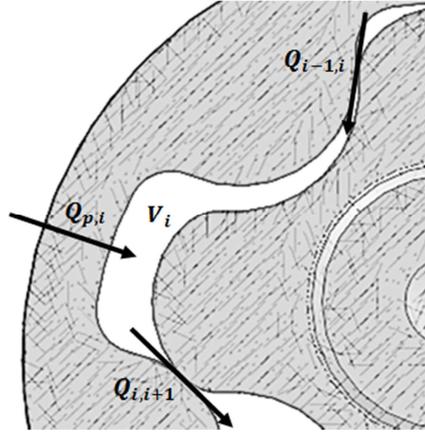
Figure 27: Flow rate balance for a variable volume chamber

The flow rate through the *i-th* port $Q_{p,i}$ depends on the pressure difference between the external environment and the chamber, as well as on the port dimensions and on the fluid properties according to the following expression.

$$Q_{p,i} = sign(p_P - p_i)C_d A_p \sqrt{\frac{2|p_P - p_i|}{\rho_{oil}}} \tag{66}$$

Where p_P and p_i are the environment and the chamber pressures, ρ_{oil} is the fluid density and A_p is the port area seen by the *i-th* chamber, which value is defined by the rotors position. The discharge coefficient C_d is instead depending on the fluid Reynolds number computed in the port section; its values are obtained through the expressions proposed in (Viersma, 1980). Leakages between adjacent chambers can modelled using the Hagen-Poiseuille law for gaps with rectangular section (Jelali & Kroll, 2003).

$$Q_{i-1,i} = (p_{i-1} - p_i)\frac{H h_g^3}{12\mu l_g} \tag{67}$$

\

Where H is the gerotor axial dimension, h_g is the gap height and l_g is the gap length in the direction of the leakage, while μ is the dynamic viscosity of the fluid. The net flow rate across the single chamber Q_i can hence be computed through Equation (68), where the adopted sign convention generates positive values during volume filling and negative during fluid discharge.

$$Q_i = Q_{p,i} + Q_{i-1,i} - Q_{i,i+1} \qquad (68)$$

Applying the continuity equation to the examined control volume it is possible to link the net flow rate Q_i with the chamber geometry variation and the consequent changes in fluid pressure p_i through the Bulk modulus β.

$$Q_i - H\frac{dA_{ch}}{dt} = \frac{V_i}{\beta}\frac{dp_i}{dt} \qquad (69)$$

Where the chamber frontal area A_{ch} is a function of the inner rotor position. The instantaneous flow rate delivered by the pump can be computed by summing only the negative contributes of Q_i, while paying attention to eventually subtract the quote due to leakage between the external rotor and its tracks $Q_{s,r}$.

$$Q = -\sum_{i=1}^{N} Q_i|_{Q_i<0} - Q_{s,r} \qquad (70)$$

The leakages between the pump rotating parts and its stator are again evaluated according to the Hagen-Poiseuille law, where p_{in} and p_{out} are the inlet and outlet port pressures (Jelali & Kroll, 2003).

$$Q_{s,r} = (p_{out} - p_{in})\frac{Hh_{grs}^3}{12\mu l_{grs}} \qquad (71)$$

The net useful torque acting on the driving gear $T(\phi_{in})$ can be hence obtained through the application of the power conservation principle:

$$T(\phi_{in}) = \frac{Q(p_{out} - p_{in})}{\omega_{in}} \qquad (72)$$

Notice that the results obtained through equation (72) are valid only if the gerotor pump is in motion. Given the simulation results, a rapid check is performed to detect any evidence of cavitation inception; addressing with $p_i(t)$ the simulated pressure in the *i-th* chamber at the simulation time t, the following expression must be verified.

$$\begin{cases} p_i(t) > p_v \\ \forall i \ 1 \leq i \leq N \\ \forall t \ t_0 \leq t \leq t_{end} \end{cases} \tag{73}$$

Where t_0 and t_{end} are the simulation time related to the beginning and the end of the data acquisition. The dynamic model has been implemented using Matlab\Simulink software, but the provided equations have general validity and can be employed into any other coding language.

5.4 Design of suction and delivery ports

As well introduced in Section 5.2, the correct design of the suction and delivery ports is critical for the pump's operation and health. For the suction port, as well described by Equations (59) and (62), the main design issue is related to its under sizing, that lead to the incomplete filling of the chambers and to cavitation inception.
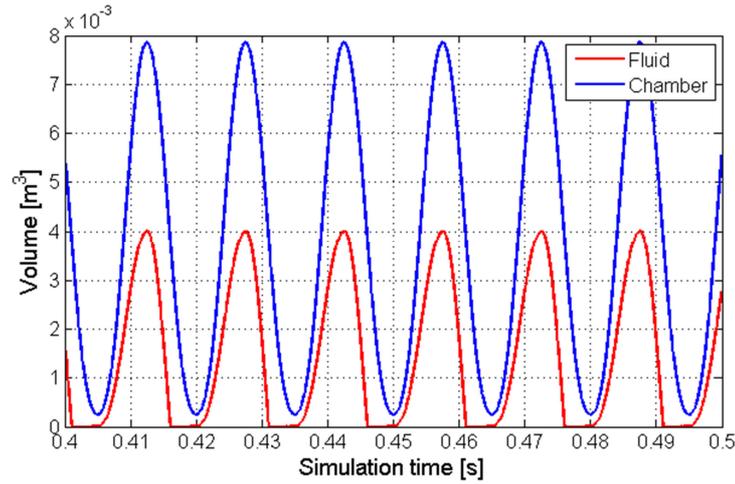
Figure 28: Effects of under sizing of the suction port

By looking at Figure 28, we define the filling ratio X_f as:

$$X_f = \frac{\max(V_{fl})}{\max(V_{ch})} \tag{74}$$

According to (Singh, 1991) and to the equations provided in Section 5.2, it is however possible to compute for each angular position of the chamber the minimum suction port area required to avoid cavitation for the considered operating conditions.

\

The definition of the delivery port is less impactful on the overall pump design when dealing with low-pressure systems, but is nonetheless fundamental. During the delivery phase, the fluid inside the considered variable volume chamber is subjected to a significant pressure variation; during the first stages of the delivery, the pressure quickly raises due to the effect of the high-pressure delivery environment and a limited amount of backflow may be observed. Following the first stages, the delivery process is governed by the contraction of the chamber's volume, which generates the flow-rate leaving the pump. Focusing on the delivery port and a single chamber we can slightly elaborate Equation (66) and write,

$$Q_{p,i} = \text{sign}(p_{out} - p_i)C_d A_p \sqrt{\frac{2|p_{out} - p_i|}{\rho_{oil}}} \tag{75}$$

Considering a fixed angular frequency for the driving gear, the theoretical flow rate may be considered as constant, as well as the delivery pressure. Hence, the main factor affecting the fluid pressure inside the chamber is the area of the delivery port itself. If the delivery port is undersized, the fluid inside the chamber is not able to completely leave the pump, leading to a pressure increase that may be unsustainable for the structural integrity of the device, as shown in Fig. 29. Moreover, the delivery port design must be carefully tuned in order to avoid excessive pressure spikes during the first and the last stages of the delivery process that can possibly affect the fatigue life behavior of the inner rotor's shaft and of its supports.
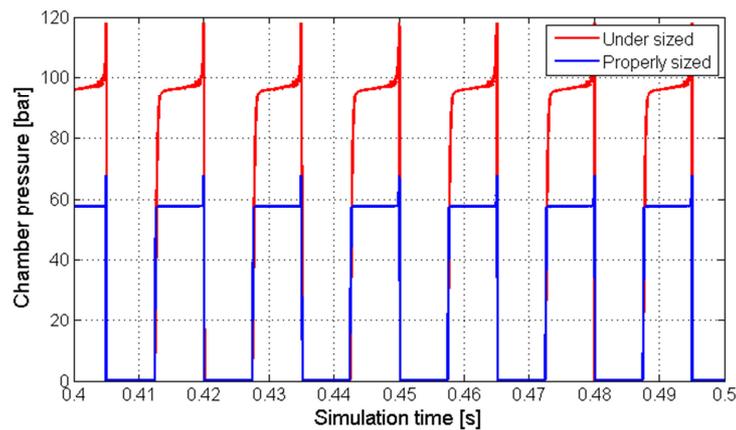
Figure 29: Effects of under sizing of the delivery port (57 bar delivery)

As for Figure 29, we define the delivery ratio X_d as:

$$X_d = \frac{\min(V_{fl})}{\min(V_{ch})} \tag{76}$$

To quickly design both suction and delivery ports, the following procedure is adopted. At first, we consider a simplified approach making use of:

- Non compressible fluid (flow rate equal to the volume variation in the chambers)
- Fixed suction and delivery pressures
- Constant discharge coefficient $C_d = 0.61$

Since the vapor tension p_v for the employed fluid is known, we can fix an acceptable chamber pressure during the delivery p_i and hence compute, for each angular position of the inner rotor, the corresponding port area thanks to Equation (66). Hence the obtained values $A_p(\alpha)$ are used inside the dynamic model to verify the pump behaviour under more realistic hypothesis, such as compressible fluid and variable discharge coefficient. A simulation is run using the design conditions and the associated values of the filling and delivery ratio are computed. These values are hence used to modify the ports area in the suction and delivery phase as follows.

$$\begin{cases} A_p(\alpha)' = \dfrac{1}{X_f} A_p(\alpha) & \alpha < \pi \\ A_p(\alpha)' = X_d A_p(\alpha) & \alpha \geq \pi \end{cases} \tag{77}$$

Hence further simulations are performed and the process iterated until the results are acceptable. An example of the chamber's and ports' areas is reported in Fig. 30 as functions of the driving gear position. Please notice that the ports area is higher than the frontal area of the chamber for some extended angular span; this is possible only for the radial ports configuration and highlights that this option would allow to design pumps working with operating conditions unsustainable for the axial ports case. The asymmetry between suction (up to 180°) and delivery is due to the different pressure drop imposed on them; in this particular case, the acceptable pressure difference on the delivery port is higher than the one demanded on the inlet port. This is not the case if the pump is designed to be driven in both direction at the same speed during its operative life; under this assumption, the behavior of the ports area must be symmetric over the suction and delivery phases.

\
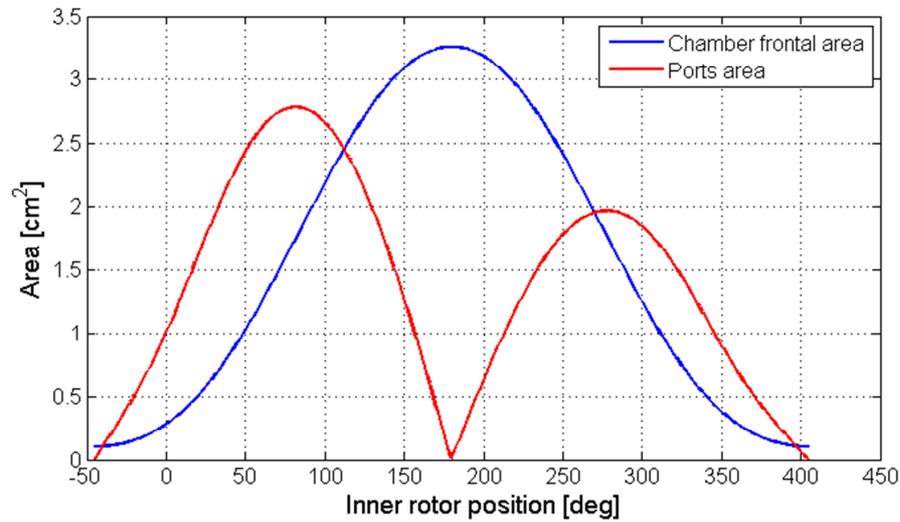
Figure 30: Ports vs chamber behavior (radial port configuration)

5.5 Evaluation of contact pressures in multi-contact scenario

The determination of the contact stresses in the rotor profiles is made difficult by several factors related to the nature of the meshing process and the presence of the pumped fluid. The first issue is represented by the number of contact zones, which is variable inside one pump cycle and possibly affected by non-uniform clearance distribution. Moreover, the load repartition is unknown a-priori making a direct computation of the contact forces impossible. Further, lubrication regime is affected by operating conditions, so that the actual contact pressure distribution is not constant in time. In order to obtain a first-approximation analysis while keeping the computational time within reasonable limits, an iterative approach similar to the one proposed by (Gamez-Montero, Castilla, Khamashta, & Codina, 2006) is applied.

The described method is based on the following simplifying hypothesis:

- The rotors are perfectly crafted (no geometrical errors)
- No clearances between the gears
- Lubrication effect is neglected
- Gears support are treated as rigid bodies, hence the deformations due to the contact forces developed during meshing are located only in the gears' teeth

Following this approach, force exchange between mating teeth is supposed to occur only along the suction side of the pump, as shown in Fig. 31. Gearing in the portion of the device connected to the delivery environment is instead considered as a purely geometry coupling.

The application of a small arbitrary rotation $\delta\phi_{in}$ to the inner rotor causes the interpenetration w_i between the teeth of the two gears. According to Hertz theory it is then possible to determine the contact forces vector $\boldsymbol{F}_c$ as for (Johnson, 1985):

$$\boldsymbol{F}_c = \frac{\pi H}{4\left(\dfrac{1-v_{in}^2}{E_{in}} + \dfrac{1-v_{ext}^2}{E_{ext}}\right)}\boldsymbol{w} \tag{78}$$

H is the rotors axial length, E and v the Young modulus and the Poisson coefficient for the two gears. The vector $\boldsymbol{w} = [w_1 \quad w_2 \quad \cdots \quad w_N]^T$ contains the interpenetration distance for each contact point. Its element w_i are non-zero only when measured in the active zone.

Considering frictionless contacts we can express the net resistant torque acting on the driving shaft through the contributes of each contact force $F_{c,i}$.

$$T(\phi_{in}) = \sum_{i=1}^{N} d_i F_{c,i} \sin\gamma \tag{79}$$
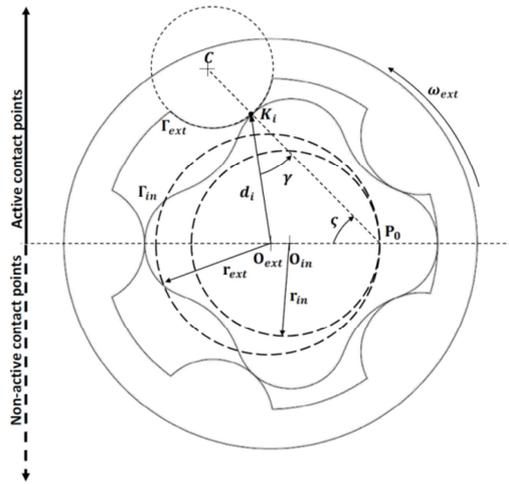
Figure 31: Considerations for contact force estimate

\
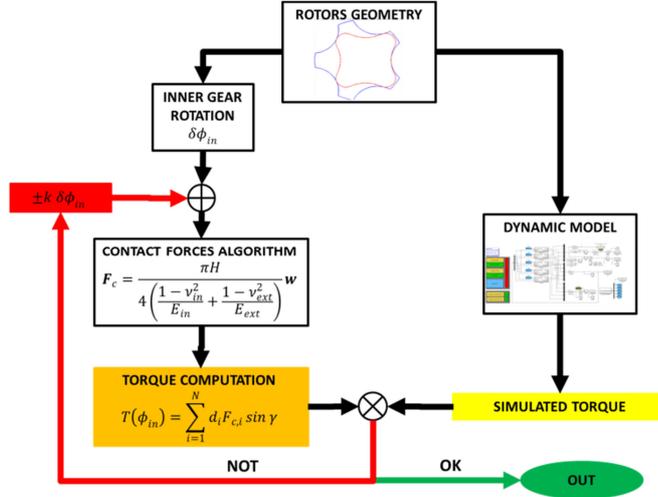
Figure 32: Algorithm for contact forces estimate

Since the overall resistant torque has been computed by the dynamic model through Equation (72), it is then possible to estimate the contact forces $F_{c,i}$ by means of an iterative procedure. Given an arbitrary $\delta\phi_{in}$ we can compute the correspondent $T(\delta\phi_{in})$ through Equations (78) and (79). This torque value is hence compared with a reference signal obtained through the dynamic model simulation: if the difference falls below a tuneable threshold the results are accepted and the contact forces value saved. Otherwise a proper variation is applied to $\delta\phi_{in}$ and the procedure repeated, as well described in Fig. 32. The contact stresses σ_i for each tooth can hence be computed as

$$\sigma_i = \frac{2F_{c,i}}{\pi a_i H} \tag{80}$$

Where the contact area characteristic dimension a_i is determined considering the formulas available in literature for cylinder on cylinder contact:

$$a_i = \sqrt{\frac{4F_{c,i}\left(\dfrac{1-v_{in}^2}{E_{in}} + \dfrac{1-v_{ext}^2}{E_{ext}}\right)}{\pi H\left(\rho_{int,i} + \rho_{ext,i}\right)}} \tag{81}$$

The external and the internal profiles curvatures for the *i-th* contact point $\rho_{ext,i}$ and $\rho_{int,i}$ can be easily obtained considering the geometrical properties of the selected lobes. The maximum values of contact stress are then compared to the material limit for static and repeated Hertzian contact. The contact stress estimation method and the effect of the use of a coupled dynamic model have

been verified through FEM analysis performed on a reference radial port gerotor. The reference case has been designed for a 14 psi inlet pressure and 5000 rpm speed of the driving gear. The pressure of the delivery environment is supposed to be fixed and equal to 500 psi, while the geometry parameters used for the example case are $e = 3.5mm$ and $\lambda = 1.8$; a simplified render of the pump geometry can be found in Fig. 33. The gerotor axial length has been over imposed as $H = 0.4\,R_{ext}$.
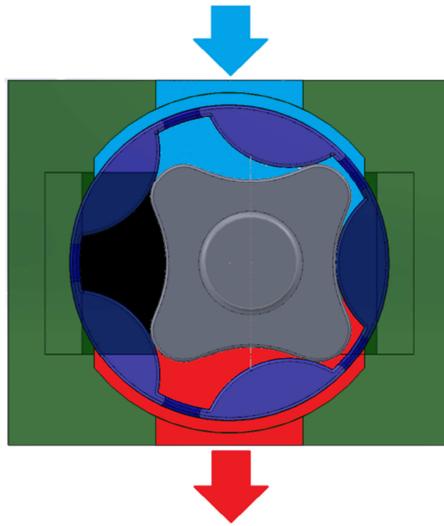
Figure 33: Geometry of the example case

The analysis has been conducted using over 8E5 tetrahedral cells while applying several congruent rotation to the inner and outer rotors. For each angular position, the chambers pressure and the input torque have been imported from the dynamic model simulation results reported in Fig. 34.
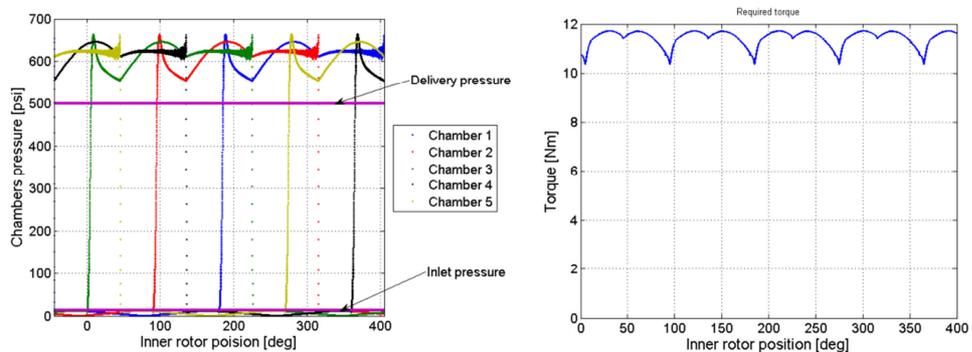
Figure 34: Fluid pressures (left) – simulated net torque (right)

\

The mesh generated for the two rotors for a given position and an example of the FEM analysis results are reported in Fig. 35; in Fig. 36 are instead compared the results of the FEM study with those coming from the presented algorithm declined in two different version:

- In blue: the reference torque used inside the algorithm for the evaluation of the contact forces is coming from the dynamic model and is, as such, dependent on the inner rotor position
- In red: the reference torque is a constant average value over a complete revolution of the inner rotor

In both cases, the trend of the algorithm results is coherent with the FEM data, even though some deviation in the numerical values can be noticed. Focusing on the contact pressure behaviour it is possible to notice two major peaks. The first one occurs during the beginning of the gear meshing and is due to the change in the sign of the inner rotor curvature; the second peak is due to the variations in the number of meshing teeth. Moreover, it can be observed that the integration of the dynamic model allows to obtain a higher level of detail in estimating the contact stresses behaviour, in particular during the first stages of the meshing process. The constant torque version of the algorithm tends to overestimate the stress peak, while failing to properly describe the contact behaviour at the beginning of the rotation. As a side note, it can be observed that the peak of the contact pressure behaviour may cause issues with the contact surface fatigue behaviour; this is mainly due to the pressure drop imposed between inlet and delivery environments that is usually lower than the one imposed for the comparison.
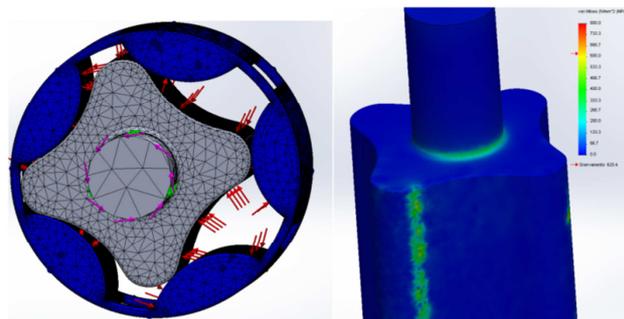
Figure 35: Rotors' mesh (left) – FEM result example (right)
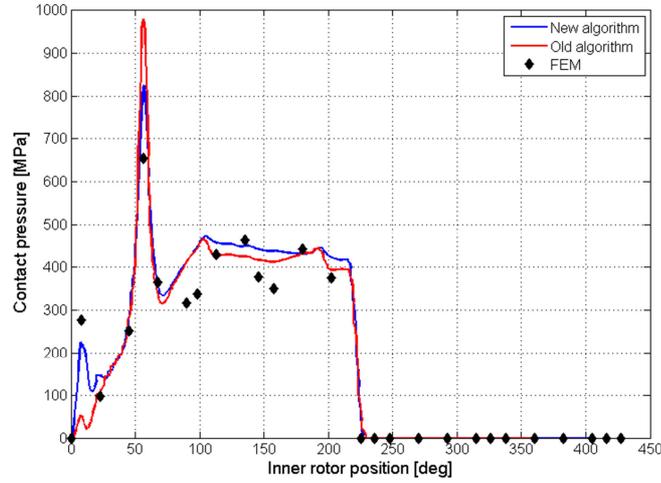
Figure 36: Comparison between FEM and iterative algorithm

5.6 Shaft design

The driving shaft integral with the inner gear is subjected to multi-axial stress conditions due to the contemporary effects of the pressure drop between delivery and suction sides of the pump, contact forces between the gears during meshing and the torsional effect generated by the driving and resistant torque. Addressing with the maximum diameter of the shaft, the following condition must be verified:

$$min(\|\boldsymbol{\Gamma}_{in}\|) = \overline{CO_{ext}} - \rho_\chi - e < \frac{D_{shaft}}{2} \tag{82}$$

To properly tackle the shaft design issues, the first step is to study the static equilibrium of the inner rotor. As described in Fig. 37 and considering the fixed $(x, y, z)_f$ reference frame, the inner rotor can be considered in first approximation subjected essentially to:

- Bending over the $(x, z)_f$ plan due to the combined effect of the distributed load associated with the pressure drop $(p_{out} - p_{in})$ and the contact forces $F_{C,x}$, in first approximation considered as uniformly distributed over the axial length of the pump
- Bending over the $(y, z)_f$ plan due to the component $F_{C,y}$ of the contact forces
- Torsion over the z_f axis due to the concentrated driving torque T_{in} and the distributed resistant torque t_r

\
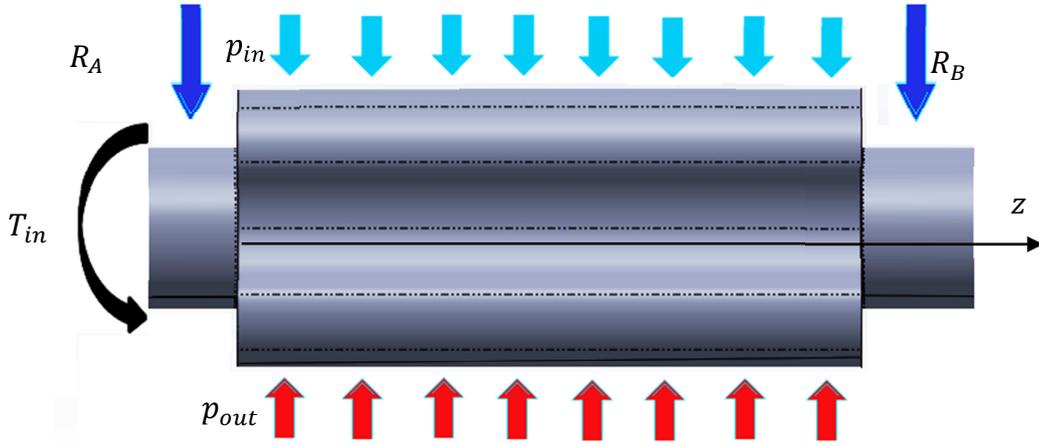
Figure 37: Static equilibrium of the inner rotor shaft

In first approximation we may consider as negligible the effect of the friction forces in the contact points and cover this assumption with the use of safety coefficients. Under these hypothesis, and considering the $(x, z)_f$ and $(y, z)_f$ plans, we may compute the reaction forces in the shaft supports as follows.

$$
\begin{cases}
R_{A(x,z)} = R_{B(x,z)} = \dfrac{1}{2}\left((p_{out} - p_{in})A_l - \sum_{i=1}^{N} F_{C,x} \right) \\
R_{A(y,z)} = R_{B(y,z)} = \dfrac{1}{2}\left(-\sum_{i=1}^{N} F_{C,y} \right)
\end{cases} \tag{83}
$$

The bending moments on the two considered plans can hence be defined as:

$$
\begin{cases}
M_{f(x,z)} = \dfrac{1}{2}\left((p_{out} - p_{in})\dfrac{A_l}{H} - \sum_{i=1}^{N} \dfrac{F_{C,x}}{H} \right)z^2 - R_{A(x,z)}z \\
M_{f(y,z)} = \dfrac{1}{2}\left(-\sum_{i=1}^{N} \dfrac{F_{C,y}}{H} \right)z^2 - R_{A(x,z)}z
\end{cases} \tag{84}
$$

The torsional moment can be instead computed as follows, reminding that the input torque is at regime equal to the resistant torque assumed as uniformly distributed along the axial length of the shaft.

$$M_{t(z)} = \frac{T_{in}}{H}(H - z) \tag{85}$$

The first tentative diameter as a function of the axial coordinate can be computed according to (Budynas & Nisbett, 2014).

$$D(z) = \left(\frac{32}{\pi(R_m/10)}\sqrt{M_{f(x,z)}^2 + M_{f(y,z)}^2 + M_{t(z)}^2}\right)^{\frac{1}{3}} \tag{86}$$

Where R_m is the static breakage stress for the selected material. Given that the gear and the shaft are usually machined as a unique component, we'll assume $D_{shaft} = \max(D(z))$, while the diameter of the supports can be defined as the maximum value between $D(z = 0)$ and $D(z = H)$. A fillet radius is hence defined as a fraction of the difference between the shaft and the supports diameters.

A two steps verification is hence performed. At first, the verification against static breakage is provided through the application of the Tresca criterion and a safety coefficient for the static case computed as follows.

$$\mathrm{SF}_{st} = \frac{R_{p0.2}}{\max\limits_{z:0\to H}\left(\sqrt{\sigma_f^2 + 4\tau_t^2}\right)} \tag{87}$$

Where $R_{p0.2}$ is the material yield stress while σ_f and τ_t are respectively the maximum normal and tangential stresses calculated as

$$\begin{cases} \sigma_f = K_{t,f}\dfrac{\sqrt{\left(M_{f(x,z)}^2 + M_{f(y,z)}^2\right)}}{W_f} \\[3mm] \tau_t = K_{t,t}\dfrac{M_{t(z)}}{W_t} \end{cases} \tag{88}$$

With W_f and W_t being the bending and the torsional resistance modules, while $K_{t,f}$ and $K_{t,t}$ are the stress concentration factors dependent on the shaft geometry and derived by the curves provided by (Budynas & Nisbett, 2016). If the static safety factor is higher than a predefined value, the fatigue verification is performed, otherwise the diameter of the critical section is increased and the procedure repeated.

\

Since a load spectrum is available thanks to the dynamic model, cycles of normal and tangential stresses can be counted applying the rain flow method by (Matuishi & Endo, 1968). In particular, the top-level-up version mathematically illustrated by (Rychlik, 1987) has been applied in this work. According to Sines' hypothesis, we can evaluate the equivalent stress for a shaft subjected to fatigue as:

$$\begin{cases} \sigma_{eq,m} = \sigma_m \\ \sigma_{eq,a} = \sqrt{\sigma_a{}^2 + 3\tau_a{}^2} \end{cases} \tag{89}$$

Where the *m* and *a* subscripts are addressing the medium and alternate component of each considered stress type. If no rain flow counting method is applied, we may consider in first approximation:

$$\begin{cases} \sigma_m \approx 0 \\ \sigma_a \approx \max_{z:0 \to H} \left(\dfrac{\sqrt{\left(M_{f(x,z)}{}^2 + M_{f(y,z)}{}^2\right)}}{W_f} \right) \\ \tau_a \approx \dfrac{\max\limits_{z:0 \to H}\left(M_{t(z)}\right) - \min\limits_{z:0 \to H}\left(M_{t(z)}\right)}{2W_t} \end{cases} \tag{90}$$

The admissible alternate fatigue for the component may be computed as for y (Budynas & Nisbett, 2016),

$$\sigma_C(z) = C_L C_S C_F \frac{\sigma_{D-1}}{K_f} \tag{91}$$

Where σ_{D-1} is the fatigue limit for the material, C_L, C_S and C_F are coefficients dependent on the geometry and K_f is the stress intensity factor, each obtained by the tabulated value reported by y (Budynas & Nisbett, 2016). Safety coefficient for fatigue SF_f can hence be evaluated through the application of a properly settled Haigh diagram. The predicted fatigue behaviour of the shaft may be considered acceptable if $SF_f \geq 3$.

5.7 Supports sizing

The driving shaft of a generic gerotor pump is usually supported by two plain shaft bearings; for the lubrication of aeronautic engines, they are commonly made

of bronze because of the high temperature environment. The size of these supports depends mainly on:

- Maximum contact pressure (on the supports)
- Maximum linear relative speed between shaft and support
- Maximum value of the pv product
- Expected wear

The maximum contact pressure in a cylindrical support of axial length L_b can be computed as:

$$p_{max} = 4 \frac{R_A}{\pi D L_b} \tag{92}$$

Where R_A is the resultant of the reaction forces. The maximum value of the linear relative speed between shaft and bearing can be easily computed as:

$$v_{max} = \omega_{ref} \frac{D}{2} \tag{93}$$

While the product is the obvious combination of Equations (92) and (93). The expected depth of the worn material in the bearing at time t can be computed by modifying the (Archard, 1953) wear model with the experimental coefficients f_1 and f_1 depending on the motion type (complete rotations, oscillations etc.) and on the operating conditions, which values can be taken from manufacturers tables y (Budynas & Nisbett, 2016).

$$h_{worn} = f_1 f_2 K_w p_{max} v_{max} t \tag{94}$$

K_w is the wear factor, dependent on the bearing's material. The sizing process makes use of the supports diameters determined in Section 5.6 and of a first approximation length $0.5 \leq L_b/D \leq 2$. It hence computes the sizing parameters and the length t of the operative life associated with a maximum acceptable wear h_{worn}. If one or more design requirements are not met, the length is extended and/or the material changed. A similar approach can be used for the cam hosting the outer rotor.

5.8 Performance indexes evaluation

We introduce here a few indexes commonly used to evaluate the pump performances and distinguish between several solutions providing the same net

\

average flow-rate. The first performance index is the *flow-rate irregularity* ε, defined as:

$$\varepsilon = \frac{Q_{max} - Q_{min}}{Q_m} \% \tag{95}$$

Where Q_{max}, Q_{min} and Q_m are respectively the maximum, minimum and average flow rate generated by the pump at the reference speed. Its value depends on the driving shaft speed, the rotors' profiles geometry, the fluid property and the considered operating conditions.

Another important performance index is related to the expected wear rate for the rotors' profiles. According to (Kwon, Kim, & Shin, 2008), it is possible to rank the profiles wear behavior using the Wear Rate Proportional Factor (WRPF), which is defined as,

$$\text{WRPF} = \frac{\sigma_i v_s}{\omega_{in}} \tag{96}$$

Where σ_i is the contact stress, v_s the relative speed between the two rotors in the contact point and ω_{in} the reference speed of the inner gear. Fixing the driving shaft speed and the pressure drop across the pump, the WRPF index ends up to depend on the profiles geometry alone; the relative speed between the gears profiles in the contact points can be computed as follows.

$$v_s = (\omega_{in} - \omega_{ext})\overline{P_0 k} = \omega_{in}\frac{\tau_{ie} - 1}{\tau_{ie}}\overline{P_0 k} \tag{97}$$

Where $\overline{P_0 K}$ is the distance of the contact point K from the instantaneous center of rotation of the relative motion P_0.

Chapter 6

Automatic design framework

6.1 Introduction

In Chapters 4 and 5 we presented the theoretical framework needed to describe the geometry and the behavior of a generic gerotor pump. The equations needed to properly design the suction and delivery ports have been provided, as well as some preliminary considerations regarding the shaft sizing and the plain bearings choice. Finally, an algorithm to estimate the contact forces and stresses during the meshing process has been presented and a few performance indexes introduced. To investigate the properties of the profiles geometry and propose novel solutions for the radial ports case, the theoretical framework has been translated into a unified, comprehensive design and simulation tool provided in Matlab/Simulink$^{©}$.

This tool, here and after addressed as the "Automatic Design and Simulation Framework" (ADSF), has been prepared so that it might be able to:

- Automatically design valid gerotor profiles given the proper set of input parameters
- Automatically design and validate the geometry of the suction and delivery ports in both radial and axial configurations
- Automatically simulate the pump's behavior in nominal and (eventually) off-nominal conditions
- Automatically estimate the contact pressures during meshing, evaluate the performance indexes and signal anomalies
- Automatically perform a first tentative sizing of the driving shaft and of its supports

\

Moreover, the ADSF code and structure have been prepared following a modular approach, so that it might be easily interfaced with additional routines dedicated, in example, to the definition of the pump operative envelope or to the profiles optimization.

6.2 Features and organization

The user-interface of the automatic design and simulation framework is depicted in Fig. 38 and is roughly divided in two main section; on the right the dynamic model prepared in Simulink$^©$, on the left the commands window which is used to insert the input data to the pump sizing and/or simulation, launch several routines and interface the dynamic model with 4500+ code lines dedicated to data handle and results analysis. The routines that can be run through the command window can be divided in two main categories:

- Design routines: profiles design, pump simulation, data analysis
- Additional routines: estimate of performances in degraded conditions, operative envelope determination, debris behavior, profiles optimization

In this section we will focus on the design routines, highlighting their structure, needed inputs and provided outputs.
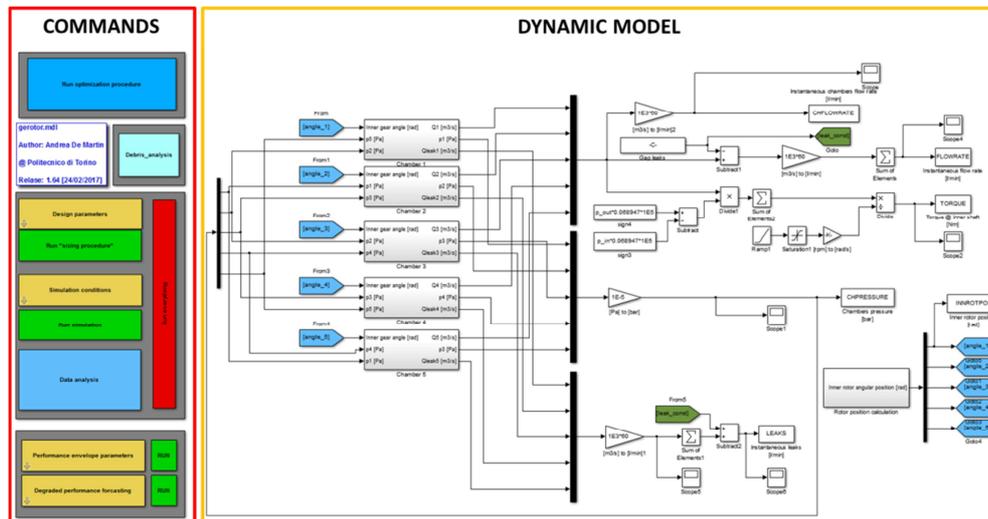
Figure 38: Automatic design and simulation framework interface

6.2.1 Pump design routine

The pump design routine is mandatory executed before every other, as its objective is to provide the complete definition of the geometry of the rotors and of the ports. The input mask of this routine is reported in Fig. 39. It allows to select the profile type for the external lobe and request the following input parameters:

- λ parameter
- Rotors eccentricity
- Requested flow rate or info on the axial length

In the rated environmental conditions tab the values for the reference temperature can be inserted as well as the rated suction and delivery pressure. The sizing constraint tab lets define the reference speed for the driving shaft and the safety coefficient against cavitation inception. The other tabs allow to define further parameters necessary to properly define alternative geometries.

This routines follows a simple cascade flow-chart. At first a few preliminary operations, such as input data reading and requested profile type recognition, are performed. Hence the external rotor is defined through the following steps: determination of the maximum diameter avoiding cavitation, lobe geometry definition and profile design. The inner rotor is then obtained through an iterative procedure employing the method described in Chapter 4 and its geometrical validity checked while searching for undercutting conditions.
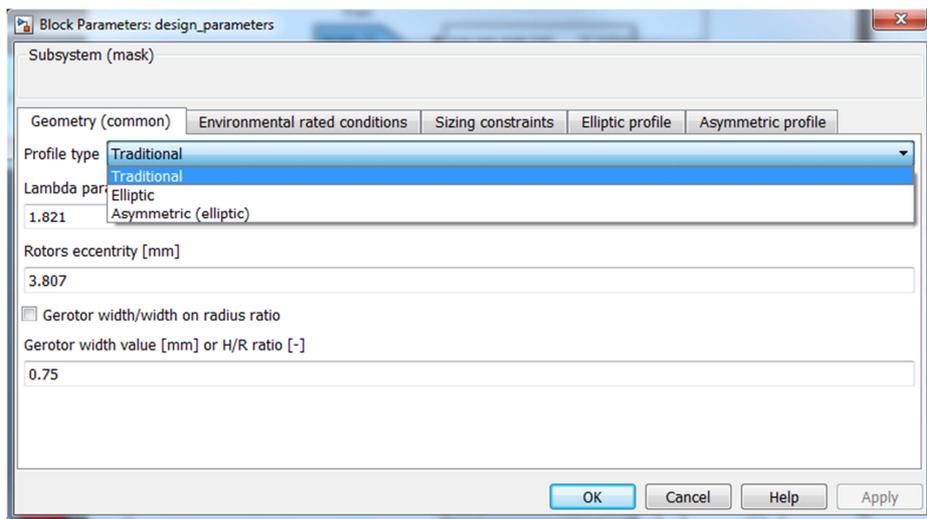
Figure 39: Input mask for the pump design routine

\

Another function impose several small rotation to both gears up to complete one complete revolution of the outer rotor and keeps track of the evolution of the contact points position. For each rotation, it isolate one of the *N* variable volume chamber, register its position and numerically integrate its frontal area, providing in the end the complete evolution of the chambers' volume along one pumping cycle and evaluating the pump's capacity. Moreover, it computes the expected theoretical flow rate by differentiating the chambers' volume over the inner rotor position as shown by Equation (98).

$$Q_{th} = \omega_{ref} \sum_{i=1}^{N} -\frac{\Delta V_{ch,i}}{\Delta \Phi_{in}}\bigg|_{\Phi_i \geq \pi} \tag{98}$$

The routine hence determine the ports areas needed to avoid cavitation and pressurization and compare them with the available space, finally providing a positive flag or an error code. Finally, the routine export the rotors profile in a .mat file that can be directly imported in the most common CAD software.

6.2.2 Pump simulation routine

The simulation routine employs the output of the design routine to perform the dynamic simulation of the pump in nominal or off-nominal conditions. In particular, the variable volume chambers evolution with respect to the angular position of the inner rotor and the ports' area are directly imported in the simulation environment.
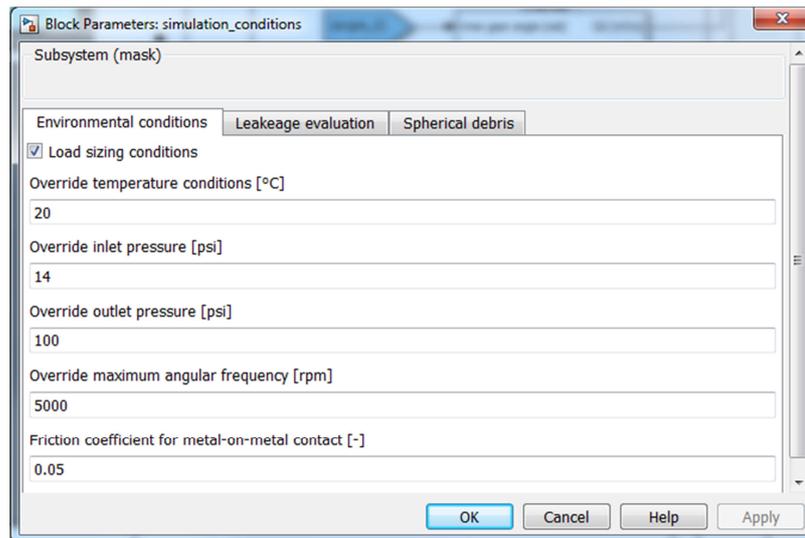
Figure 40: Input mask for the pump simulation routine

The input mask for this routine is reported in Fig. 40; the environmental and operating conditions used for the pump design are imported by default but it is possible to override each parameter to study the device expected behavior under off-nominal conditions. The leakage evaluation tab let the user define the size of the gaps between adjacent chambers and the dimensions of the passage between the external rotor and the cam, while the spherical debris tab will be further described in Chapter 7.

The pump model accepts as inputs the suction and the delivery pressures, the driving shaft speed and the fluid properties, while providing as output the chambers pressures, the total flow rate and the flow rate generated by each chamber, the total leakages and the net resistant torque. Please notice that this configuration allows the model to be easily connected with standard models of electric motors and hydraulic circuits, as shown in Fig. 41. This flexibility would allow to further expand the scope of this framework, allowing to simulate the designed pump inside more complex systems.

If not demanded otherwise, the simulation is performed on a 0.5 s time span; during the first 0.3 s the speed of the driving shaft is progressively increased and is hence kept constant for the final 0.2 s, with the integrator set to work over fixed steps of 1E-6 s. The ADSF proceed hence to down-sample the simulation results, organizing them in structure variables and saving them as .mat files ready to be processed by the data analysis routine.
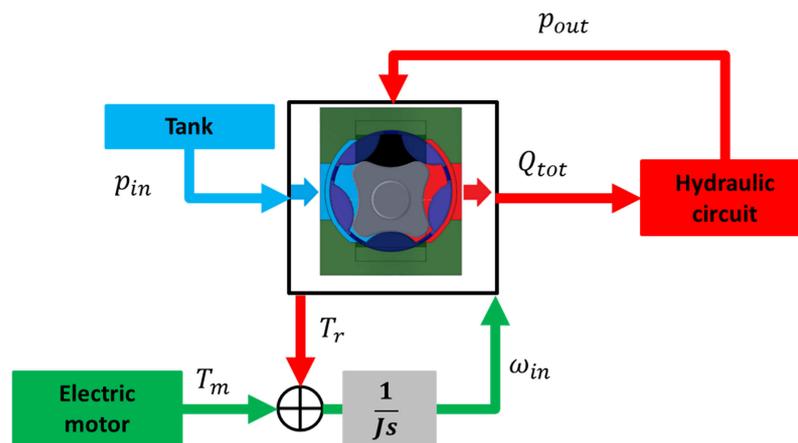
Figure 41: Interfacing the pump model with other components

\

6.2.3 Data analysis routine

The data analysis is by far the most complex of the three design routines and is strictly connected with both the profile definition and the pump simulation. The data analysis routine combine the information gathered through the simulation with the knowledge of the gears profiles to:

- Evaluate the contact forces during the meshing process
- Estimate the contact stress behavior of each contact point
- Compute the flow rate irregularity index
- Compute the specific slip and the relative speed between the rotors
- Evaluate the local and average WRPF
- Estimate the rotors mass
- Design the driving shaft and the shaft's bearings

At first, simulation results are further elaborated to translate the data function of the simulation time in signals function of the angular position of the inner rotor. For each registered position, a first algorithm search for the contact points, labelling each contact point's position found. Hence, as per Chapter 6, the contact forces and the contact stresses on each contact point are estimated and plotted.

The flow rate irregularity is computed based on the down-sampled data to avoid spikes that may occur due to issues in the integrator, while the equations provided in Chapter 5 are employed to evaluate the WRPF index on each contact point. The rotors' mass is estimated as follows.

$$m = \left(\pi R_{ext}^2 H - \frac{\Delta}{N-1} \right) \rho_{rot} \qquad (99)$$

Where ρ_{rot} is the density employed material.

To design the shaft and the shaft bearings, a vector containing several point on the axial length of the pump is generated. Hence, equations from Chapter 5 are applied to this vector, for each angular position of the shaft. In this way, the most stressful section can be easily identified, helping the design process.

6.3 Design routines performances

To address the framework performances we performed over 100 sizing procedures while keeping track of the computational time and size of the exported .mat files. The test has been performed over a desktop pc equipped with an *Intel 7-4770* CPU running at 3.40 GHz and with a DDR3 RAM.

The results for each design routine have been reported in Table 2. It is shown that the framework is able to completely define a novel gerotor pump in slightly less than 30 minutes. This statistics takes into account only valid geometries, since the algorithm stops otherwise after one of the design checks (hence after less than 5 minutes). As shown in Fig. 42, the most expensive routine from a computational time standpoint is the pump simulation, that lasts for more than the 40% of the overall design time considering the average conditions.

The shaft design features instead the widest distribution, due to the highly variable number of iterations required to identify the fatigue cycles and to converge to an acceptable size of its diameter.

Table 2: Computing performances of design routines

Routine		Computational time [s]		
		Min	**Average**	**Max**
Profile design	Rotors	261.34	273.67	291.24
	Ports	0.054	0.068	0.072
Pump simulation	Data handling	0.221	0.253	0.264
	Simulation	538.24	540.16	541.16
Data analysis	Data handling	8.432	9.954	11.024
	Contacts analysis	401.22	404.98	410.68
	Shaft design	41.23	58.17	96.38
TOTAL		1250	1287	1350

\
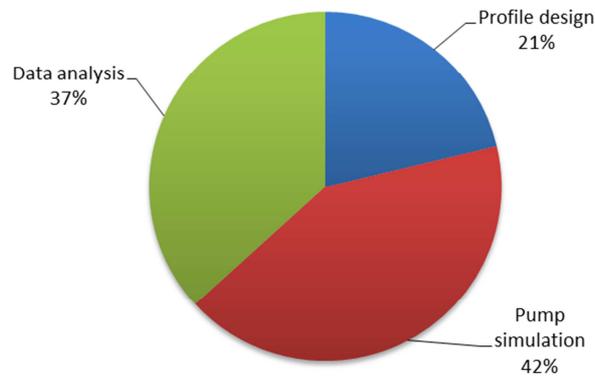
Figure 42: Breakdown of the ADSF computational effort

6.4 Additional routines

With additional routines we address all those ADSF's functions which are not responsible for the design of a single gerotor pump. These routines are:

- Definition of the operative envelope
- Estimation of pump performances in degraded conditions
- Simulation of the behavior of big metallic particles
- Profiles optimization

This section is dedicated to the first two, while the other will be object of further chapters of this thesis.

6.4.1 Performance envelope determination

To define the operating envelope of the pump means to evaluate its performances under off-nominal conditions and to match them with the project requirements.

The performance envelope routines allows to cycle the simulation and data analysis tools while defining the boundaries of the considered operating conditions. It is possible to vary the fluid temperature, the minimum and maximum pressures for both the suction and the delivery environments, the minimum and maximum speed for the driving shaft and the case study number.

6.4.2 Pump performances in degraded conditions

During the pump design process, the gerotor behavior is simulated under rated conditions to obtain data related to its nominal performances and to the contact

pressures and reaction forces needed to check the structural integrity of its components. As stated in the introduction, lubricating pumps are often subjected to high requirements on their operative life that translates in the need to keep high performances even after prolonged use. From this perspective, the most troublesome issue affecting gerotor pumps is the rotors profiles due to continuous relative motion under the effect of the fluid pressure. This would lead to wear or pitting of the gears profiles; since georots are unable to compensate for wear, this would cause issues in the meshing process and the increase of the leakages, that may become unacceptable for certain operating conditions. The "degraded conditions" routine allows to estimate the effect of the wear progression over the pump leakages and simulate the pump's behavior at different time stamps of its operating life.

Prediction of wear behavior is a rather complex subject; according to (Meng & Ludema, 1995) over 200 wear models could be found in literature, covering the influence of a wide array of materials properties and operating conditions and this number is moreover increased since. However, despite the huge research effort there is still no reliable way to predict wear progression (Williams, 1999). The authors hence chose to employ the and most common and simple wear model, that is the Archard/Rabinowicz equation by (Archard, 1953) and (Rabinowicz, 1965). Following this theory, the wear rate w is directly proportional to the normal load on the contact point $F_{c,i}$ and to the sliding distance s, while it is inversely proportional to the material hardness H_h.

$$w = K \frac{F_{c,i}s}{H_h} \tag{100}$$

Where K is the wear dimensionless constant. The contact force is computed by the data analysis routine described in Chapter 6.2.3, while the sliding distance can be obtained by integrating in time the value of the relative speed between the rotors profile. Considering a first simplifying hypothesis of uniform wear distribution, the detached material thickness Δh_w can be found as follows.

$$\Delta h_w = \frac{1}{Hs} \int_0^t K \frac{F_{c,i}s}{H_h} dt \tag{101}$$

The height of the gap associated with clearances in the gerotor pump depends, other than on the wear progression, on the materials' temperature. Focusing on the gaps between internal and external rotor profile, the overall height variation due to

\

thermal expansions in the direction normal to the contact zone Δh_T can be written as the sum of the thermal displacements of the inner and outer rotors:

$$\Delta h_T = \Delta y_{T,i} + \Delta y_{T,e} \tag{102}$$

Considering isotropic materials, thermal expansion in the direction of interest can be assumed in first approximation proportional to the temperature variation *ΔT*:

$$\Delta h_T = -\alpha_{m,i} r_{lim,in} \Delta T + \alpha_{m,e} r_{lim,ext} \Delta T \tag{103}$$

Where $\alpha_{m,i}$ and $\alpha_{m,e}$ are the linear thermal expansion coefficients of the internal and the external gears. The final expression of the clearance dimension h_g at the time *t* and temperature *T* between pump rotors can be hence estimated as:

$$h_g(t,T) = h(t = t_0, T = T_0) + \Delta h_w(t) + \Delta h_T(\Delta T = T - T_0) \tag{104}$$

A similar equation can be found for the clearance between the external rotor and the stator. Defining the set of temperature and operating time to be investigated, this routine simulate and analyze the pump's performance loss. An example of the possible results is reported in Fig. 43, for a case study gerotor pump driven at a constant speed of 5000 rpm for fluid temperatures ranging between -40°C and 100°C; the test fluid is the lubricating oil MIL-L-23699, which properties can be easily found in technical literature provided by oil makers, while pump rotors are in stainless steel. The wear constant is supposed to remain the same for the whole duration of the pump's operative life. As expected, performance degradation due to leakage increase tends to occur earlier at high temperature due to the effects of the fluid viscosity change.
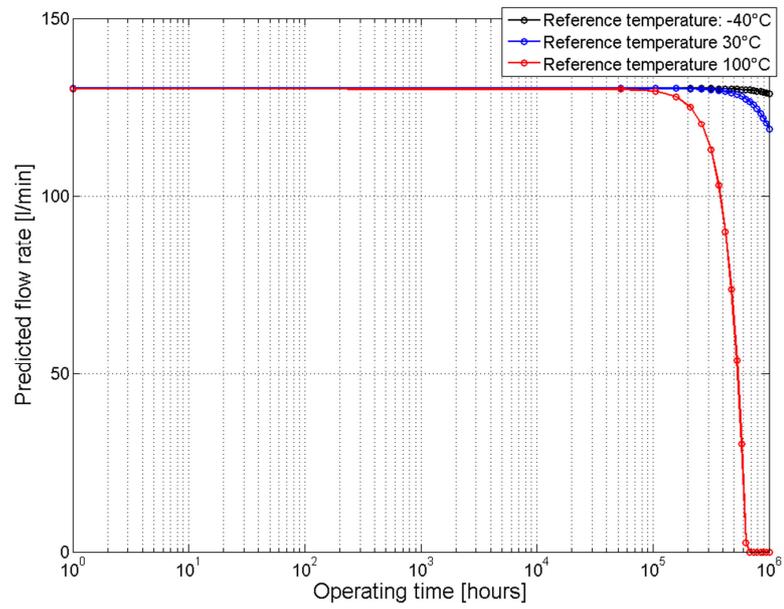
Figure 43: Example of performance loss due to increased leakages

\

Chapter 7

Survey on debris sensitivity

7.1 Survey rationale

Low-pressure pumps employed in lubricating systems may have to face the effects of the presence of big metallic particulate inside the fluid they are moving. In particular, in aeronautic engine this may occur during cold starts or in configurations that do not make use of a filter on the suction line.

While smaller debris raise the issue of faster abrasive wear, debris which size is comparable to that of the variable volume chambers may remain stuck inside the chambers, eventually causing jamming issues. As such, the pump should be able to expel the particle before it becomes troublesome, that is before that the available space inside the chamber falls below the particle dimensions. This capability is influenced by two main factors; the pump type and the configuration of the suction/delivery ports. In this Chapter we focus on the gerotor pumps and highlight the behavior of radial and axial ports configurations. The dedicated routine within the ADSF is presented and its results discussed.

7.2 Additions to the simulation model

To perform this survey some additions to the simulation model need to be introduced. In particular, the effect of the debris presence and its behavior given the rotors geometry and the system dynamics must be provided.

In this section we describe the dynamic model used to estimate the behavior of a spherical debris for both radial and axial ports configuration under some simplifying hypothesis.

7.2.1 Debris expulsion model – radial ports configuration

The dynamic equilibrium of the spherical debris can be described by making reference to Fig. 44. Addressing with r the module of the distance between the debris center and the origin of the fixed reference frame, we may write the following equation.

$$[p_{ch}(r - r_{db}) - p_{ch}(r + r_{db})]A_{db} + m_{db}r\omega^2 - c(\dot{r} - v_f) = m_{db}\ddot{r} \qquad (105)$$

Where $p_{ch}(r + r_{db})$ and $p_{ch}(r - r_{db})$ are the chamber's pressures at the distances $(r + r_{db})$ and $(r - r_{db})$, A_{db} is the effective area for the debris, m_{db} its mass and ω its angular frequency. c and v_f are respectively the viscous friction coefficient and the fluid velocity.

The following simplifying hypothesis are introduced:

- Flow forces are neglected
- Debris angular frequency is equal to that of the outer rotor
- Chamber's pressure varies with the second power of the fluid velocity
- The debris simply translates along the radial direction (no rotations around its own center)

The debris presence tends moreover to change the discharge coefficient in the port zone as described by the (Idelchik, 2005) tables while decreasing the effective size of the port area.
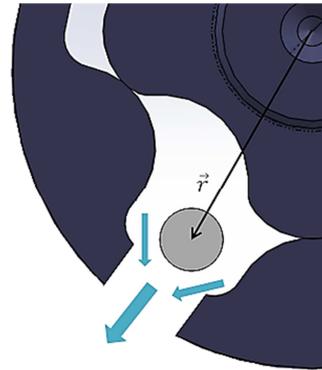
Figure 44: Spherical debris – radial ports

\

7.2.2 Debris expulsion model – axial configuration

For the axial port configuration, the dynamic equilibrium of the debris particle in its motion across the pump is written along the gerotor's axial direction. Addressing with r the distance of the particle from the suction side along the axial direction as shown in Fig. 45, we may hence write:

$$[p_{ch}(r - r_{db}) - p_{ch}(r + r_{db})]A_{db} - c(\dot{r} - v_f) = m_{db}\ddot{r} \qquad (106)$$

Comparing this expression with the radial ports configuration, we may notice a first significant difference in the loss of the term due to the centripetal acceleration $r\omega^2$.
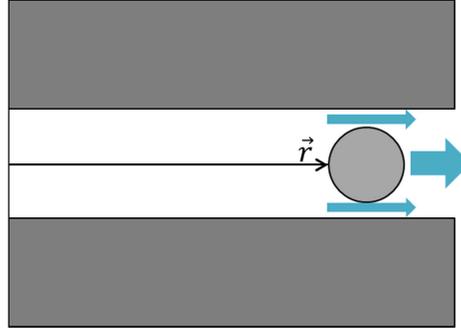
Figure 45: Spherical debris – axial ports

7.2.3 Additional routine in the automatic framework

An additional routine is prepared within the ADSF to run the simulations and elaborate their results. It is given the freedom to set the size and the material of the spherical particle, while importing or changing the operating conditions defined during the pump design phase.

In the Matlab/Simulink$^{©}$ environment, the debris dynamic is inserted as a conditional block, which is activated only during the delivery phase. In order to study the worst possible conditions, the initial state is always associated with the farthest possible point from the delivery port. The block produce as outputs the breakdown of the forces applied to the debris particle and an index F_{db}, equal to:

$$\begin{cases} F_{db} = 1 & r > r_{max} \\ F_{db} = 0 & r_0 \leq r \leq r_{max} \wedge A_{db} < \min(A_{ch}, A_{port}) \\ F_{db} = -1 & r_0 \leq r \leq r_{max} \wedge A_{db} \geq \min(A_{ch}, A_{port}) \end{cases} \qquad (107)$$

The value of the debris index is hence equal to 1 when the particle has been expelled, 0 if the particle is still inside the pump but still has the possibility to leave the chamber and -1 when the debris remains trapped. The addition of the debris model increases the computational effort required during the simulation, raising the average computational time on the same machine up to 634.34 s.

7.3 Results

The simulations have been performed considering a reference geometry that remains the same in both radial and axial ports configurations, to assess which is the maximum size of the spherical debris to be expelled from the pump.

The analysis has been repeated for different angular speed of the driving shaft, leading to the results reported in Fig. 46; here the maximum size of the debris able to leave the chamber is reported as a ratio over the maximum diameter of the sphere that may be inserted inside the pump's chambers. As it can be seen, the radial ports configuration appears to be favorable, being able to expel particles of bigger size. This behavior is mainly related to the influence of the centripetal acceleration of the debris and the shorter distance to cover in order to leave the pump.
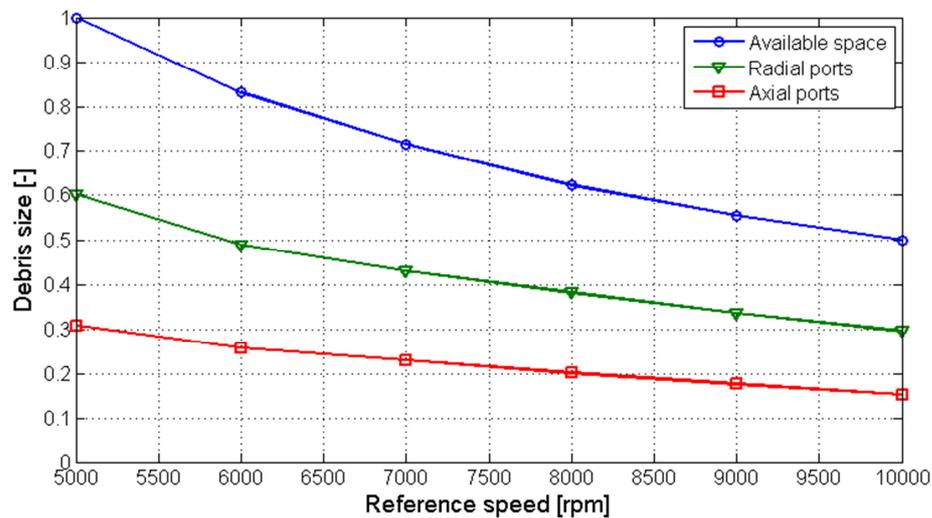
Figure 46: Maximum size of the expelled particles

\

Chapter 8

Introduction to asymmetric lobes profiles

8.1 Introduction

As highlighted in the last chapters, the geometry of rotors profiles provides a fundamental contribute to the determination of the pump's performances. Although several studies are available in literature, as per Chapter 1, none consider the radial ports configuration. A first study is hence carried out to investigate the effects related to variations in the geometry of the outer gear lobes. All the results reported in this chapter have been obtained considering a suction port pressure of 14 psi and an delivery port pressure equal to 140 psi; the reference speed of the driving shaft spans within the 4000 rpm and 10000 rpm range, that is the usual target for lubrication systems in mobile applications. For each reference speed, gerotor with different geometries have been sized and for each profile type the maximum displacement conditions have been assessed following the procedure described by the flowchart reported in Fig. 47.

Given the operating conditions, the ASDF defines a first tentative value of the eccentricity e, of the λ parameter and of any other geometrical quantity that contributes to the definition of the gears profiles. Hence, the simulated flow rate under nominal condition for the newly designed profile is computed: if its value is higher than the previously registered maximum one for the same profile type and the same reference speed, it is saved as the new reference value along with the other indexes. A new set of sizing parameters is in any case created and the process iterated.
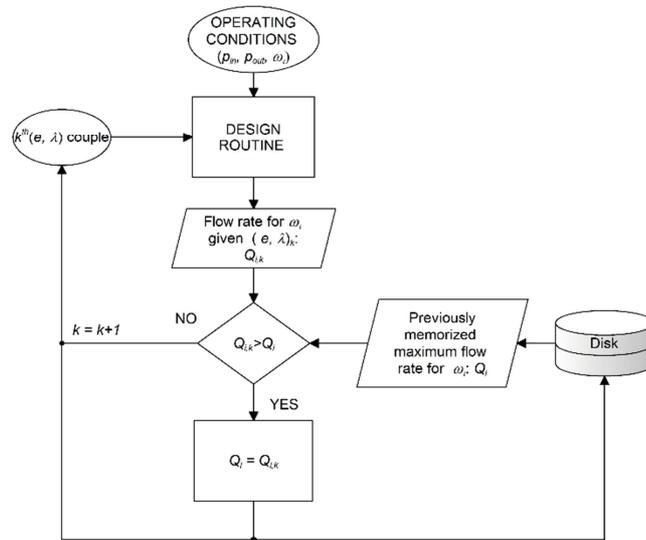
Figure 47: Routine to assess the maximum pump capacity conditions

8.2 Influence of the teeth number

The first needed step is to study the influence of the teeth number over the flow-rate performances of the pump. We hence apply the afore mentioned method to 5 and 7 teeth circular lobes gerotor and we report the results regarding the pumps' capacity and their flow irregularity in Fig. 48. In particular, it is evident that the maximum pump capacity tends to decrease for high teeth number. This is pretty was expected for the radial ports configuration; we demonstrated in Chapter 3.2 that the condition ensuring the complete filling of the pump's chambers translates into a condition over the external rotor profiles in the radial ports scenario. Hence increasing the teeth number would have the effect of reducing the space available between the lobes, finally limiting the fluid volume that can be actually moved by the pump.

Moreover, these results are coherent, even if different in values, with analysis available in literature for traditional axial ports gerotors (Karamooz Ravari, Forouzan, & Moosavi, 2012). It is theoretically possible to employ an even lower number of lobes to further increase the pump's capacity; however, both the extensive literature reported in Chapter 1 and the current industrial practice recommend to use at least five teeth for the external rotor in order to ensure a sufficiently regular meshing. On the downside, decreasing the teeth number significantly raise the flow-rate irregularity index. A high flow-rate irregularity may be unacceptable for the user, even if mitigated by the circuit capacity, and generate high torque ripples on the pump's driving shaft.

\

Given the target application demanding high flow-rates and low mass as a primary objective, we focus on the study of the five teeth case. In the next sections, the theoretical displacement, flow rate irregularity and WRPF factor will be computed and compared to determine advantages and disadvantages of each considered geometry. Please notice that many results have been normalized with respect to the value achievable for a circular lobe device working at 4000 rpm.
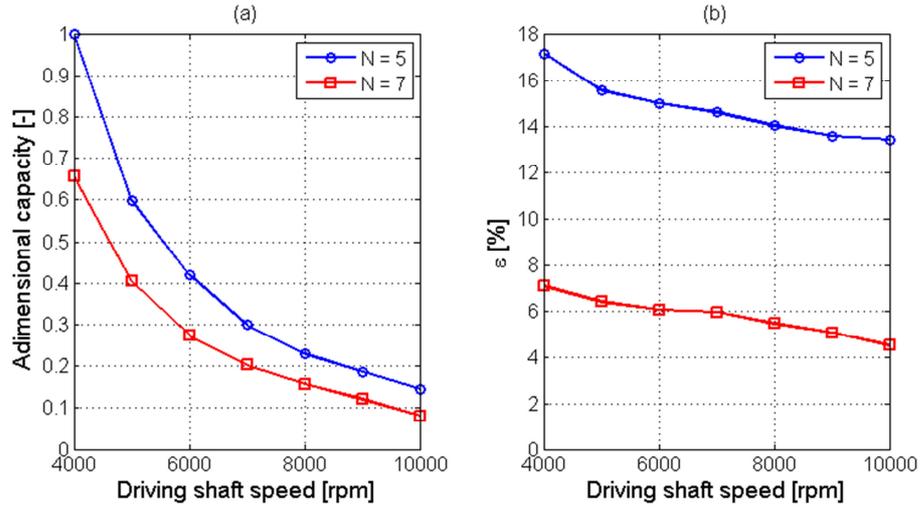
Figure 48: 5 vs 7 teeth gerotors: (a) displacement – (b) flow irregularity

8.3 Circular and elliptic lobes

After the teeth number, we focus on the rotors geometry. As extensively shown in the previous chapters, the definition of the traditional cycloidal profile is completely performed through the (λ, e) couple. Given the circular geometry of the lobes, the teeth height and the teeth width are strictly correlated, making it difficult to have high and narrow teeth. To add an optional degree of freedom in the profiles definition, we first pursue the use of elliptic lobes in the external rotor.

Recalling Equations (38) and (39), we may define their profile by using $k_{ell} \neq 1$.

$$\begin{cases} \chi = \rho_\chi cos(\xi) \\ \psi = k_{ell}\, \rho_\chi sin(\xi) \end{cases} \tag{108}$$

$$\begin{cases} tan(\vartheta) = k_{ell}\, tan(\xi) \\ \quad 0 \leq \xi \leq \pi \end{cases} \tag{109}$$

We hence focus on the study of the differences between the pumps performances using elliptic and circular profile. We identify two main types of

elliptic lobes, namely "narrow" teeth and "enlarged" lobes. Narrow teeth are those for which $k_{ell} > 1$; they allows to obtain additional space for the radial ports and are hence expected to provide higher flow rates. An example is provided in Fig. 49.

On the other hand, enlarged teeth are obtained for $k_{ell} < 1$, with an example provided in Fig. 50. Since the space between the external rotor teeth is reduced, a decrease in the maximum flow rate is expected. At the same time, the increased teeth size should allow for a more regular meshing and a reduction in the profiles wear may be expected.

The comparison analysis has been carried out searching for the maximum flow rate conditions for each of the three considered geometry (circular, narrow elliptic, enlarged elliptic); the k_{ell} parameter for the narrow elliptic case spans between *0.8* and *0.95*. For the enlarged option, it may instead vary within the *1.05- 1.20* range.
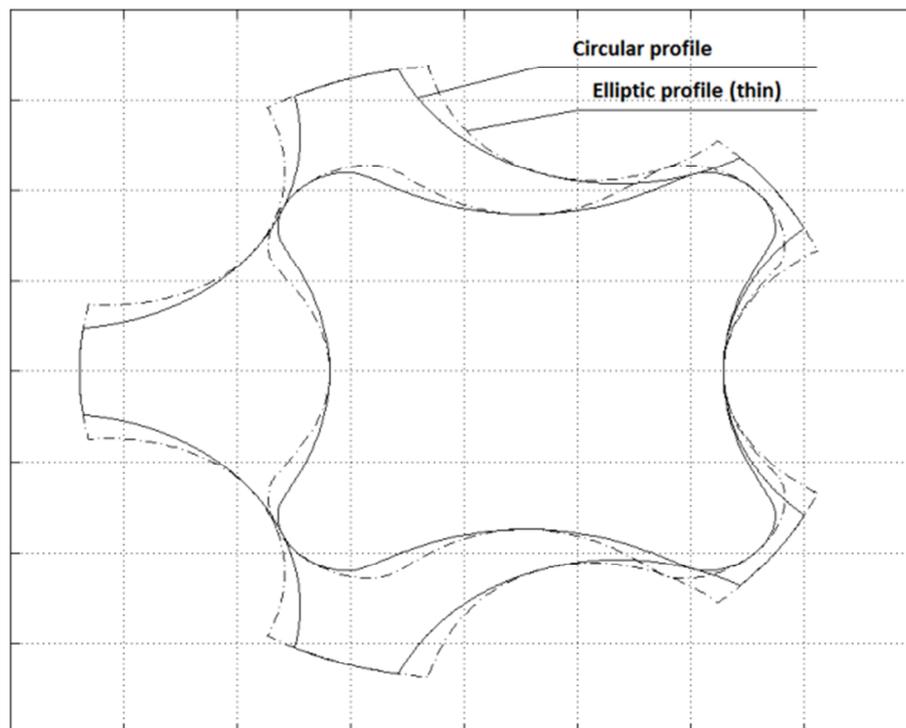
Figure 49: Circular and narrow lobes profiles
5000 rpm, $e = 5.0$ mm, $\lambda = 1.8$, $k_{ell} = 0.85$

\
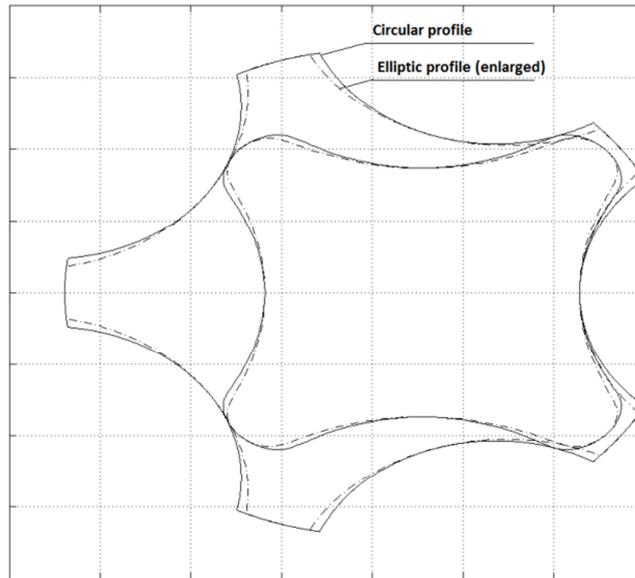
Figure 50: Circular and enlarged lobes profiles
5000 rpm, $e = 5.0$ mm, $\lambda = 1.8$, $k_{ell} = 1.05$

Results regarding the maximum displacement obtainable with each of the selected geometries over a 4000-10000 rpm span are reported in Fig. 51. As expected, the use of narrow teeth allows to obtain an appreciable increase in flow rates that, for the considered case, has an average value of 7.5 % circa. The opposite situation occurs when considering the enlarged teeth case. In this case, the reduced space for the radial ports origins an flow rate loss of the 9.03% for the considered case.
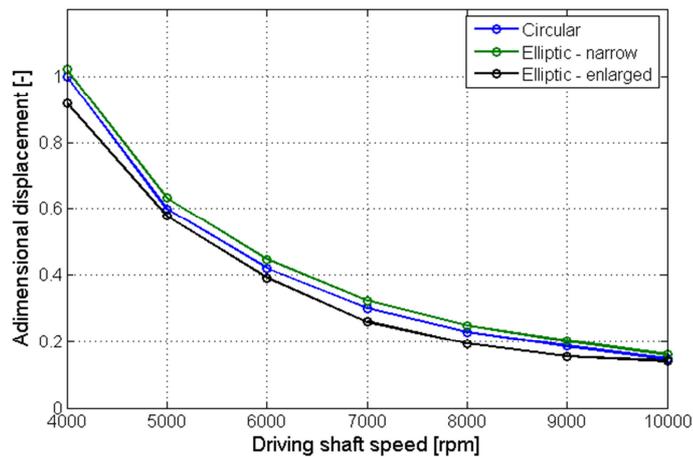
Figure 51: Maximum displacement for circular and elliptic profiles

Capacity increase however comes with some drawbacks regarding the flow rate irregularity index and the wear rate.

As shown in Fig. 52-(a), flow rate irregularity index is higher for narrow elliptic lobes, while the enlarged case generates a reduction of the same performance index. It has to be noticed that flow rate irregularity is rather high for the maximum flow rate configuration, being higher than 10% in most of the cases; this is mainly due to the low teeth number and could represent a major issue for applications requiring more stable flow rate or low noise levels. It is interesting to notice how a similar analysis by (Jung, Han, Cho, & Kim, 2009) for axial ports gerotors gave different results. Observing their results for gerotor with 5 teeth in the external lobes, flow rate maximization could be obtained with k_{ell} values ranging between *0.9* and *1.2* depending on the pump size and eccentricity. This difference is due to the fact that in the axial port solution the rotors profiles have negligible influence over the ports size, while the effects on radial inlet/outlet solution are significant. The study of the wear rate factor produces similar results: as reported in Fig. 52-(b), the use of narrow teeth tends to increase the WRPF parameter, here reported as its ratio on the value computed for the circular profile for a 4000 rpm reference speed; the contrary happens using enlarged lobes. This behaviour can be explained as the results of two main factors: the increased pump capacity (and hence resistant torque) in the narrow teeth case and the profiles curvature variations.
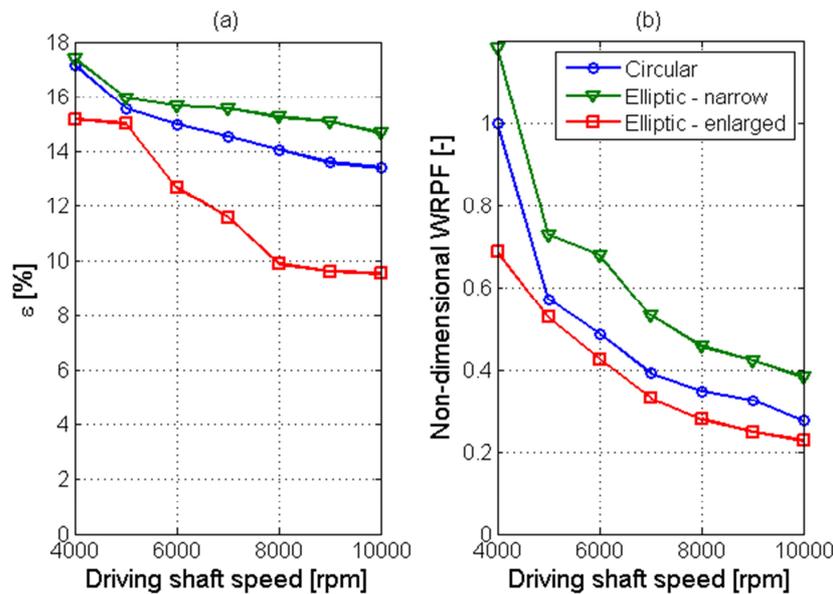
Figure 52: circular vs. elliptic lobes: (a) **ε** – (b) WRPF

\

The decreasing trend of the WRPF factor with the increase of driving shaft speed is common to each of the considered solution and is related to the progressive downsizing of the device and so of its displacement in order to avoid cavitation problems.

8.4 Asymmetric lobes

The use of narrow teeth looks promising in the perspective of maximizing the flow rate capability of the pump, but suffers from an evident increase of the wear rate. For applications aiming at obtaining good performance stability over time, this could represent a significant issue. In order to strike a good balance between the WRPF and the flow rate gain ensured by the narrow elliptic lobes, a possible solution would be the combination of both the narrow and the enlarged elliptic teeth profile, or of the narrow and circular lobes depending on the project requirements.

As such, we introduce the concept of asymmetric lobes for gerotor pumps. Asymmetric teeth are not infrequent in high-performance gearing systems; they offer several advantages on weight saving, torque density and structural integrity, but are only suitable to gears operating without changing the verse of rotation (Borwn, Davidson, Hanes, & Weires, 2010). Since this condition is verified for most of the mobile lubrication systems, they are suitable for gerotor pumps but not for pump-motor devices.

External gear lobes can be obtained using circular or large elliptic profile for the half tooth which is in contact with the inner gear during the fluid suction phase, while the space for the radial ports is ensured by the use of a narrow ellipse arc for the second half tooth. From a mathematical perspective, Equations (107) and (108) are still valid, taking into account that we have:

$$
\begin{cases}
k_{ell} = k_1 & 0 \leq \xi \leq \dfrac{\pi}{2} \\[2mm]
k_{ell} = k_2 & \dfrac{\pi}{2} < \xi \leq \pi
\end{cases}
\tag{110}
$$

In this way, the two ellipse arcs share one semi-axis (the one oriented along the radial direction of the pump); hence, the continuity of both the profile and of its first derivative is ensured by design.

Another adjustment to the ADSF is needed in the routine computing the space available between the adjacent teeth in the external rotor; in this case, it is computed as the average between the space that would be obtained by two complete elliptic profiles with $k_{ell} = k_1$ and $k_{ell} = k_2$.
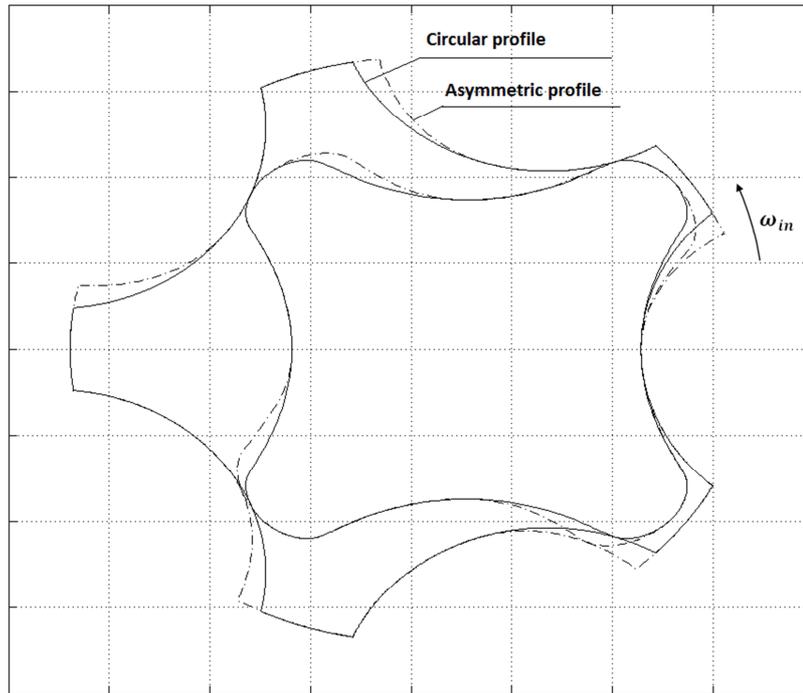
Figure 53: Circular and asymmetric lobe profiles
5000 rpm, $e = 5.0$ mm, $\lambda = 1.8$, $k_{ell,m} = 0.85$, $k_{ell,M} = 1$

An example, featuring half circular and half narrow elliptic teeth can be found in Fig. 53. In order to test the asymmetric teeth capabilities, the lobes have been slightly enlarged on their active side ($k_{ell} = 1.05$) and strongly narrowed on the non-active flanks ($k_{ell} = 0.85$). Please notice that this configuration is not the optimal one by any means and it has been selected just as a proof of the capabilities of the asymmetric lobe concept. Again the comparison has been performed while searching for the geometrical parameters generating the maximum displacement for the given suction pressure and driving shaft speed; results have been reported in Fig. 54. As shown in the graphs, it is possible to appreciate that the solution maximizing the flow-rate capability for the asymmetric teeth case is able to consistently reduce the WRPF from 5% to 15% with respect to the narrow lobe case, while some minor benefits can be observed for the theoretical flow rate irregularity index

The maximum displacement of the so-defined asymmetric case is in average inferior to that of the narrow case, giving up to the 2.5% of the narrow elliptic solution's capacity, while still remaining superior to the circular option. Please notice that those results may change based on the combination of the (k_1, k_1) couple.

\
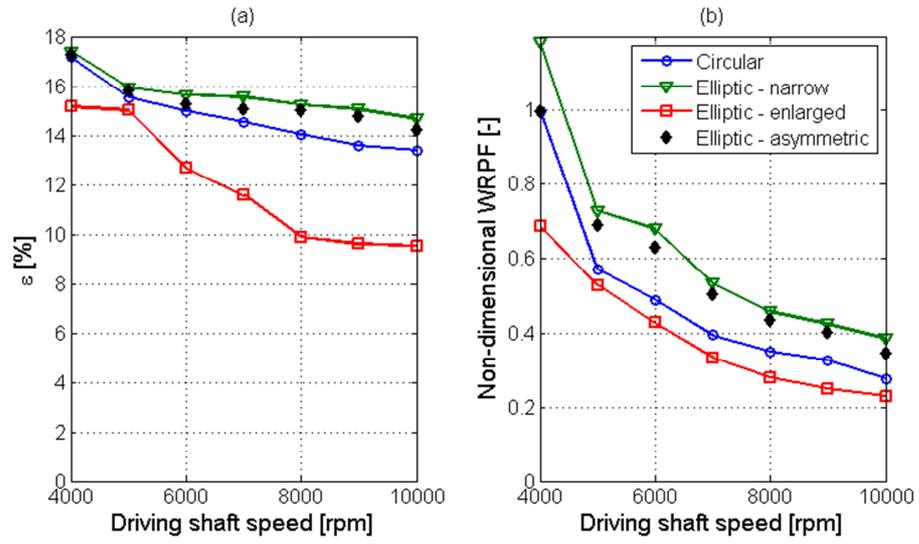
Figure 54: asymmetric lobe performances: (a) $\boldsymbol{\varepsilon}$ – (b) WRPF

Chapter 9

Asymmetric profiles optimization

9.1 Introduction

Having assessed the potentiality of the introduction of the asymmetric lobe design in gerotor pumps using radial-ports configuration, we focused on a different use of the same profile geometry. In particular, the interest shifted to study in a more rigorous way the impact that the asymmetric elliptic lobe design may have on a generic gerotor pump performances, regardless of the port technology adopted. Hence we focused on the possible effects over the flow irregularity, wear rate and rotors mass working with a fixed requirement for the pump's capacity.

Several single and multi-optimization cycles have been performed to assess the asymmetric lobe capability to optimize one single performance index or to find the best compromise between conflicting requirements.

9.2 Stochastic optimization methods for engineering

Optimization through stochastic algorithm has been widely used in the last decades to solve engineering problems whereas it is difficult to provide a-priori hypothesis of the region containing the optimum solution, or whereas the objective-function is not continue over its entire dominion (Alotto, et al., 1998). This class of algorithm in fact searches for the optimum applying a certain degree of randomness and only revolve around the evaluation of the objective function itself, without the need to compute the function's gradients. Stochastic methods mainly follows three alternative approaches; genetic algorithms (Rechenberg, 1994) and evolutionary strategies (Holland, 1992) mimic the evolutionary behaviour of nature, while simulated annealing imitate the behaviour of cooling

fluids (Metropolis, Rosenbluth, Teller, & Teller, 1955). Stochastic algorithms have been already applied to pump stacking optimization by (Kelner & Léonard, 2004) and specifically to gerotor profiles in works by (Jae-Hun, Chul, & Chang, 2006) and (Kwon, Kim, & Shin, Optimal rotor wear design in hypotrochoidal gear pump using genetic algorithm, 2011).

9.2.1 Single-objective optimization

Several declinations of the evolutionary strategy for single-objective optimization are available in literature (Alotto, et al., 1998), but they all share the same philosophy, based on the four base principles of the process of organic evolution: reproduction, mutation, competition and selection (Fogel, 1995). A flow-chart for the most general method, the $(\mu/\rho\,;\lambda)$ strategy, is reported in Fig. 55 (Schwefel, 1977).
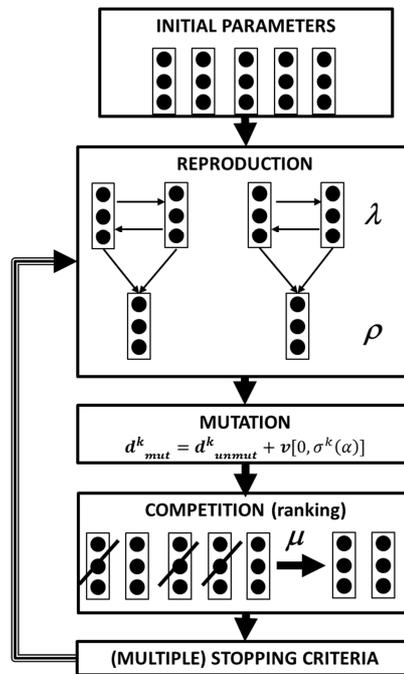
Figure 55: Flowchart for the $(\boldsymbol{\mu}/\boldsymbol{\rho}\,;\boldsymbol{\lambda})$ strategy

Starting from an initial populations, λ elements are chosen as parents, giving birth to r offsprings; the simplest method to perform this step is through arithmetical crossover, that is a linear combination of the vectors containing the optimization parameters of the parents (Janikow & Michalewicz, 1991). For a two parents-two scenario this can be translated as,

$$\begin{cases} \boldsymbol{d}^{k+1}_{unmut1} = \alpha\boldsymbol{d}^k_{p1} + (1-\alpha)\boldsymbol{d}^k_{p2} \\ \boldsymbol{d}^{k+1}_{unmut2} = \alpha\boldsymbol{d}^k_{p2} + (1-\alpha)\boldsymbol{d}^k_{p1} \end{cases} \tag{111}$$

Where $\boldsymbol{d}^{k+1}_{unmut1}$ and $\boldsymbol{d}^{k+1}_{unmut2}$ are the offspring parameter vector, $\boldsymbol{d}^k_{p1}$ and $\boldsymbol{d}^k_{p2}$ are the parents and α the crossover operator. The offspring are hence mutated by applying a random factor chosen from a standard distribution $\boldsymbol{v}$ centred in 0 with standard deviation $\sigma(\alpha)$ which is divided or multiplied by a factor α at the beginning of each iteration.

$$\boldsymbol{d}^{k+1}_{mut} = \boldsymbol{d}^{k+1}_{unmut} + \boldsymbol{v}[0,\boldsymbol{\sigma}(\alpha)] \tag{112}$$

The population, in this study comprehensive also of the parents, is hence ranked and the first μ elements selected, while the others are discarded. Multiple stopping criteria are finally inserted to put a stop to the optimization loop. In this paper four alternatives are considered: if one of them is met, the results exits the loop. The first one, is related to the algorithm convergence and computed through the quadratic norm of the population with respect to its mean value, as reported by (Back & Schwefel, 1993). The second criterion is the number of consecutive loops in which the variation of the optimization parameters remains under a certain threshold. This is due to the fact that each considered parameter is a geometrical quantity used to describe a physical object; as such, variations that remains below the geometrical tolerances of the possible production process are not useful. If this condition repeats itself on each parameter for more than three cycles, the algorithm stops the loop. The last condition, related to the computational time required, is the maximum number of iterations.

9.2.2 Multi-objective optimization

Evolutionary strategies can be extended to multi-objective optimization by slightly modifying the flowchart reported in Fig. 55 and by paying particular care to the competition step (Konak, Coit, & Smith, 2006). Between the methods available in literature, the simplest and most straight-forward approach is to reduce the multi-objective optimization to a scalar problem by defining the fitness function $f(\boldsymbol{d})$ as the weighted sum of the normalized objective functions $f_m(\boldsymbol{d})$ for each single objective. In these conditions, the objective function for the multi-objective problem becomes:

$$\min(f) = \sum_{m=1}^{n_o} w_m f_m(\boldsymbol{d}) \tag{113}$$

\

Where n_o is the number of the optimization objective considered by the algorithm. While being extremely simple to implement and evaluate, the final result is dependent on the weights value, that are difficult to properly set a-priori.

According to (Konak, Coit, & Smith, 2006), a good compromise between performance and implementation issues is represented by the Pareto ranking methods based on non-domination sorting, firstly proposed by (Goldberg, 1989), and then refined by (Srinivas & Deb, 1994) and (Deb, Agrawal, Pratap, & Meyarivan, 2000). This class of algorithms is based on the idea that the optimum solution is such that no other combination of the optimization parameters is able to provide better results in one of the objective functions without worsening at least one of the others; as such, they make use of a dominance rule and of a fitness sharing function to search for the true Pareto front. In this study, the fitness r of each possible solution to the optimization problem is defined using the Fonseca version (Fonseca & Fleming, 1993) of Goldberg criterion based on the number of dominating solutions:

$$r(\boldsymbol{d}_i, K) = 1 + nq(\boldsymbol{d}_i, K) \tag{114}$$

Where $nq(\boldsymbol{d}_i, K)$ is the number of solutions dominating $\boldsymbol{d}_i$ during the *K-th* generation.

One of the most significant difficulties in multi-objective optimization is to avoid the formation of clustered solutions, that causes the overrepresentation of parts of the variables space at the expense of the rest of the dominion and that may provide misleading results. To limit this issue, the fitness-sharing approach proposed by Fonseca and Fleming has been employed in this study. This method is based on the computation of the Euclidean distance D_K between every solution pair $(\boldsymbol{d}_i, \boldsymbol{d}_j)$ in the objective space normalized between 0 and 1 during the *K-th* iteration of the optimization algorithm:

$$D_K(\boldsymbol{d}_i, \boldsymbol{d}_j) = \sqrt{\sum_{m=1}^{n_o} \left(\frac{f_m^K(\boldsymbol{d}_i) - f_m^K(\boldsymbol{d}_j)}{\max_{k=1\ldots K} f_m - \min_{k=1\ldots K} f_m} \right)^2} \tag{115}$$

Hence, given those distances, the number of solutions falling inside a niche of size σ_{niche} may be calculated as,

$$nc(\boldsymbol{d}_i, K) = \sum_{\substack{j=1\ldots(\rho+\lambda) \\ r(\boldsymbol{d}_i)=r(\boldsymbol{d}_j)}} \max\left(\frac{\sigma_{niche} - D_K(\boldsymbol{d}_i, \boldsymbol{d}_j)}{\sigma_{niche}}, 0\right) \tag{116}$$

Finally the fitness $r(\boldsymbol{d}_i, K)$ of each solution for the *K-th* generation is adjusted as follows.

$$r'(\boldsymbol{d}_i, K) = r(\boldsymbol{d}_i, K)nc(\boldsymbol{d}_i, K) \tag{117}$$

In this way, the overall ranking of the clustered solutions in the minimization process is penalized, hence reducing the probability of being selected for breeding while enhancing the exploration of the optimization parameters space.

9.3 Profiles optimization

According to previews chapters, we can identify a few optimization parameters, that are meaningful geometrical quantities that determines the rotors shape and performance. The optimization process has been performed on gerotors having five teeth in the external gear, since this solution allows to obtain higher flow rate capability at a given reference speed. A generic optimization parameter vector $\boldsymbol{d}$ is hence defined as:

$$\boldsymbol{d} = \begin{bmatrix} \lambda \\ e \\ k_1 \\ k_2 \end{bmatrix} \tag{118}$$

Three indexes are used to evaluate the pump performance and perform the optimization procedure: the flow rate irregularity ε, the Wear Rate Proportional Factor (WRPF) and the estimated rotors mass *m*.

For each parameters vector the corresponding gerotor pump is designed and tested through the Automatic Design and Simulation Framework. The ASDF outputs are collected and used to perform the optimization cycles. The design routine of the ADSF is eventually resected if one or more geometrical constraints or performance requirements are not met.

9.3.1 Cycloidal profile optimization

The first step to assess the capabilities of the asymmetric profile is to define a proper set of reference values for each of the three optimization objectives. In

\

order to do so, three series of single-objective optimization cycles have been performed for the traditional epitrocoidal profiles.

The reference speed of the driving rotor has been varied between 5000 rpm and 10000 rpm to target a mobile application, while the pressure at the inlet port is approximately 1 bar. The required flow rate has been set to 100 l/min. For each reference speed, the pump geometry has been optimized with respect to each performance index, leading to the definition of three sets of gerotor profiles each able to minimize the flow irregularity, wear rate and rotors mass. The optimization parameters vector is obtained simplifying the one reported in Equation (117) by neglecting k_1 and k_2. Starting from these parameters, the algorithm designs and tests the gerotor through the automatic framework. The safety factor against cavitation is initially set to 1.

The number of parents in the evolutionary algorithm is set to $\lambda = 4$, while the offsprings are $\rho = 6$. The population size that survives after each optimization cycles is $\mu = 8$. In order to achieve faster convergence, parents are not discarded a-priori and take part in the ranking; as such, it is possible for them to survive for more than one optimization cycle. To monitor the algorithm behaviour, the ratio of successful mutation for the *k-th* optimization cycle has been computed as:

$$p_m^k = \frac{\left| D_\rho^k \cap D_\mu^k \right|}{\left| D_\mu^k \right|} \tag{119}$$

Where D_ρ and D_μ are respectively the sets of the mutated off-springs and of the population survived after the *k-th* cycle. The maximum number of iterations allowed to the algorithm is $N_{max} = 50$. An example of the algorithm behaviour is reported in Fig. 56, Where q_n is the quadratic norm of the population with respect to its mean value (Alotto, et al., 1998). The results of the optimization process are reported in Fig. 57. The wear rate and rotors mass tends to progressively decrease with the reference speed tending to reach a plateau towards the end of the investigated speed range. This can be explained by considering that the flow rate requirement remains the same for the whole speed range; as such the benefits of downsizing the gerotor radial dimension are progressively decreased by the increase in the pump length. For the same reason no appreciable variation of the optimum flow rate irregularity can be observed.
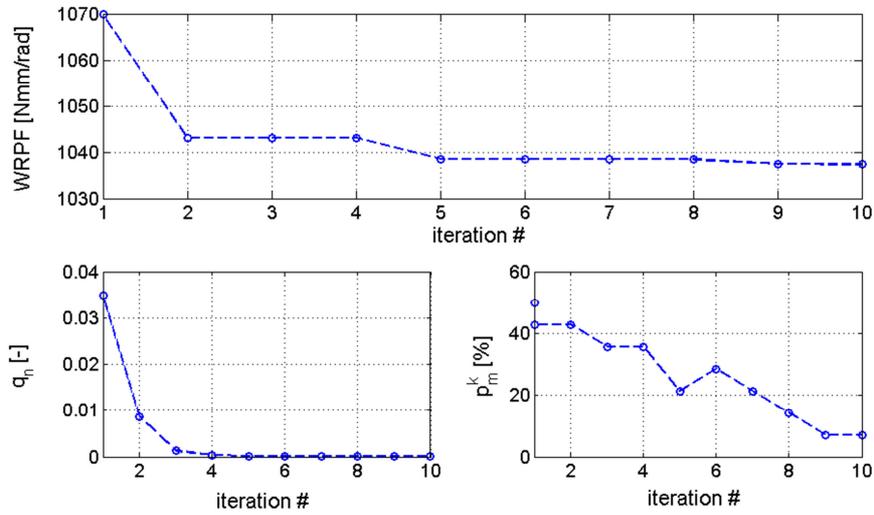
Figure 56: Algorithm behavior for $n = 5000$ rpm, WRPF optimization
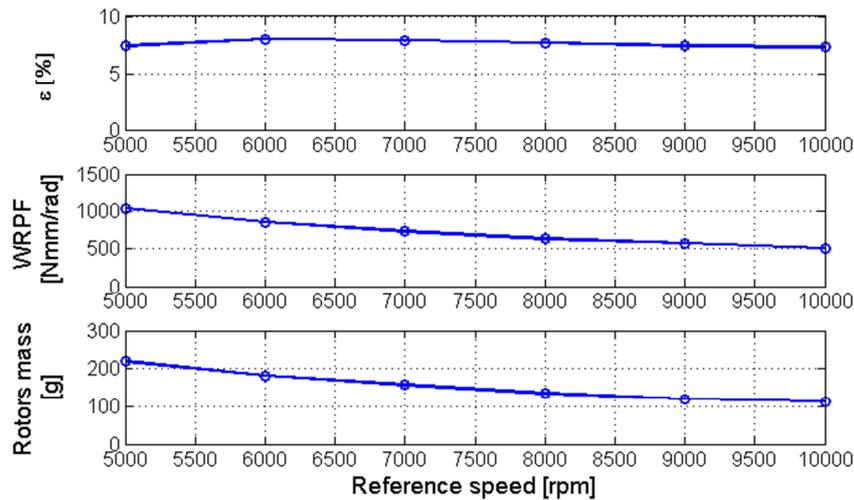
Figure 57: Cycloidal profile: single objective optimization results

A comprehensive description of the (λ, e) couple for each case is provided in Fig.58-(a), while the corresponding rotors geometries are reported in Fig.59. In particular, some interesting considerations may be performed: it can be noted how the rotor mass minimization makes use of the highest value of eccentricity and the lowest λ parameters, while the opposite happens for the flow irregularity. Wear optimization finds itself in the middle of the other two cases. From the perspective of a multi-objective optimization, this seems to suggest that the minimization of the $(\varepsilon; \text{WRPF})$ and $(m; \text{WRPF})$ couples may be obtained more easily than the $(\varepsilon; m)$ one. Looking at the Fig. 58-(b) it is possible to notice the immediate

\

consequences of the different (λ, e) sets. The profiles optimizing the rotors mass presents higher teeth, hence generating chambers with higher frontal areas and shorter pumps. On the other side, geometries optimizing the flow rate irregularity features small teeth able to provide a more regular flow rate output at the expense of longer and hence heavier devices.
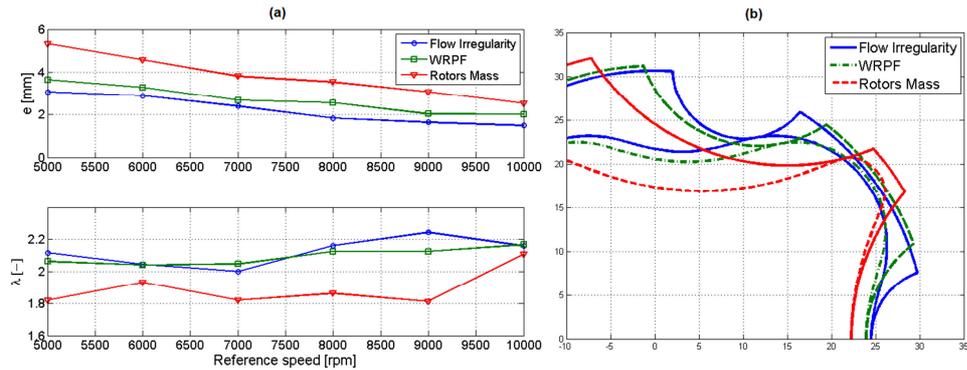
Figure 58: Optimized cycloidal case: (a) parameters - (b) geometries (5000 rpm)
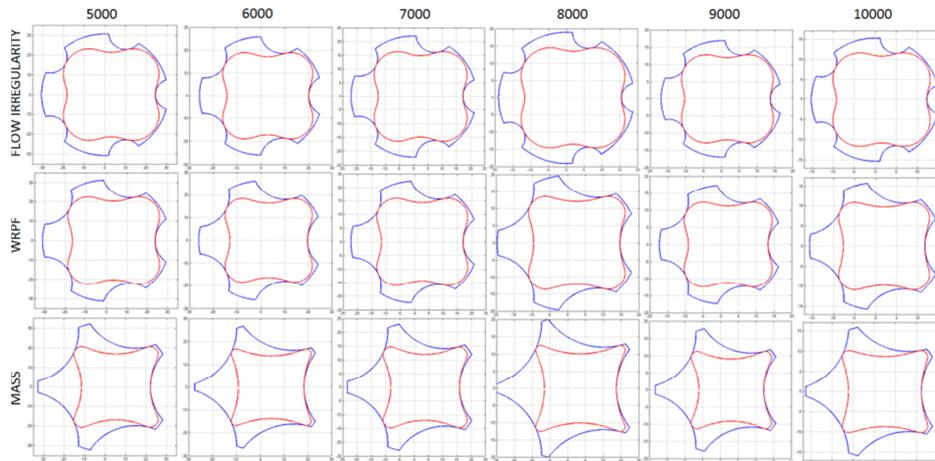
Figure 59: Optimized cycloidal profiles in the 5000 – 10000 rpm range

Looking at the profiles depicted in Fig. 59, it is possible to notice how their shape seems to be almost independent on the reference speed and only changes in function of the optimization objective. An explanation to this behavior can be provided by looking at Fig. 59-(a) and noticing that the eccentricity of the optimized profiles tends to decrease linearly with speed. From Chapter 2 it is known that the radial size of the gerotor pump is inversely proportional to the speed of the driving gear; hence the ratio between the eccentricity of each optimum solution and the radial size of the device should be constant given the

inlet pressure, fluid properties and optimization objective. Results for the studied profiles are presented in Fig. 60.
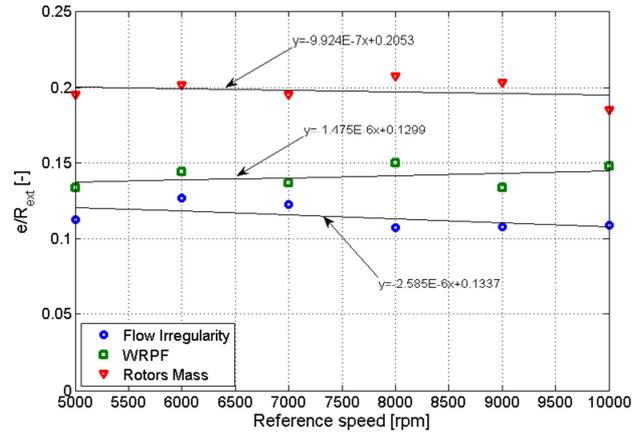
Figure 60: e/R_{ext} for the optimized cycloidal profiles

9.3.2 Asymmetric profile optimization (4 parameters)

In Chapter 8 we studied how the use of asymmetric teeth profiles could be useful to increase the flow rate capability of radial ports gerotors while highlighting their effects on the other performance indexes, flow rate irregularity and wear rate over the others. In this case the investigation is focused on the possibility to use the asymmetric lobe concept to design gerotor pumps able to provide optimum results over two or more of the considered performance indexes. Several multi-objective optimization cycles have been run and their results compared with the performance indexes of the reference profiles for the cycloidal case. It has to be underlined that this study is much more general than the one performed in Chapter 8, since its results are independent on the ports' configuration, being hence valid for both radial and axial inlet/delivery solutions.

The multi-objective optimization study considers four possible cases. At first the following three couples of objectives are considered: $(\varepsilon; \text{WRPF})$, $(\varepsilon; m)$ and $(m; \text{WRPF})$. Hence the routines are applied to the complete optimization and their results reported in Figs. 61, 62 and 63, where they are compared to the single optimization results for the traditional profiles. The profiles optimizing the $(\varepsilon; \text{WRPF})$ couple average an increase of the flow rate irregularity equal to 1.54% with respect to the reference values while the mean WRPF value sees a -0.96% variation with respect to the singly-optimized traditional profile. The estimated rotors mass increases of an average 16.08% with respect to the cycloidal solution.

\
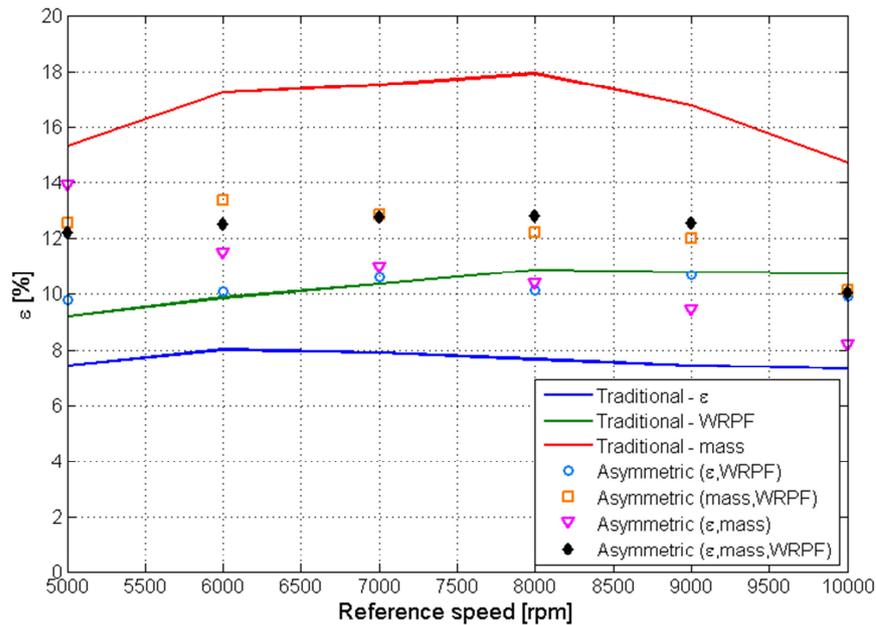
Figure 61: Multi objective optimization results: flow rate irregularity

The profiles for the $(m; \text{WRPF})$ objective couple is affected by a higher increase of the flow rate irregularity, averaging 3.53%. On the contrary the results for the WRPF (-2.85%) and estimated rotor mass (+4.92%) are far more favourable. The optimization of the $(\varepsilon; m)$ couple fails to provide interesting results, increasing the flow rate irregularity (+2.08%), the computed WRPF (+6.91%) and the rotors mass (+11.99%). Those results may be explained by looking at Fig. 59, where it is highlighted how the geometrical parameters characterizing the cycloidal profile optimizing the flow irregularity and the rotor mass are far from each other: to obtain low weights high value of eccentricity and low λ are needed, while the exact opposite happens to reduce the flow rate irregularity. The most interesting results are related to the multi-objective optimization performed over the combination of the three performance indexes; the profiles generated in this case loose of around the 3.49% in flow rate irregularity with respect to the single-optimization cycloidal profiles, the 3.21% for the WRPF and the 4.80% with respect to the estimated rotors mass. In Fig. 64 are reported the profiles generated by the multi-objective optimization process. It is interesting to notice that the ratio between the two semi-axis of the elliptic teeth tends to be higher in the two-objective optimization cases than what happens in the three-objective cycles; its average value is of 1.25 for the $(\varepsilon; \text{WRPF})$ couple,

1.35 for $(m; \mathrm{WRPF})$ and 1.22 for $(\varepsilon; m)$ while it falls to 1.12 for the final case $(\varepsilon; m; \mathrm{WRPF})$.
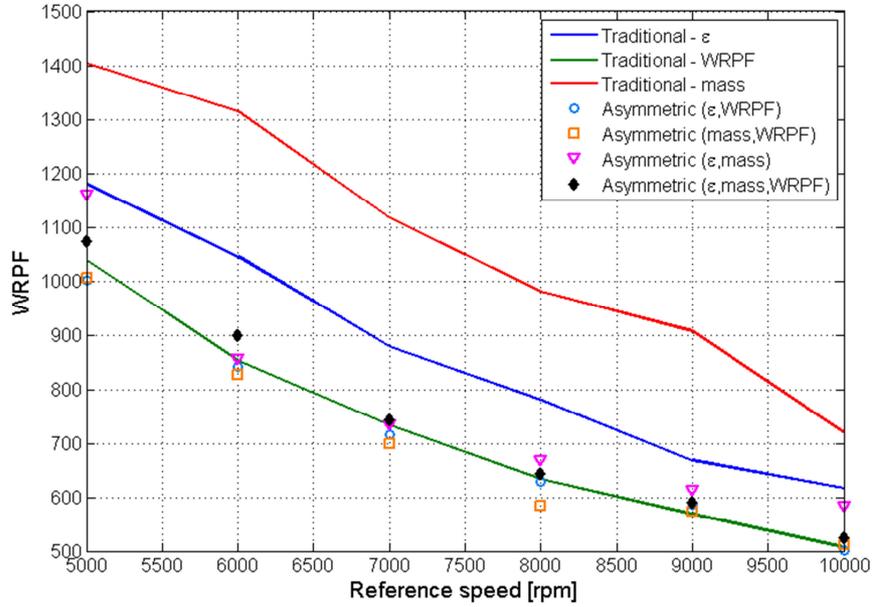
Figure 62: Multi objective optimization results: WRPF parameter
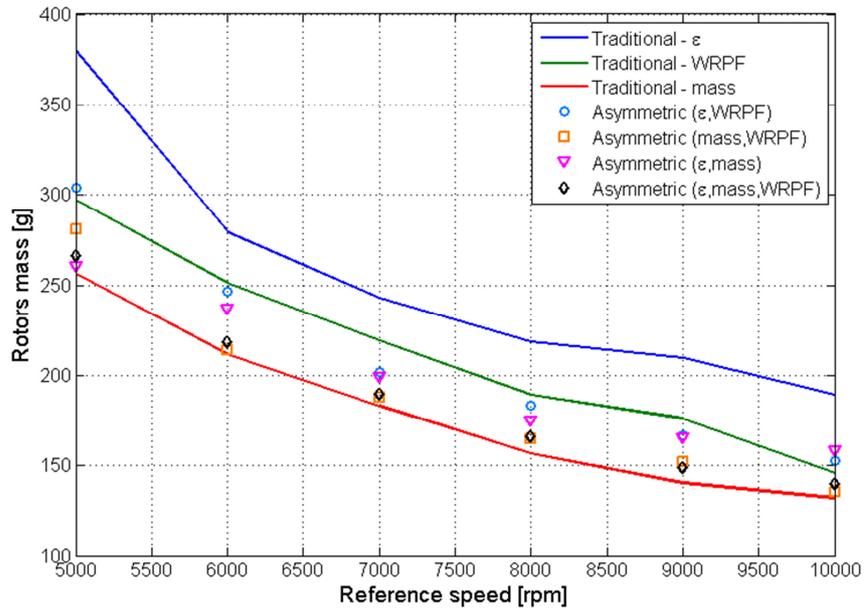
Figure 63: Multi objective optimization results: rotors mass

\
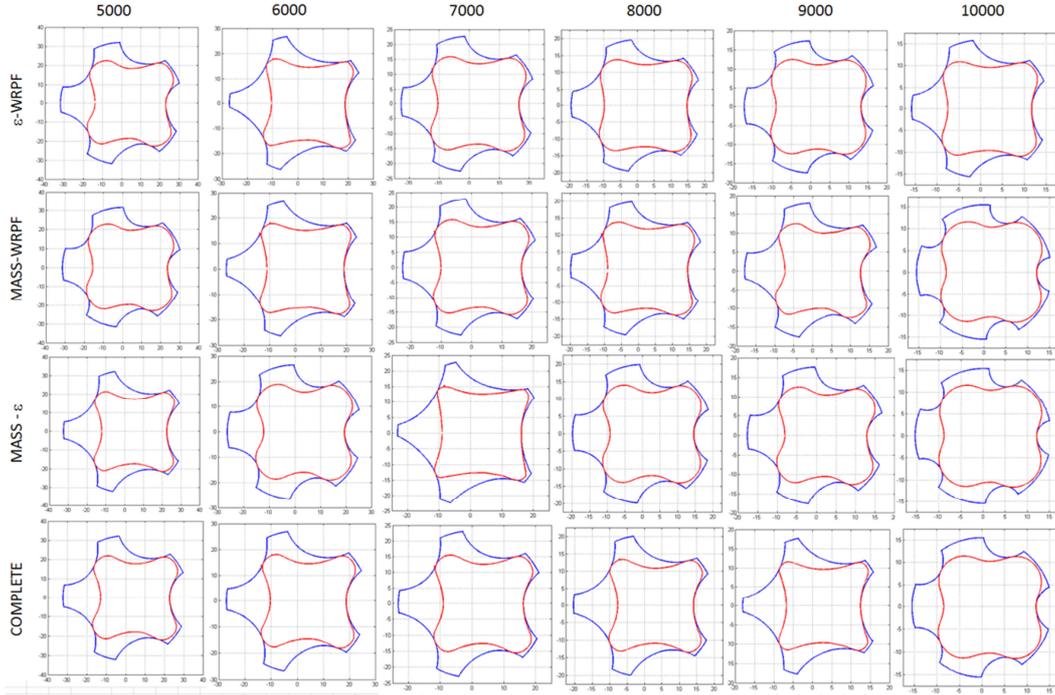
Figure 64: Optimized asymmetric profiles in the 5000-1000 rpm range

9.3.3 Asymmetric profile optimization (2 parameters)

The asymmetric lobe design could also be used as a second order optimization on an optimized circular lobe profile. In this situation, the optimization parameter $\boldsymbol{d}$ is reduced to:

$$\boldsymbol{d} = \begin{bmatrix} k_1 \\ k_2 \end{bmatrix} \tag{120}$$

While the (λ, e) couple is determined by the optimization of the traditional profile. For this analysis, we perform a second order optimization on each cycloidal profile obtained minimizing the performance indexes obtained in Chapter 9.3.1. The second order optimization has been again performed over the combinations between the flow rate irregularity, rotors mass and WRPF. The optimized parameters are reported in Table 3. The second order optimization, as shown in Figs. 65, 66 and 67, allows to achieve noticeable advantages on the performance indexes. Starting from the couple optimized for the flow rate irregularity, the use of asymmetric teeth allows to obtain minor reduction in the rotors mass (-5.68%), while the expected flow-rate irregularity (+0.29%) and wear rate (+0.03%) remain almost constant. In a similar fashion, the second order optimization allows to obtain some advantages when applied to the WRPF

optimized profiles, achieving small reduction in the expected (-0.66%), wear rate (-1.31%) and rotors mass (-0.24%). Much more significant are the results related to the second order optimization of the traditional profiles firstly optimized with respect to the estimated mass. In this case, the use of asymmetric teeth allows to obtain an average decrease of the flow irregularity computed as the 1.40%, while the estimated rotors mass sees an average variation equal to -3.23%; more importantly, a significant decrease (-14.61%) can be appreciated in the estimated wear rate. It is important to summarize the major highlights related to the second order optimization:

- Provides advantages to each performance index
- Does not provide any disadvantages to the performance indexes
- It is possible only through asymmetric teeth

We can hence conclude that the use of asymmetric teeth can be justified since it provides an additional layer of optimization that allows to further enhance the pump performance.

Table 3: **Second order optimization parameters**

Speed [rpm]	Objective of the 1st optimization process											
	(ε)				(m)				$(WRPF)$			
	λ	e	k_1	k_2	λ	e	k_1	k_2	λ	e	k_1	k_2
	[-]	[mm]	[-]	[-]	[-]	[mm]	[-]	[-]	[-]	[mm]	[-]	[-]
5000	2.118	3.074	0.720	1.159	1.820	5.326	0.747	1.070	2.063	3.643	0.939	1.115
6000	2.046	2.880	0.753	1.179	1.932	4.582	0.834	1.142	2.041	3.279	0.879	1.114
7000	2.000	2.388	0.775	1.037	1.821	3.807	0.780	1.091	2.047	2.671	0.851	1.099
8000	2.162	1.829	0.743	1.179	1.862	3.537	0.765	1.028	2.126	2.558	0.805	1.041
9000	2.244	1.636	0.878	1.109	1.813	3.074	0.761	1.080	2.126	2.025	0.815	1.175
10000	2.159	1.486	0.757	1.016	2.110	2.525	0.913	1.103	2.168	2.014	0.859	1.122

\
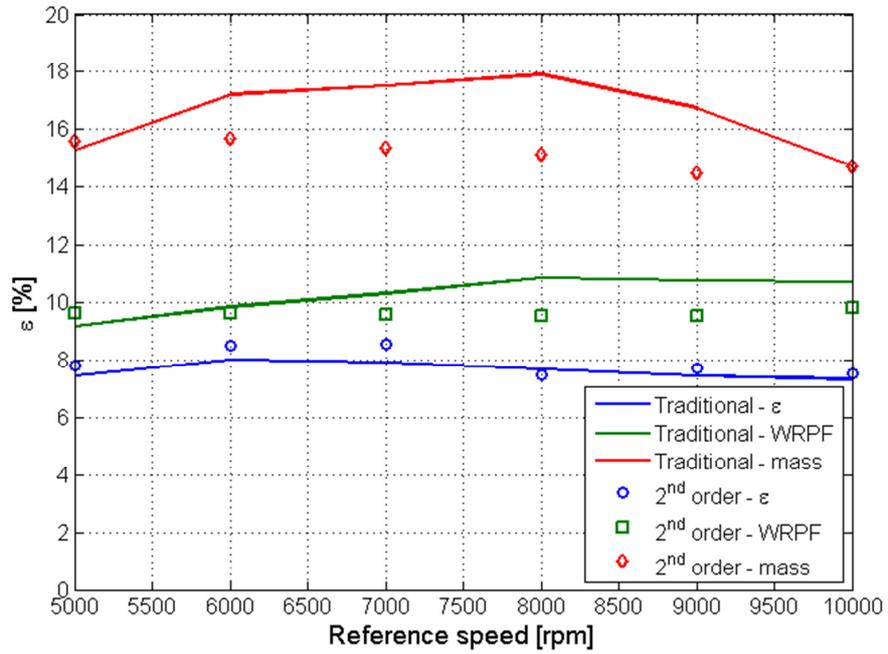
Figure 65: 2nd order optimization results: flow rate irregularity
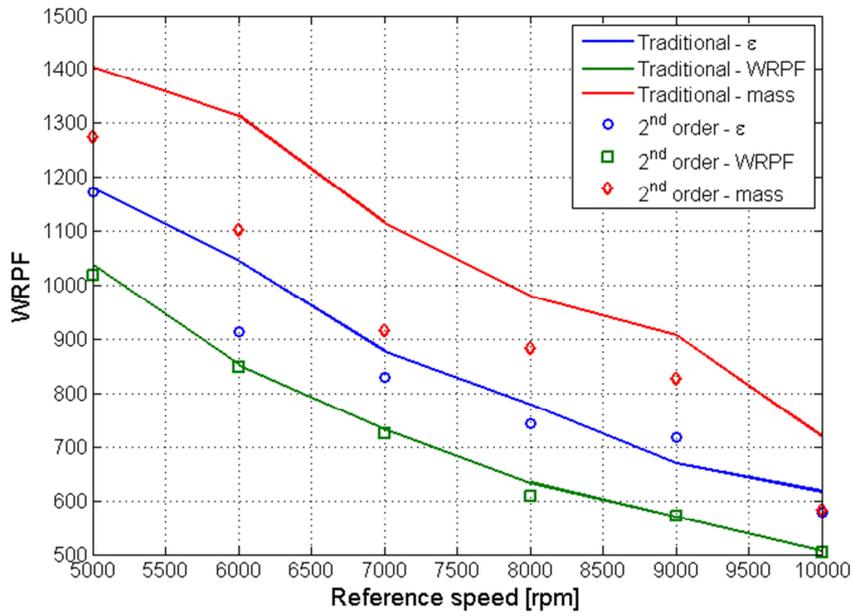
Figure 66: 2nd order optimization results: WRPF
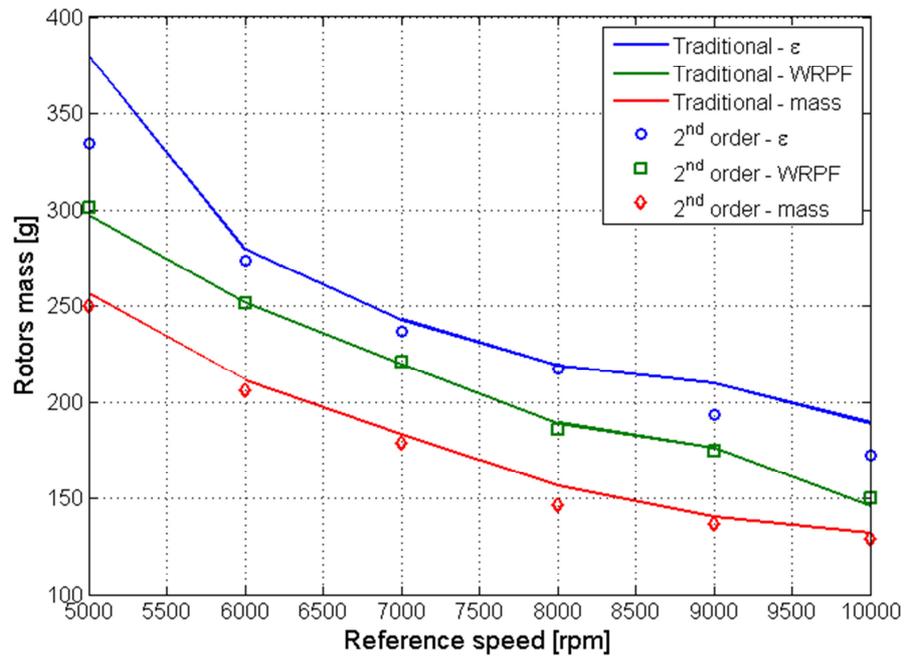
Figure 67: 2nd order optimization results: estimated rotors mass

\

Chapter 10

An alternative approach to wear optimization for gerotor profiles

10.1 Introduction

In Chapter 5 the Wear Rate Proportional Factor (WRPF) has been introduced; firstly proposed by (Kwon, Kim, & Shin, Analytical wear model of a gerotor pump without hydrodynamic effect, 2008), this parameter has hence been frequently used in literature to optimize the gerotor pumps' profiles with respect to the expected wear rate during their operative life. Although extremely simple to compute, it is based on the theoretical assumption that no lubrication exists in the contact area. Given the definition of the WRPF parameter, its optimization would generally tend to generate profile which minimize the relative speed between the meshing gears.

Both the hypothesis and the optimization results can be object of discussion. In a volumetric pump, moreover in a rotary pump conveying lubricant fluid, the hypothesis of lubrication absence is likely to be invalid. Moreover, the lubrication effectiveness, and hence the normal load which can be sustained by the lubricant film, is heavily dependent on the relative speed between the wet surfaces, tending to decrease with the fluid speed (Stachowiak & Batchelor, 2005). As such, the results of the WRPF-based optimization process can be sub-optimal for the lubricant effectiveness. To justify the use of WRPF in our work, we compare the behavior of WRPF-optimized gerotors with the results of an alternative approach to wear optimization aimed at minimizing the possibility of a direct metal-on-

metal contact and based on the assumption of the occurrence of the Elasto-Hydrodynamic Lubrication (EHL) conditions.

10.2 Basic theory for Elasto-Hydrodynamic Lubrication

According to the basic theory reported by (Stachowiak & Batchelor, 2005), the minimum thickness of lubricant film h_0 for the EHL regime can be described in non-dimensional form through the non-linear mappings f_0.

$$H_0 = f_0(U, G, W) \tag{121}$$

H_0 is the non-dimensional minimum thickness, related to the reduced radius of curvature R_t through the following equation.

$$H_0 = \frac{h_0}{R_t} \tag{122}$$

The non-dimensional speed parameter U, the materials' parameter G and the contact force parameter W are instead defined as:

$$\begin{cases} U = \dfrac{u_l \mu_0}{E_t R_t} \\ G = \alpha_\mu E_t \\ W = \dfrac{w}{E_t R_t} \end{cases} \tag{123}$$

Where u_l is the average fluid speed in the lubricated zone, μ_0 is the fluid dynamic viscosity, α_μ is the viscosity/pressure coefficient, w is the contact force and E_t is the reduced Young modulus of the contacting materials.

A simple yet effective way to evaluate the lubrication effectiveness is to compute the Tallian parameter λ_T (Tallian, 1967) defined as the ratio between the minimum thickness of the lubricant film and the mean rugosity of the wet surfaces:

$$\lambda_T = \frac{h_0}{\sqrt{R_a{}^2 + R_b{}^2}} \tag{124}$$

According to (Stachowiak & Batchelor, 2005), wear rate of mechanical components is severely limited with $\lambda_T \gg 1$, with (Stachowiak & Batchelor, 2005) suggesting an optimal value in $\lambda_T \approx 3$; if the value of the Tallian parameter

\

falls towards zero, the film behavior approaches the "boundary lubrication" regime and direct contact between the mating surfaces may occur.

10.3 Novel optimization objective

According to (Stachowiak & Batchelor, 2005) it is difficult to define a precise threshold value of the Tallian parameter under which the lubrication is no more effective; traditionally the limiting value was assumed to be $\lambda_T = 1$, but authors provided several example of machinery working without significant wear issues even for values slightly below this threshold.

Addressing with y_A and y_B the position of the relative position of the profile of the two mating surfaces along the normal to the contact zone we can write:

$$\begin{cases} y_A(R_a) = v(R_a) \\ y_B(h_0, R_b) = h_0 + \omega(R_b) \end{cases} \tag{125}$$

Where $v(R_a)$ and $\omega(R_b)$ are non-Gaussian distributions accounting for the rugosity of the two surfaces. For a given value of h_0, we can hence estimate the probability of direct contact between the asperities of the two surfaces as

$$p(y_A | y_B, h_0) = \int_{-\infty}^{+\infty} \delta(y_A)\delta(y_B) \tag{126}$$

Where $\delta(y_A)$ and $\delta(y_B)$ are the density probability functions for y_A and y_B. Repeating the analysis for each of the N contact points along an entire revolution it is possible to define an average value of the contact probability.

10.4 Optimization results and conclusions

Assuming that the peak an valleys of the two mating surfaces could be approximated by two normal distributions each with variance equal to 0.8 μm, we apply the single-objective optimization method described in Chapter 9.2.1 to the direct contact probability defined by Equation (126) over a reference speed range varying between 5000 rpm and 10000 rpm.

Results are collected and compared to the single-objective optimization performed over the WRPF parameter in Fig. 68., while the values of the WRPF factor for each profile are reported, along the minimum value of the Tallian's parameter $\lambda_{T,min}$, in Table 4.
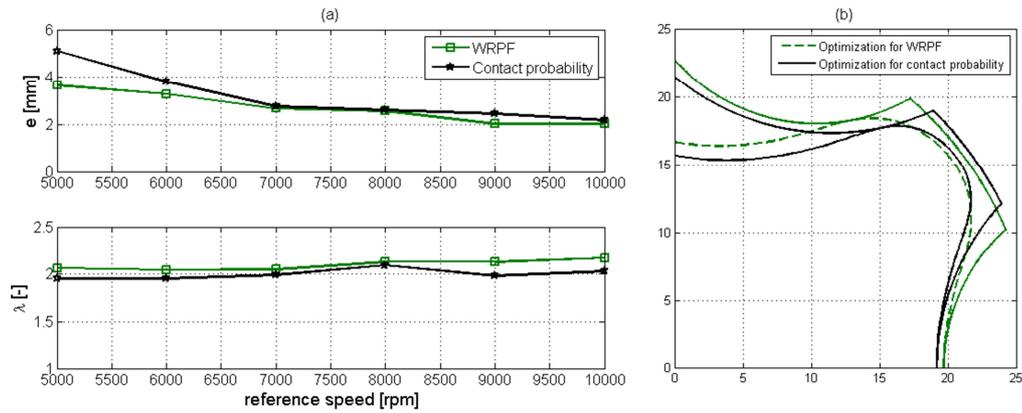
Figure 68: Optimized cycloidal case: (a) parameters - (b) geometries (6000 rpm)

The difference in the parameters defining the geometries of the pumps optimized with regards to the two objective is more noticeable in the low speed range, becoming less significant for angular frequencies higher than 7000 rpm. By looking at the effects of these geometrical differences on the pump behavior we can draw some preliminary conclusion regarding the use of the Wear Rate Proportional Factor as a parameter. Observing the results reported in Table 4 and in Fig. 69, it is possible to notice that the profiles optimized towards the probability of direct contact (P.o.c) between the two gears profiles allows to obtain minimum values of the Tallian parameter higher than those obtained through the WRPF optimization.
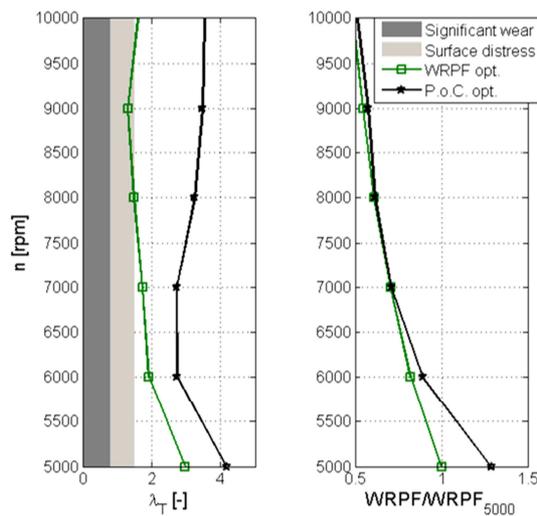
Figure 69: WRPF and Tallian parameter comparison

\

It is interesting to notice however, that the minimum values of the Tallian's parameter computed for the WRPF-optimized profiles tends to be significantly higher than 1, that is usually presented in literature as a first-approximation threshold under which issues in lubricant behavior may occur (Stachowiak & Batchelor, 2005). By comparing the WRPF values, significant differences only emerge for low reference speeds. In absence of experimental results highlighting the long-term effects of working with less favorable, but far from critical, lubricating conditions, the use of the WRPF as the primary objective for gerotor profiles optimization with respect to wear is hence justified.

Table 4: Comparison between results of profiles' wear optimization

Index	Objective	Reference speed [rpm]					
		5000	6000	7000	8000	9000	10000
WRPF	*WRPF*	1038	853	733	633	569	507
	P.o.c.	1341	928	740	642	600	536
$\lambda_{T,min}$	*WRPF*	2.98	1.92	1.74	1.5	1.32	1.62
	P.o.c.	4.19	2.75	2.74	3.26	3.49	3.15

Chapter 11

CFD survey on poppet valve behavior

11.1 Introduction

Poppet relief valve are safe-critical components widely applied in fluid power systems to keep the pipes pressure under a predefined threshold. Their simplest configuration makes use of a preloaded spring acting on one side of a poppet; the pipe pressure acts on the other side of the poppet through an inlet port. The poppet stays in position until the pipe pressure origins a force which is lower than the spring preload; when this threshold is overcome, the poppet lifts and the proper amount of fluid is discharged through the valve so that the pipe pressure remains almost constant. Although being often simple components, their sizing and optimization can become difficult, requiring significant experimental efforts. Subject of this study is the definition of a general framework for the preliminary design of poppet relief valves, able to evaluate a priori their static performances under different environmental conditions. The analysis refers to simulations obtained with MIL-L-23699 oil, but can be eventually extended to any uncompressible fluid with a similar rheological behavior.

11.2 Steady-state model

To perform the preliminary sizing of the poppet and of the preloaded spring, we refer to steady-state conditions. Under this simplifying hypothesis, we address the mechanical equilibrium of the popper and the fluid-dynamic behavior as follows.

\

11.2.1 Mechanical equilibrium on the poppet

To define a proper sizing method it is fundamental to study the mechanical equilibrium of the poppet for steady-state conditions. As shown in Fig. 70, under these assumptions the poppet is subjected to the following forces:

- pa: opening force due to the action of the inlet pressure p on the inlet port area a

- F_k: closing force due to the presence of the spring

- F_f: flow forces resultant

- $p_{out}A$: closing force due to the action of the outlet pressure p_{out} on the upper area of the poppet A

The static equilibrium equation can be hence written.

$$pa = F_k + F_f + p_{out}A \tag{127}$$

Addressing with p^* the cracking pressure, with F^* the corresponding force and with k the spring stiffness, it is possible to compute F_k simply as:

$$F_k = F^* + kx = p^*a + kx \tag{128}$$

Where x is the considered valve lift. The flow force term F_f is related to the change of direction that occurs to the fluid when passing through the valve's metering section. When the poppet is lifted the fluid is forced to pass through the small gap between the poppet itself and its seat. Due to the geometry of the poppet, it is deflected from its original flow direction of an angle ϑ that can be in first approximation considered equal to the cone semi-opening angle α.
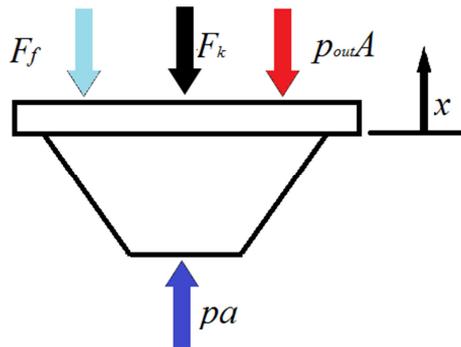
Figure 70: Poppet equilibrium

Steady-state flow force can be expressed as:

$$F_f = \rho_{oil} Q v \cos(\vartheta) = \rho_{oil} \frac{Q^2}{a} \cos(\vartheta) \tag{129}$$

Where ρ_{oil} is the oil density, Q is the volumetric flow rate through the inlet port and v the fluid mean velocity in the inlet section as per (Nervegna & Rundo, 2016).

11.2.2 Pressure-flow rate expression

The mechanical equilibrium of the poppet links the fluid-dynamics of the valve with the spring behavior, hence defining the poppet lift given the conditions of pressure and flow rate.

It is possible to correlate those physical quantities by means of the pressure-flow rate relation.

$$Q = C_d A_h \sqrt{\frac{2(p - p_{out})}{\rho_{oil}}} \tag{130}$$

Where C_d is the discharge coefficient and A_h the metering area. The metering area A_h depends on the poppet shape and current lift: it can range from a minimum value of zero, when the poppet lift $x = 0$, to a maximum value equal to the inlet port area a.

The corresponding poppet lift value, which will be addressed as "critical lift" h_{max} can be computed for conical poppet considering the following equations.

$$A_h \leq a \implies \pi D \, h_{max} \, \sin(\alpha) = \pi \frac{D^2}{4} \tag{131}$$

Defining D as the diameter of the circular inlet port, the final equation is obtained.

$$h_{max} = \frac{D}{4 \sin(\alpha)} \tag{132}$$

\

If the poppet lift overcomes the h_{max} threshold the inlet port becomes the metering section, so that $A_h = a$.

The discharge coefficient on the other hand, depends on several other factors. As reported by several authors this parameter is affected by the poppet geometry and lift, by the fluid dynamic conditions and by the material properties. A few experimental study on the subject can be found in literature; (Stone, 1960) and then (Oshima, 1989) and (Weixiang, Binggang, & Zhiyong, 1993) provided a handful of experimental results. While (Johnson, Edge, & Vaughan, 1991) and (Johnson, Edge, & Vaughan, Numerical simulation of fluid in poppet valves, 1992) provided an experimental and numerical analysis of the flow behaviour in a few types of poppet valves. It is of interest the theoretical approach by (Urata, 1969), mainly focused on the determination of the flow forces. Unfortunately no comprehensive study aimed at valve sizing can be found in literature and no mathematical expressions can be found to address the quantitative influence of each factor on the final value of the discharge coefficient.

11.3 CFD survey on discharge coefficient behavior

Lacking of the possibility to perform an extended experimental campaign, the only suitable approach to study the influence of the poppet geometry over the discharge coefficient was to pursue an in-depth investigation through the use of CFD simulations.

In order to justify the use of the CFD tools, a first study assessing the capabilities of the commercial code in use, Ansys 14, has been performed making use of established valve geometries provided by the industrial partners of the research program. Following the flow chart in Fig. 71 the mathematical model and the numerical solver have been tuned until they were able to provide results comparable with the experimental data provided.
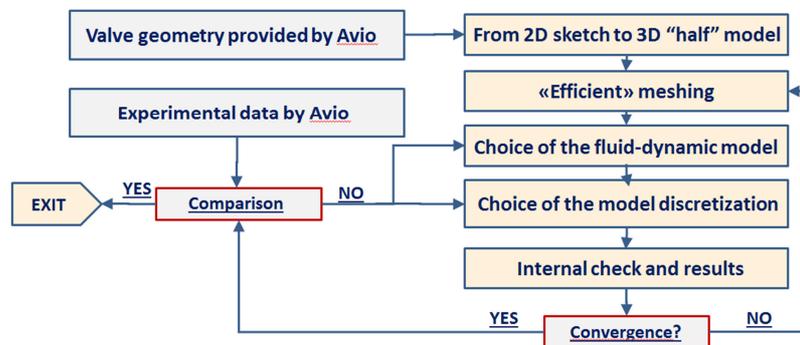
Figure 71: Model tuning scheme
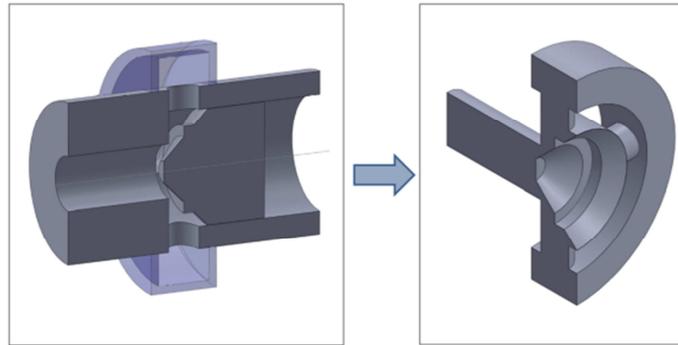
Figure 72: Example of 3D geometry

Starting from a 2D sketch of the examined valve, the corresponding 3D model has been obtained using Solidworks. Using the proper utilities the fluid control volume has been generated and introduced in Ansys 14. To better explain the process, an example not representative of the real geometry is reported in Fig. 72. To reduce the computational effort, the mesh was obtained by imposing large cells dimensions on the inlet and outlet conducts while refining the grid in the metering zone, as shown in Fig. 73. The numerical solution was performed considering only the momentum equation, using second order approximation for the spatial discretization of pressure, momentum, turbulent kinetic energy and specific dissipation rate, while using the Green-Gauss node based method for the gradient.

For inlet Reynolds numbers higher than 100 the turbulent SST k-omega model has been employed, while for Reynolds numbers lower than 10 the simple laminar flow model has been considered. For the conditions between those limits the SST k-omega with low Re correction has been employed.
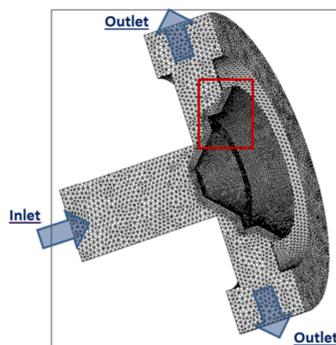
Figure 73: Mesh example

\
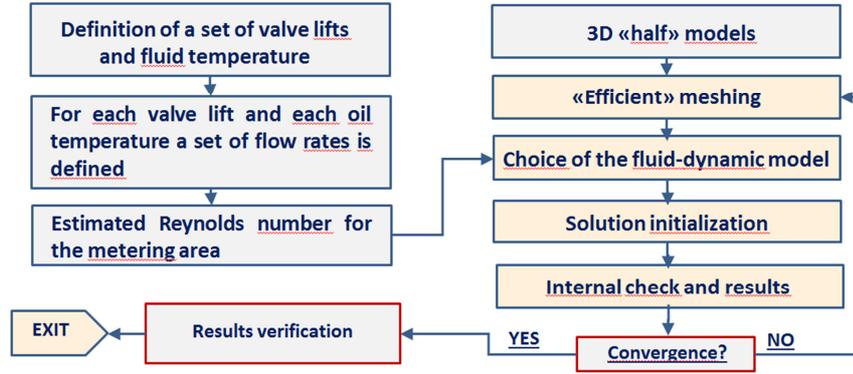
Figure 74: Procedure for the CFD survey

Tuning results and the comparison with the industrial data won't be shown due to NDA.

As stated in literature, the discharge coefficient appears to be mainly dependent on the poppet geometry, current valve lift and fluid Reynolds number. Focusing at first on simple conical devices, the corresponding input parameters are: the semi-opening angle of the cone, the ratio of the lift over its critical value, the passing flow-rate, the fluid viscosity and its density. The first step has been the definition of a set of input parameters to be repeated for each geometry; three temperature values (100°C,40°C,-40°C) determining the oil viscosity and density have been defined, as well as a certain number of poppet lifts going from zero to h_{max}. For each combination of temperature and valve lift, a set of flow rates values ranging from 0.01 l/min to 100 l/min has been defined as well.

Each CFD simulation has been performed following the procedure depicted in Fig. 74. For each operating condition the Reynolds number correspondent to the metering section of the valve has been estimated as:

$$Re = \frac{\rho v_{met} D_h}{\mu} \qquad (133)$$

Where ρ and μ are respectively the oil density and dynamic viscosity, D_h is the hydraulic diameter and v_{met} is the fluid average velocity in the metering section:

$$v_{met} = \frac{Q}{A_h} \qquad (134)$$

With A_h being the metering area.

In a similar way it has been possible to estimate the expected Reynolds number for the inlet and outlet sections Re_{in} and Re_{out}.

Those parameters have been used to provide the correct initialization to the CFD code through the computation of the inlet and outlet turbulent intensity, usually estimated as follows.

$$I_{in,out} = 0.16\left(Re_{in,out}\right)^{-\frac{1}{8}} \tag{135}$$

The other initialization parameters are the mean velocity through the inlet port and the outlet port pressure, which has been set to 0 Pa in order to simplify the results analysis.

The internal check provided by Ansys 14 and the analysis of the results convergence have been used to determine the quality of the mesh describing the studied geometry, eventually leading to its re-definition.

The most important output of the CFD analysis is the pressure *p* computed in correspondence of the inlet port. Since all operating conditions are known, the discharge coefficient for each simulation can be computed as:

$$C_d = \frac{Q}{A_h\sqrt{\dfrac{2(p - p_{out})}{\rho}}} \tag{136}$$

The results coming from the CFD simulations must be verified, since the meshing operation and the numerical integrations can introduce several errors, often unpredictable a priori. According to the best practice, results should be compared to experimental data obtained using the same controlled parameters employed in the simulations. Since there was no possibility to perform any experimental validation during the current activity, some indirect verification criteria have been used.

The first one is obtained by comparison with the results of the Von Mises theory (Von Mises, 1917), which gives the behavior of the discharge coefficient in dependence of the semi-opening angle of the conical poppet when the valve lift is very small with respect to the inlet port dimensions. Under these simplifying assumptions, the fluid can be considered as ideal, giving the results described in

\

Fig. 75. The results coming from the CFD analysis are expected to fall always below the ideal characteristics, since as reported by authors cited in Chapter 11.1, the discharge coefficient tends to decrease with the valve lift. Moreover, it has been reported by (Stone, 1960) and (Johnson, Edge, & Vaughan, Experimental investigation on flow and force characteristics of hydraulic poppet and disc valves, 1991), that high Reynolds number have almost negligible impact over the discharge coefficient: hence, reasoning at constant valve lift, notable variations in C_d are expected increasing the Reynolds number up to a critical value, after which C_d should remain almost constant.

If the simulation converge to a numerical solution which satisfies the above described criteria, the associated results are accepted and further analyzed.
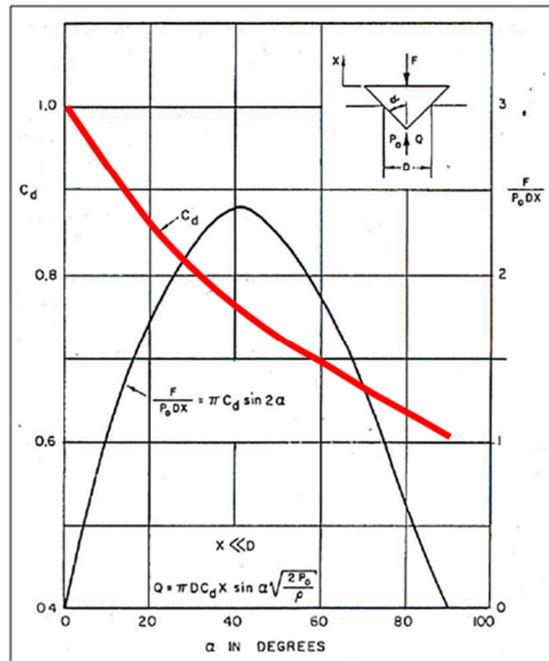
Figure 75: Discharge coefficients according to Von Mises' theory

11.4 Results analysis

This section is focused on the discussion of the numerical results obtained during the CFD simulation campaign. It is divided in three main sub-sections, addressing the influence of the operating conditions, hence valve lift and fluid temperature, of geometrical variations to reduce the static flow forces and of the cone semi-opening angle. Each of those dependence has been studied and analytical expressions for corrective coefficients based on data fitting have been proposed.

11.4.1 Influence of operating conditions

As already stated, the influence of the operating conditions over the discharge coefficients is mainly dependent on two functional parameters, which are the valve lift and the Reynolds number.

In literature, the dependence on the valve lift is often represented as the dependence on the ratio λ between the valve lift and the inlet port diameter.:

$$0 \leq \lambda = \frac{h}{D} \leq \frac{1}{4\sin(\alpha)} \tag{137}$$

Notice that the maximum value for this parameter depends on the semi-opening angle of the conical poppet. Pursuing a more general expression, a new parameter Λ expressing the ratio between the metering section and the inlet port areas is introduced:

$$0 \leq \Lambda = \frac{A_h}{\left(\pi \dfrac{D^2}{4}\right)} \leq 1 \tag{138}$$

Notice that this new parameter always falls in the range between 0 and 1, independently on the poppet geometry.

Reynolds number account for fluid velocity through the valve metering sections, hence for the actual flow rate, while considering also the environmental conditions, which have effect on oil density and viscosity.

Results of the simulation performed on conical poppets with semi-opening angle of 20°, 30° and 45° are reported in Figs. 76, 77 and 78.

\
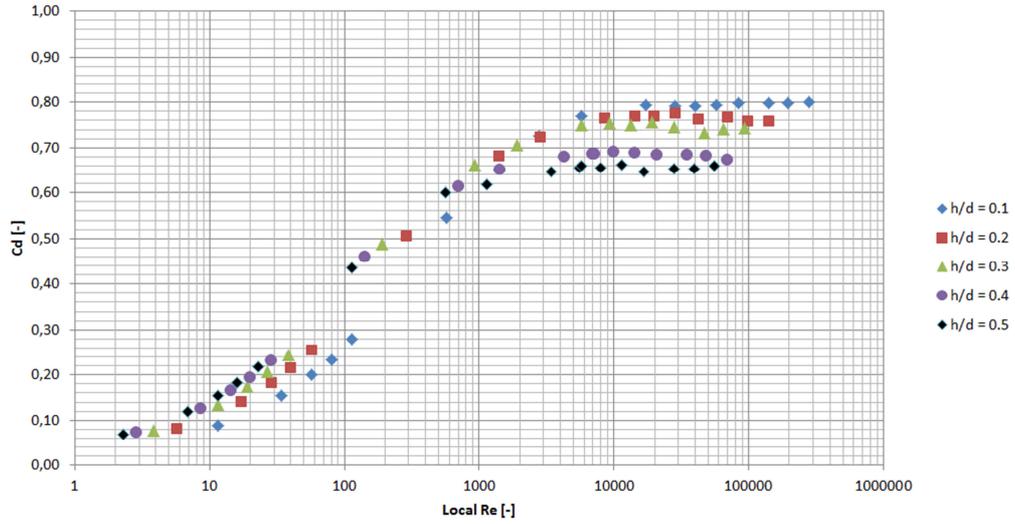
Figure 76: CFD results: discharge coefficient, $\alpha = 20°$
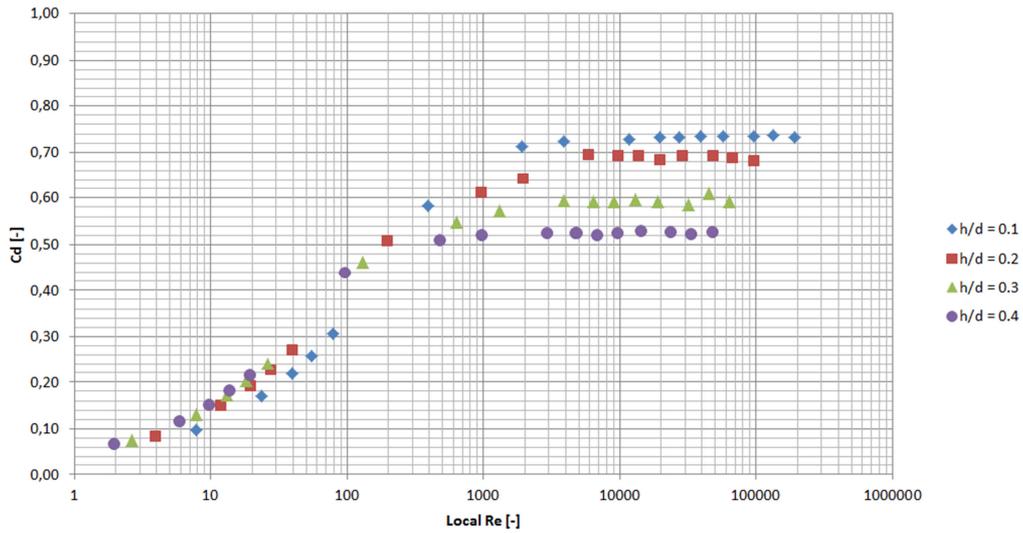
Figure 77: CFD results: discharge coefficient, $\alpha = 30°$
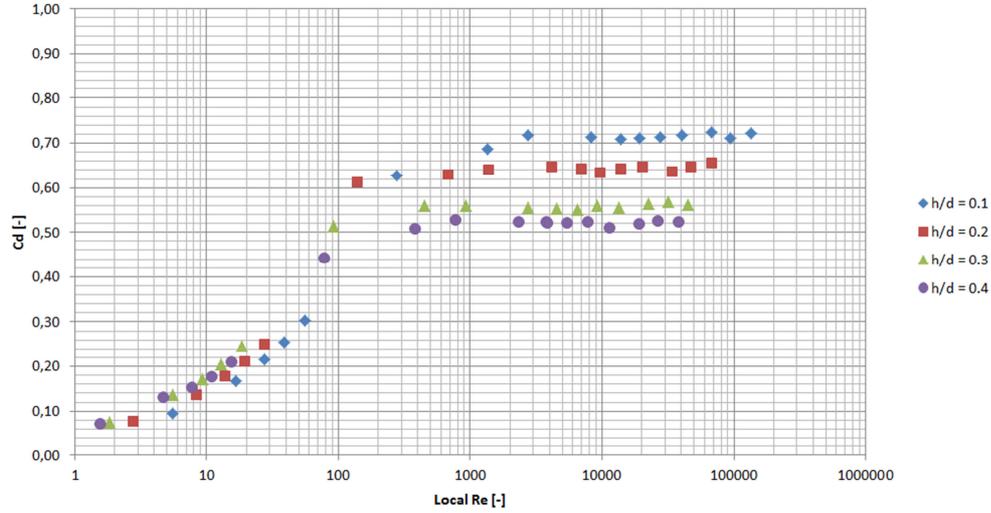
Figure 78: CFD results: discharge coefficient, $\boldsymbol{\alpha = 45°}$

Please notice that the expectations set in chapter 11.3 have been satisfied.

Now, focusing on the 45° case, a mathematical equation able to give the best possible fitting of the simulations results has been studied. Following the approach reported by (Idelchik, 2005), this operation has been performed over the parameter ζ defined as follows.

$$\zeta = \frac{1}{\sqrt{C_d}} \tag{139}$$

The polynomial fitting expression obtained is the following:

$$\begin{cases} a = \ln(1 + Re) \\ b = \sqrt{\Lambda} \end{cases}$$

$$\begin{aligned} \zeta = 7.726 - 1.03a - 11b - 0.07491a^2 - 0.0249ab + 18.18b^2 + 0.02065a^3 \\ + 0.4905a^2b - 2.695ab^2 - 10.14b^3 - 0.00121a^4 \\ - 0.04857a^3b - 0.04368a^2b^2 + 2.126ab^3 + 2.375 \cdot 10^{-5}a^5 \\ + 0.001214a^4b + 0.01126a^3b^2 - 0.1005a^2b^3 \end{aligned} \tag{140}$$

The resulting values of for the discharge coefficient are reported in Fig. 79. The discharge coefficient computed through this first expression will be addressed as $C_{d,0}$ in the following sections.

\

$$C_{d,0} = \frac{1}{\zeta^2} \qquad\qquad (141)$$
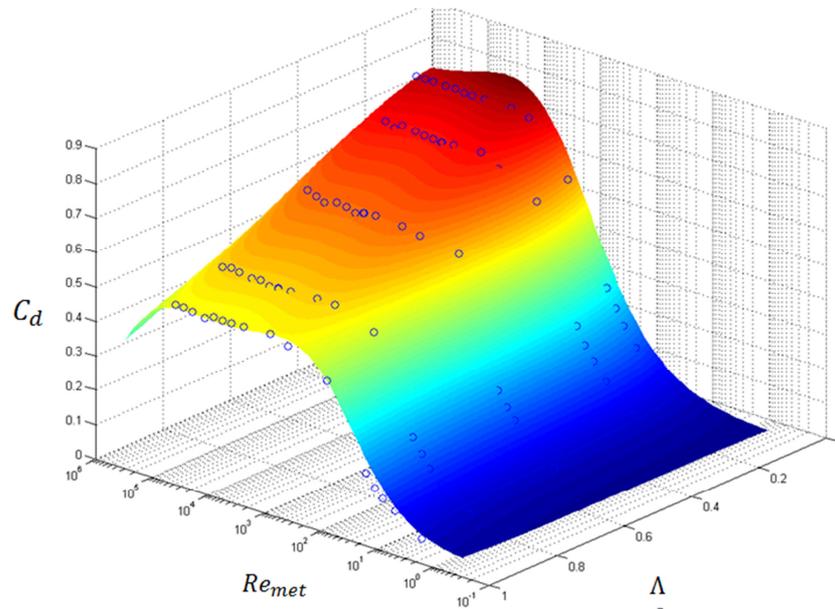
Figure 79: Polynomial fitting vs CFD results, $\boldsymbol{\alpha = 45°}$

11.4.2 Dependence on the semi-opening angle of the cone

Apart from the operating conditions, the most significant influence over the discharge coefficient comes from the poppet and the seat geometry. In example, (Johnson, Edge, & Vaughan, Experimental investigation on flow and force characteristics of hydraulic poppet and disc valves, 1991) demonstrated that chamfered seats allows to obtain generally better results; it is however difficult, at the current state of the art, to guarantee the appropriate tolerances, so that sharp edge seats are usually preferred.

The approach used to evaluate the effects of the conic angle variation over the discharge coefficient is different from the study of the operational conditions influence. In this case, the idea is to compute a corrective coefficient K_α by interpolating the ratio between the discharge coefficient C_d computed for a certain couple of parameters (Λ, Re) with a semi-opening angle α and the discharge coefficient $C_{d,0}$ obtained for the same couple of input parameters for a cone with a 45° semi-opening angle.

Performing this operation with $\alpha = 20°$, it is possible to obtain the following polynomial expression:

$$
\begin{aligned}
K_{20} = \frac{C_d(\Lambda, Re, 20°)}{C_d(\Lambda, Re, 45°)} \\
= -2.728 + 2.813a + 6.003b - 0.7848a^2 - 3.85ab \\
- 3.889b^2 + 0.1052a^3 + 0.7052a^2b + 2.44ab^2 + 0.4233b^3 \\
- 0.00681a^4 - 0.05348a^3b - 0.3066a^2b^2 - 0.468ab^3 + 1.7 \\
\cdot 10^{-4}a^5 + 0.001545a^4b + 0.009853a^3b^2 - 0.04502a^2b^3
\end{aligned}
\tag{142}
$$

Parameter K_α variation between $20°$ and $45°$ is assumed to be linear with α and as such is expressed as:

$$
K_\alpha = \frac{C_{d,a}}{C_{d,0}} = 1 - \frac{1 - K_{20}}{45° - 20°}(45° - \alpha)
\tag{143}
$$

The results of this approximation have been evaluated applying the last expression to the $\alpha = 30°$ case and comparing the obtained values with the CFD analysis. For each (Λ, Re) couple, the corresponding K_{20} parameter is computed, allowing then to obtain the corresponding K_{30}. As shown in Fig. 80, the relative error is limited and doesn't show any systematic nature.
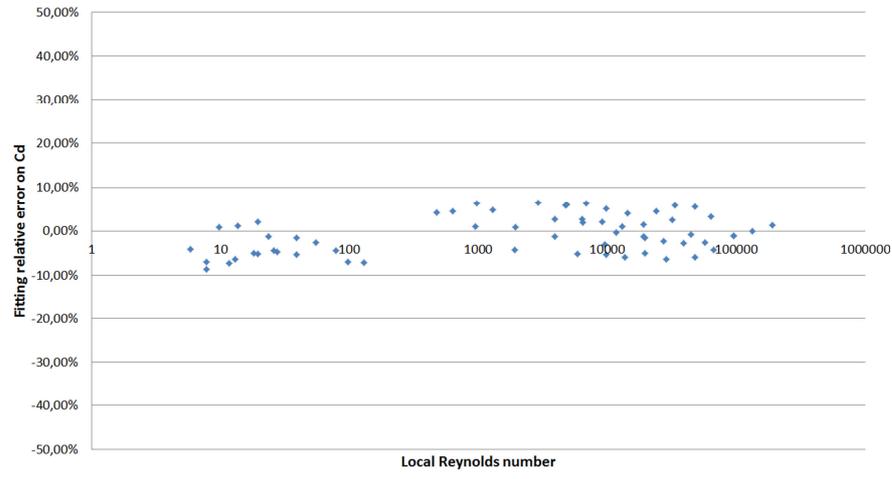
Figure 80: Relative error on C_d, $\alpha = 30°$

\

11.4.3 Influence of flow-force reduction geometry

The last factor influencing the valve discharge coefficient addressed in this section is the presence, and the position, of geometrical changes to the poppet to decrease the flow force resultant. Those geometrical variations usually translate into the addition of a cylindrical plate on top of the poppet. Its usage is expected to have some influence over the discharge coefficient. The study is focused only on the position of the plate and not on its dimensions, hence its validity is limited to provide some first-approximation estimates.

The followed approach is similar to that employed for the study of the cone angle influence, so that another corrective coefficient K_{plate} is defined as the ratio of the discharge coefficients with and without the additional plate:

$$K_{plate} = \frac{C_{d,plate}}{C_{d,no\ plate}} \tag{144}$$

The position of the plate along the axial direction of the inlet port is identified through the quantity l described in Fig. 81, while an example can be found in Fig. 82.
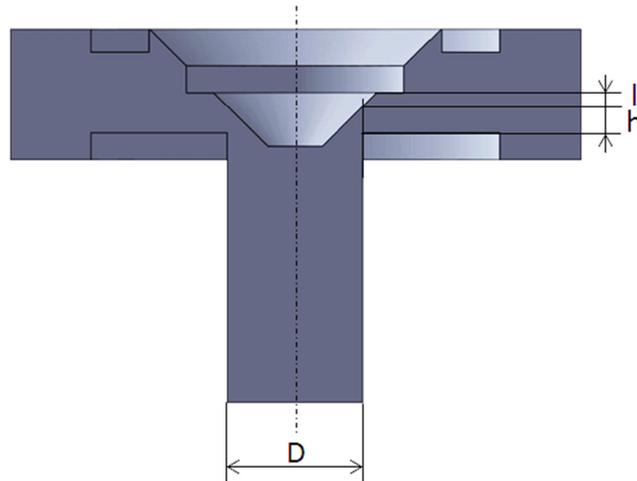
Figure 81: Geometrical quantities meaningful to the analysis
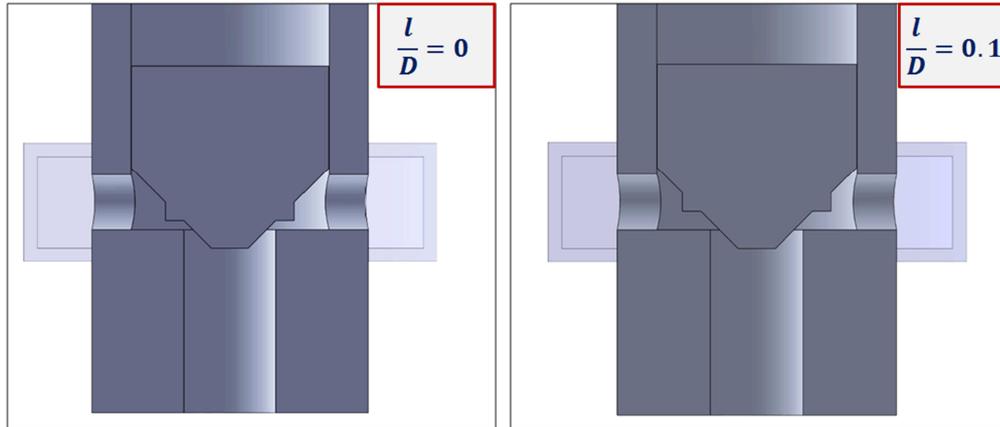
Figure 82: Examples for different valued of l/D

CFD analysis were at first performed on a conical poppet with 45° semi-opening angle ranging the l/D ratio between 0 and 0.3. The analysis have been then repeated on 20° and 30° cases. As shown in Fig. 83, the influence of the plate over the discharge coefficient becomes almost negligible for $l/D \geq 0.2$; moreover the contribute of the plate presence can be considered as independent from the poppet cone angle. It can be observed that the dependence on the plate position tends to decrease with the increase of the valve lift, becoming negligible for $\Lambda \cong 1$, as depicted in Fig. 84.
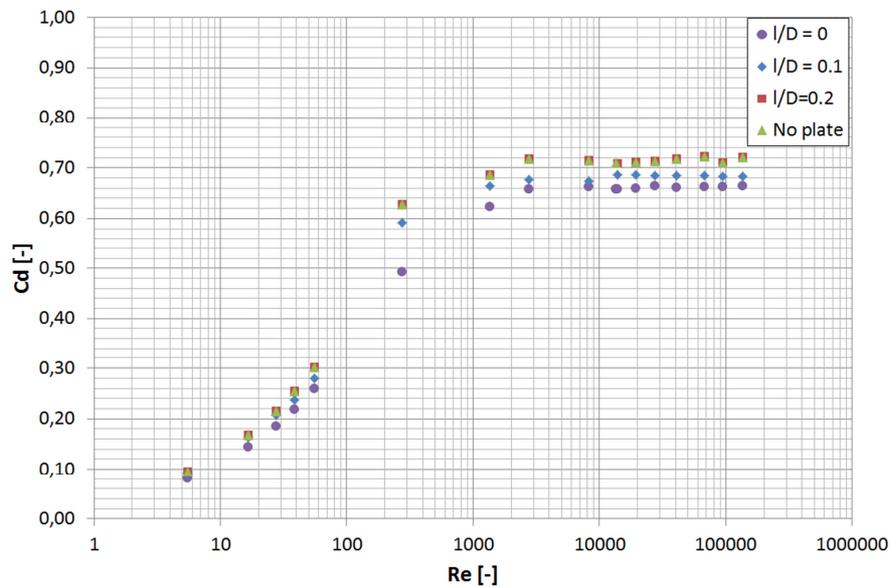
Figure 83: Variation of C_d with l/D, $\alpha = 45°$

\
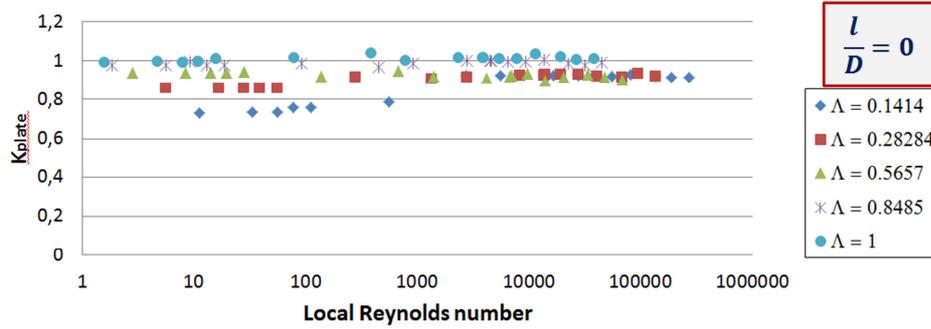
Figure 84: Variation of K_{plate} with Λ, $\alpha = 45°$

As done for the other factors affecting the overall discharge coefficient, the analysis starts from obtaining an expression for the corrective coefficient K_{plate} through the fitting of CFD data coming from the simulation in some particular conditions.

In this case, the studied condition features $l/D = 0$ and a semi-opening angle of the conical poppet equal to $45°$. Under those assumptions it is possible to write the following expression, linking the corrective factor to the local Reynolds number and to the valve lift.

$$
\begin{aligned}
K_{plate,0} = \frac{C_{d,plate}(^l/_D = 0)}{C_{d,noplate}} \\
= 0.3291 + 0.006832a + 3{,}704b + 0.05782a^2 \\
- 0.5166ab - 7{,}845b^2 - 0.007398a^3 - 0.05746a^2b \\
+ 0.9321ab^2 + 7.261b^3 + 0.008209a^3b - 0.009665a^2 \\
- 0{,}3886ab^3 - 2.471 \cdot 10^{-5}b^4
\end{aligned}
\tag{145}
$$

The value of K_{plate} obtained using this equation is the lowest possible for a certain couple of (Λ, Re), since it considers the worst possible condition. As written before in this section, the influence of the plate becomes negligible for $l/D \geq 0.2$, condition for which $K_{plate} \cong 1$. The variation of the corrective coefficient in dependence of the ratio l/D has been described in first approximation with a linear expression:

$$K_{plate} = \frac{C_{d,plate}}{C_{d,no\ plate}} = K_{plate,0} + \frac{1 - K_{plate,0}}{0.2}\frac{l}{D} \qquad (146)$$

11.4.4 Final expression of the discharge coefficent

Given the corrective coefficients defined in this chapter, we propose a possible expression to estimate the discharge coefficient given the poppet geometry as:

$$C_d = K_\alpha K_{plate} C_{d,0} \qquad (147)$$

Whereas, for a given semi-opening angle, the calculated value must remain under those provided by Von Mises.

\

Chapter 12

Poppet valve sizing

12.1 Introduction

In this chapter we provide a framework to perform the preliminary sizing of a direct pressure relief valve. In particular, the presented framework makes use of the study detailed in Chapter 11 to define the poppet geometry. Starting from the requirements description, the fluid dynamic conditions for the project point are obtained and used as input for the correct sizing of the retaining spring.

Once that the spring features have been defined, the expectations regarding both the structural integrity and the valve performances in the project point are checked. Hence, a final numerical simulation in static conditions is performed in order to evaluate the valve pressure-flow rate characteristics at different operating temperature.

12.2 Sizing framework

The framework to perform the first-tentative sizing of the valve can be roughly divided in two consequent steps, that are the poppet design and the spring choice. The definition of these two components is in fact critical for the device operation and is moreover sufficient to provide an estimate of its expected volume envelope.

12.2.1 Inputs to the sizing procedure

The inputs to the sizing procedure can be divided into three categories:
- Operative requirements

- ▪ Geometrical inputs
- ▪ Fluid properties

Operative requirements are the one used to define the pressure-flow rate characteristics in the project point, as well as to impose some additional constraints. Some of these requirements are pressures values: the cracking pressure p^* the one at which the valve is set to regulate, while the discharge pressure p_{out} is an estimated value for the tank environment. The pressure at which the valve shall be completely opened is called saturation pressure and it is addressed as p_{sat}. Other parameters are the rated oil temperature for the project point and the associated flow rate value Q_n.

Geometrical inputs define the mechanical project point and determine the poppet and inlet port dimensions. Input parameters are: the semi-opening angle of the conical poppet a, the aspect ratio $\lambda = h/D$, the diameter of the inlet port D and the anti-flow-force plate position parameter $\beta = l/D$. In particular, the λ parameter determine the valve lift for the project point, which is the equilibrium point of the poppet for the flow rate Q_n and can range between *0* and a maximum value defined in Equation (131). Parameter β can instead vary between *0* and 0.2; if the poppet will dose not feature the plate, it is assumed for convenience $\beta = 1$.

The last input to the sizing procedure is represented by the following fluid properties: the curves of fluid density and dynamic viscosity at various temperature ρ and the dynamic viscosity μ.

12.2.2 Poppet sizing

The first step of the sizing procedure is the definition of the fluid mechanics conditions in the project point, in order to make a first verification on the pressure condition. If this check is passed, the input data for the spring choice are computed.

At first, it is important to understand if the project conditions are coherent, which means understand if, given all the previously described inputs, the pressure at the inlet port is within the range defined by the cracking pressure and the saturation pressure. Given the input parameters, the metering area A_h and the inlet port area *a* are computed for the rated conditions as:

$$A_h = \pi D h \sin(\alpha) \tag{148}$$

\

$$a = \pi \frac{D^2}{4} \tag{149}$$

Knowing D and a it is possible to compute the rated and maximum poppet lift h and h_{max} through equation (126); the ratio between A_h and a is the Λ parameter. Please notice that A_h maximum value is equal to a. The mean fluid velocity in the metering area v and the associated Reynolds number Re_m are computed through Equations (127) and (128). Following the process described in Chapter 11, each corrective factor for the discharge coefficient estimate is computed; the discharge coefficient for the project conditions, which means for the imposed valve lift, temperature and flow rate, is then calculated by means of equation (141).

Finally the pressure drop across the valve can be obtained by reversing the efflux equation, hence deriving the inlet pressure for the project operating point p_p:

$$p_p = p_{out} + \frac{\rho}{2}\left(\frac{Q_p}{C_d A_h}\right)^2 \tag{150}$$

If $p^* \leq p_p \leq p_{sat}$ is satisfied, then the sizing procedure can continue. Otherwise the geometrical inputs to the sizing process needs to be re-evaluated. The true saturation pressure can hence be evaluated as

$$\widehat{p_{sat}} \approx \frac{k h_{max}}{a} + p^* \tag{151}$$

12.2.2 Spring sizing

Once that the project point and the poppet geometry have been established and verified, the next operations regard the spring sizing. The most important requirements coming from the fluid mechanics computations at the rated conditions are the expected spring stiffness and its preload.

Applying equation (123) it is possible to obtain the static value for the flow-forces in the project point F_f. The preload force acting on the spring F^* and the pressure force for the project conditions F_p can be easily computed as:

$$\begin{cases} F^* = p^* a \\ F_p = p_p a \end{cases} \tag{152}$$

Combining equations (121), (122), and (146) it is possible to obtain the required spring stiffness k as:

$$k = \frac{F_p - F^* - F_f}{a} \tag{153}$$

The spring compression associated with the preload needed to guarantee the opposing force F^* can be hence computed:

$$x^* = \frac{F^*}{k} \tag{154}$$

Starting from the stiffness and preload compression requirements, the spring is geometrically defined and verified for static and fatigue loads and for instability conditions, according to the classical theory reported by (Niemann, Winter, & Hohn, 2006). The material properties needed to perform the sizing procedure are: the shear modulus G, the yield shear stress τ_y, the ultimate shear stress τ_u the fatigue limit τ_{Dx}, and the material density ρ_s. Please notice that the fatigue limit refers to the conditions described by Equation (148):

$$R = \frac{\tau_m}{\tau_a} = 0 \tag{155}$$

Where τ_m and τ_a are the medium and alternate fatigue shear stresses. The other input parameters are the number of active coils N_i and the number of end coils N_e; finally, the first attempt spring index c' can be defined as:

$$c' = \frac{d''}{D''} \tag{156}$$

Where d' is the wire diameter and D'' the coils medium diameter; its value is usually held between 7 and 12 (Niemann, Winter, & Hohn, 2006). Tolerances on wire and coil diameters, d_t and D_t can be set and used to evaluate the possible outcome of the uncertainty over the real spring size over its expected nominal behavior.

\

From the basic spring theory it is known that the spring length variation f due to an active load F can be computed as follows (Niemann, Winter, & Hohn, 2006).

$$f = \lambda'' \frac{8Fc'^3 N_i}{Gd''} = \frac{F}{k} \tag{157}$$

If $7 \leq c' \leq 12$, $\lambda'' = 1$; substituting f with x^* it is then possible to obtain a first attempt value for d'':

$$d'' = \frac{8kc'^3 N_i}{G} \tag{158}$$

The related medium coil diameter can be consequently found reversing equation (150). If the tolerances on the coil and spring diameters δ_d and δ_D have been defined, the four possible outcomes described in Table 5 can occur.

Minimum dimensions conditions is critical for mechanical resistance, maximum dimensions case is related to the most critical situation for the residual length verification, while minimum stiffness could give origin to instability issues.

For each case, the actual spring rate k' is recomputed using equation (153):

$$\lambda'' \frac{8c'^3 N_i}{Gd'} = \frac{1}{k'} \tag{159}$$

In each case, the solid length L_s of the spring can be computed as:

$$L_s = d'N \tag{160}$$

Where $N = N_i + N_e$ is the total coil number. The working travel y of the spring, which is its maximum compression, is equal to the maximum valve lift h_{max}. The actual preload compression L_p is assumed equal to x^*: this means that for each condition under examination, the cracking pressure varies.

Table 5: Considered outcomes on spring sizing due to tolerances

Nominal	Minimum dimension	Maximum dimension	Minimum stiffness
d''	$d'' - \delta_d$	$d'' + \delta_d$	$d'' - \delta_d$
D''	$D'' - \delta_D$	$D'' + \delta_D$	$D'' + \delta_D$

For nominal conditions, the residual length L_{res} is imposed equal to:

$$L_{res} = \frac{d'}{4} N_i \tag{161}$$

Hence the installed length L_0 can be obtained as:

$$L_0 = L_{res} + L_s + y \tag{162}$$

While the free length of the spring L_F is evaluated as:

$$L_F = L_0 + L_p \tag{163}$$

Once that the free length has been obtained, it is possible to compute the installed and the residual length for the non-nominal cases by reversing Equations (156) and (157). In order to be acceptable, the minimum residual length must be greater than $\frac{d'}{4} N_i$, in order to avoid contact between the contiguous coils.

According to (Niemann, Winter, & Hohn, 2006), the maximum shear stress due to static load τ_{st}, can be computed through equation (164):

$$\tau_{st} = \lambda' \frac{8 F_{max} c'}{\pi d'^2} \tag{164}$$

Where F_{max} is the maximum load acting on the spring evaluated by equation (165), while λ' is the Wahl coefficient which value for $7 \leq c' \leq 12$ is obtained through equation (166).

$$F_{max} = F^* + k' h_{max} \tag{165}$$

$$\lambda' = \frac{4c' - 1}{4c' - 4} + \frac{0.615}{c'} \tag{166}$$

The static safety coefficient CS_{st}, acceptable if higher than 1.5, can then evaluated as:

$$CS_{st} = \frac{\tau_y}{\tau_{st}} \tag{167}$$

There exist many methods for fatigue verification in springs accepted by the engineering community. Some of them, as the ones recommended by the (DIN 17221, 1988) and (DIN 17223, 1984), make use of corrective coefficients to distinguish between different production processes; those methods, while

\

certainly trustable, requires an in-depth knowledge of the spring under examination, being hence not suitable for the preliminary study proposed in this report.

The general approach for fatigue calculation through Haigh diagram is then employed. The minimum force applied to the spring is its preload F^*, while its maximum value is defined by Equation (165); hence, if no load spectrum is available, the medium fatigue load can considered to be equal to:

$$F_m = F^* + k' {h_{max}}/{2} \tag{168}$$

The alternate fatigue force is hence considered as:

$$F_a = k' {h_{max}}/{2} \tag{169}$$

Under those consideration, the medium and the alternate fatigue stress τ_m and τ_a can be computed and compared with the admissible alternate shear stress at the corresponding medium shear stress, estimated as:

$$\Delta\tau_{amm} = \tau_D - \frac{\tau_D}{{\tau_u}/{\sqrt{3}}}\tau_m \tag{170}$$

Under these hypothesis, the fatigue safety factor can be evaluated as:

$$CS_f = \frac{\tau_a}{\Delta\tau_{amm}} \tag{171}$$

If the valve geometry is such that the compression spring is not supported by external guides, there exist a critical load F_{crit} that leads to elastic instability, usually estimated as follows.

$$F_{crit} = k'L_0 K_L \tag{172}$$

Where K_L is a tabulated factor available in literature, function of the L_0/D' ratio and of the type of spring extremities (hinged or fixed) as shown in Fig. 85. In order to avoid instability conditions, the critical force computed through Equation (173) must be higher than the maximum compression force that the spring may face during operation. The last passage of the sizing procedure is the estimate of the spring resonance frequency. This operation can be performed by means of equation (174).

$$\sigma_r = \frac{d'}{D' l_{eq}} \sqrt{\frac{G}{8\rho}} \qquad (173)$$

Where l_{eq} is the spring equivalent length, estimated as:

$$l_{eq} \approx \pi D' N_i \qquad (174)$$
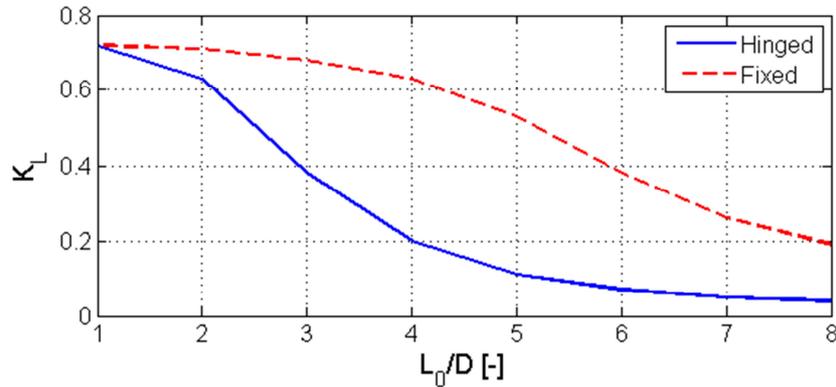
Figure 85: K_L behavior

12.3 Influence of the sizing inputs

As for the presented framework, there are a few input parameters to the sizing procedure which effect is not immediately predictable. In particular, while the effect of the sizing parameters of the spring (such as the number of effective coils) on the device are quite obvious, the influence of the poppet geometry, of the inlet port dimension and of the project point choice should be studied in more detail.

In this section we provide a few insights on this issues, in particular with regards to

- Influence of the inlet port diameter
- Influence of the Λ value used for the definition of the project point
- Influence of fluid temperature

The results provided in this section have been obtained for a cracking pressure $p^* = 100$ psi and a discharged flow rate in the project point equal to 100 l/min, while applying the sizing procedure described in Chapter 12.2. If not addressed diversely, results are obtained for $\alpha = 45°$.

\

For each of the selected values of Λ, the corresponding values of the inlet port diameter D can vary within a certain range. Admitting a maximum value of the pressure in the project point equal to 200 psi, we have the results reported in Fig. 86. The lower the diameter, the higher is the pressure in the project point, as shown in Fig. 87. In Fig. 88 is instead reported the behavior of the required spring stiffness in function of the Λ parameters and the project point pressure: it is possible to notice that the spring stiffness tends to obviously increase with the project point pressure and decrease with the Λ value. These behaviors can be explained by looking at Equations (124), (131) and (132). By combining those, we may wright

$$\begin{cases} Q = C_d(\alpha)A_h \sqrt{\dfrac{2(p - p_{out})}{\rho_{oil}}} \\ A_h = \left(\pi \dfrac{D^2}{4}\right)\Lambda \end{cases} \tag{175}$$

Considering α and Λ as a constant, neglecting p_{out} and reversing the equation we observe that the pressure in the project point is inversely proportional to the fourth power of D:

$$p = \left[\frac{Q}{C_d\left(\pi \dfrac{D^2}{4}\right)\Lambda}\right]^2 \frac{\rho_{oil}}{2} \tag{176}$$
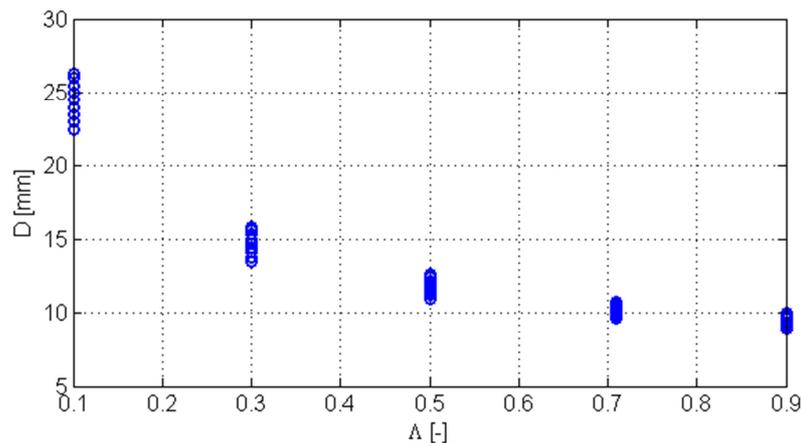
Figure 86: Inlet port diameter vs Λ - 45°
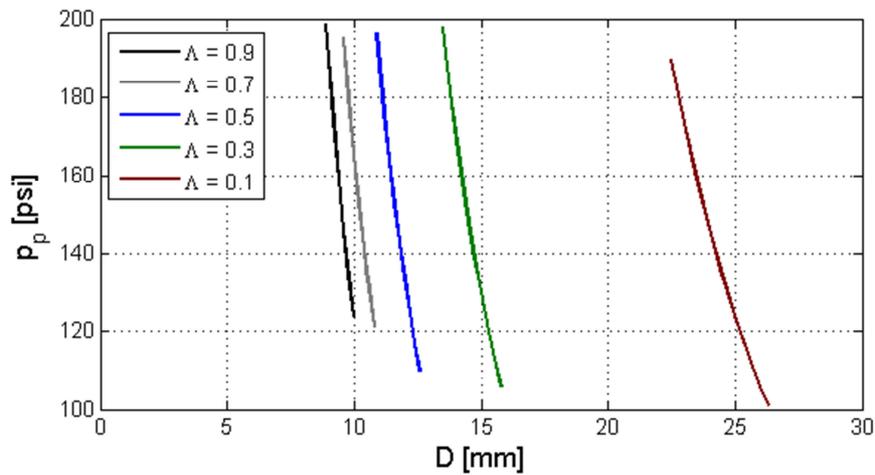
Figure 87: Fluid pressure at project point – 45°
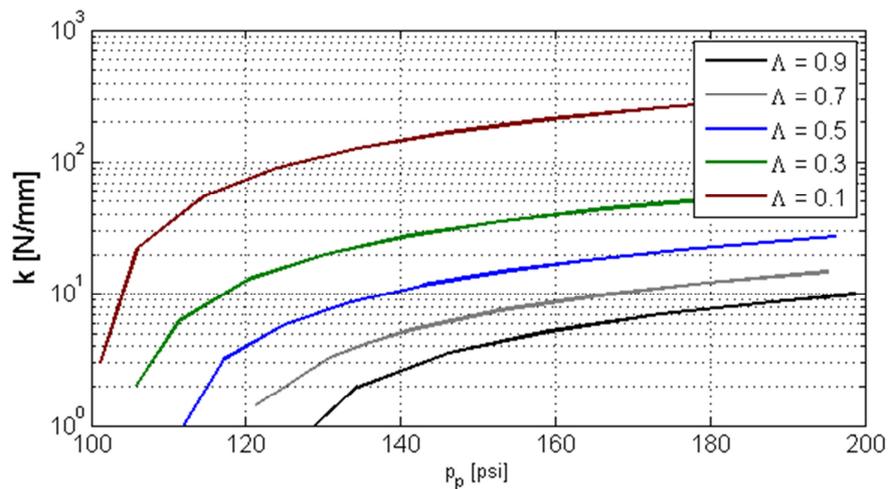
Figure 88: Required spring stiffness - 45°

The variation of the required stiffness determines some changes in the spring geometry and hence the variation of the volumetric envelop of the device. The behavior of the envelope is reported in Fig. 89. It is interesting to notice that there exists, for each value of Λ, a certain range of project point pressures that tends to minimize the spring size and hence the overall envelope. In particular, the position of this minimum tends to vary in such a way that the lower the Λ, the lower the pressure in the design point.

\
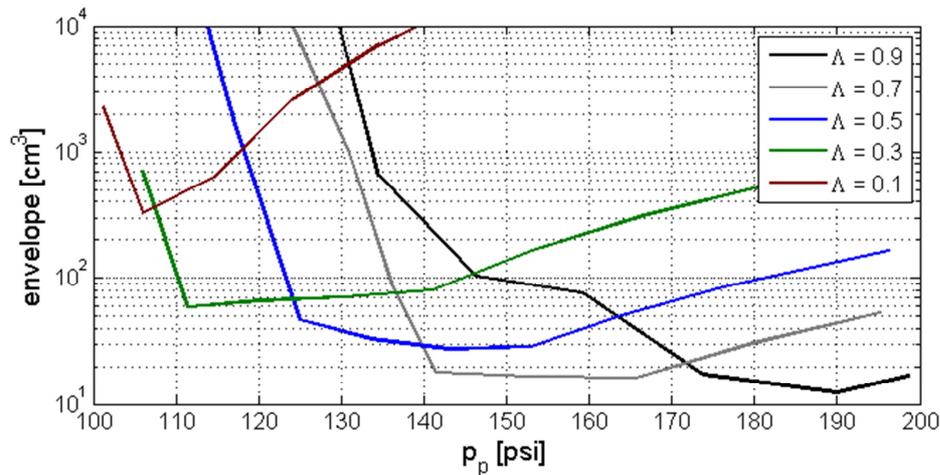
Figure 89: Estimated valve envelopes – 45°

The influence of the afore mentioned input parameters can be also studied observing the expected pressure-flow rate characteristics of the valve, that can be obtained by searching for the static equilibrium point for each given couple of fluid pressure and flow rate through the equations presented in Chapter 11. The analysis is performed using those input parameters able to minimize the projected envelope for each considered Λ. In this analysis we didn't consider the eventual presence of any end-stop to limit the maximum poppet lift under its value defined by the chosen Λ. Valves have been sized making reference to a lubricant oil adhering to the MIL-L-23699 standard and normally operating at 100°C. To observe the temperature influence over the valve behavior, their characteristics has been further obtained for a fluid temperature of -40°C. Results are reported in Fig. 90 and compared with the ideal case. From these results it is possible to notice how lower values of Λ better approximate the ideal case and tend to minimize the effect of the increase of the fluid viscosity due to temperature variations. This behavior can be observed because of two main reasons, that are the low stiffness of the spring and the significant portion of the poppet lift that can be used to open bigger metering areas in response to the increase of the fluid viscosity.
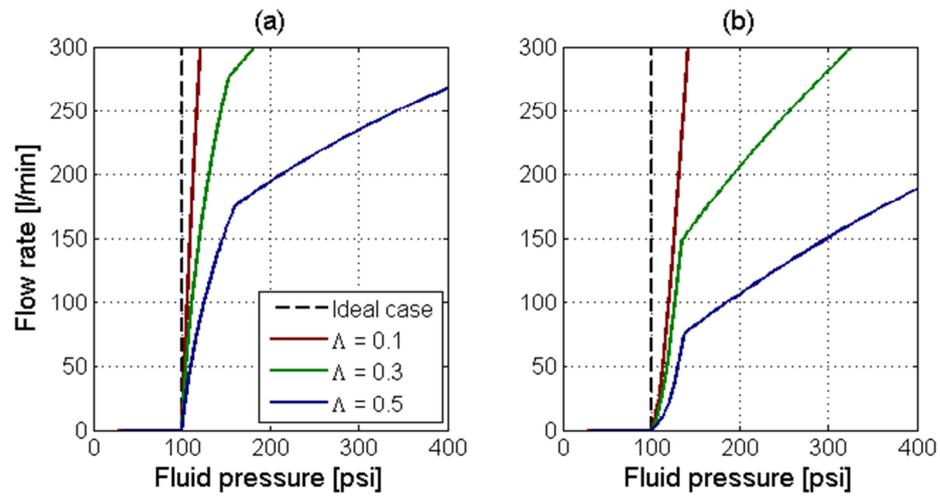
Figure 90: Valve characteristics: (a) 100 °C – (b) -40°C

\

Chapter 13

Conclusions

The main objective of the research programme was to provide a theoretical framework to help in the development of a novel gerotor pump for the lubrication of aeronautic engines. At first, the state of the art of gerotor pumps has been investigated to build a theoretical knowledge of the device and to position this pump type in the market. To do so, an in-depth benchmarking activity has been carried out through catalogues study and analytical comparisons based on dedicated simplified sizing tools. After highlighting the most common issues to be faced when designing low-pressure pumps, the major limitation of the traditional gerotor design have been emphasized and a few alternative solutions have been proposed, in particular the use of radial suction/delivery ports and the introduction of asymmetric teeth. To study the effects of these solutions, an Automatic Design and Simulation Framework has been prepared and developed; the framework is able to automatically design, validate and simulate a novel gerotor pump given a minimum number of geometrical and physical input parameters, outputting the rotors geometry and the projected performances. The study has been performed in a few consequent steps, that are a survey over the influence of ports configuration over the pump performances, a preliminary investigation over the effects of geometrical variations in the rotors' profiles and finally the optimization of the gears geometry. Through these steps, it was observed that the use of radial ports provides advantages in terms of maximum pump displacement while decreasing the probability of clogging due to ingress of external debris. Asymmetric teeth have instead proven to be effective in generating profiles able to conjugate between opposing performance requirements, such as wear rate, flow rate

irregularity and estimated rotors mass; more importantly, these improvements translates seeming less to both radial and axial ports configurations, making them effective also for more traditional design concepts.

In parallel, a side activity involving the study of a preliminary sizing tool for pressure relief valve has been performed. To prepare this tool, a lengthy CFD simulation campaign aimed at investigating the behavior of the valve discharge coefficient as a function of the poppet geometry and the fluid Reynolds' number has been performed; unfortunately, no experimental activities were planned, so that it was not possible to provide the validation of the proposed model. Finally, after addressing the most important sizing criteria, a new, automatic design tool for poppet relief valve has been prepared and discussed.

\

References

Adams, G., & Beard, J. E. (1997). Comparison of helical and skewed azis gerotor pumps. *Mechanism and Machine Theory 32 (6)*, 729-742.

Alotto, P. G., Eranda, C., Brandatter, B., Furnrtratt, G., Magele, C., Molinari, G., et al. (1998). Stochastic alorithms in electromagnetic optimization. *IEEE Transaction on Magnetics 34 (5)*, 3674-3684.

Archard, J. F. (1953). Contact and rubbing of flat surfaces. *Journal of Applied Physics 24*, 981-988.

Back, T., & Schwefel, H. P. (1993). *An Overview of Evolutioanry Algorithms for Parameters Optimization, Evolutionary Computation.* Cambridge, MA: MIT Press.

Bae, J. H., Kwak, H. S., San, S., & Kim, C. (2015). Design and CFD analysis of gerotor with multiple profiles (ellipse-involute-ellipse and 3 ellipses type) using rotation and translation algorithm. *Proceeding of the Institution of Mechanical Engineers, Part C; JMES.*

Beard, J. E., Hall, A. S., & Soedel, W. (1991). Comparison of hypotrochoidal and epitrochoidal gerotors. *Journal of Mechanical Design 113*, 133-141.

Beard, J. E., Yannitell, D. W., & Pennock, G. R. (1992). The effects of the generating pin size and placemen on the curvature and displacement of epitrochoidal gerotors. *Mechanism and Machine Theroy 27 (4)*, 373-389.

Bonadrini, G., Mimmi, G., & Rottenbacher, C. (2010). Theoretical analysis of an original rotary machine. *Journal of Mechanical Design 132 (2).*

Bonadrini, G., Mimmi, G., & Rottenbacher, C. (2012). Design and simulation of meshing of a particular internal rotary pump. *Mechanism and Machine Theory 49*, 104-116.

Borwn, F. W., Davidson, S. R., Hanes, D. B., & Weires, D. J. (2010). Analysis and testing of gears with asymmetric involute tooth form and optimized fillet form for potential application in helicopter main drives. *AGMA Technical Paper 10FTM14.*

Brennen, C. (1995). *Cavitation and Bubble Dynamics.* Oxford University Press.

Budynas, R. G., & Nisbett, J. K. (2014). *Shigley's Mechanical Engineering Design.* McGraw & Hill.

Budynas, R. G., & Nisbett, J. K. (2016). *Shigley's mechanical engineering design.* New York, NY: McGraw Hill.

Choi, T. H., Kim, M. S., Lee, G. S., Yung, S. Y., Bae, J. H., & Kim, C. (2012). Design of rotor for internal gear pump using cycloid and circular-arc curves. *Journal of Mechanical Design 134 (1).*

Colbourne, J. R. (1974). The geometry of trochoid envelopes and their applications in rotary pumps. *Mechanism and Machine Theory 9*, 421-435.

Deb, K., Agrawal, S., Pratap, A., & Meyarivan, T. (2000). A fast elitist nondominated sorting enetic algorithm for multi-objective optimization: NSGA-II. *Proceeding of the 6th international conference on parallel problem solving from nature.* Paris, France: Springer.

Demenego, A., Vecchiato, D., Litvin, F. L., Nervegna, N., & Mancò, S. (2002). Design and simulation of meshing of a cycloidal pump. *Mechanism and Machine Theory 37*, 311-332.

(1988). *DIN 17221.*

(1984). *DIN 17223.*

Fogel, D. B. (1995). *Evolutionary Computation.* New York: IEEE Press.

\

Fonseca, C. M., & Fleming, P. J. (1993). Multiobjective genetic algorithms. *IEEE colloquium on 'Genetic Algorithm for Control Systems Engineering'*. London, UK.

Franc, J. (2006). Physics and Control of Cavitation. In A.V., *Design and Analysis of High Speed Pumps.* NATO RTO Educational Notes.

Frosina, E., Senatore, A., Buono, D., Manganelli, M. U., & Olivetti, M. (2014). A Tridimensional CFD Analysis of the Oil Pump of an High Performance Motorbike Engine. *Energy Procedia 45*, 938-948.

Gamez-Montero, P. J., Castilla, R., Khamashta, M., & Codina, E. (2006). Contact problems of a trochoidal-gear pump. *Internation Journal of Mechanical Science 48*, 1471-1480.

Goldberg, D. E. (1989). *Genetic algorithms in search, optimization and machine learning.* Reading, MA: Addison-Wesley.

Higgins, P., & Crow, J. (1997). Advances in commercial engine lube debris monitoring. *SAE Technical Paper 972603*.

Holland, J. H. (1992). *Adaptation in Natural and Artificial Systems.* Cambridge, MA: MIT Press.

Hsieh, C. F. (2009). Influence of gerotor performance in veried geometrical design parameters. *Journal of Mechanical Design 134 (12)*.

Hsieh, C. F. (2012). Fluid and dynamic analyses of a gerotor pump using various span angle designgs. *Journal of Mechanical Design 134 (12)*.

Hsieh, C. F. (2015). Flow characteristics of gerotor pumps with novel variable clearance design. *ASME Journal of Fluids Engineering 137 (4)*.

Hsieh, C. F., Hwang, Y.-W., & Chang, Y. J. (2007). Geometric design for a gerotor pump with high area efficiency. *Journal of Mechanical Design 129*, 1269-1277.

Hwang, Y. W., & Hsieh, C. F. (2007). Determination of surface singularities of a cycloidal gear drive with inner meshing. *Mathematical and Computer Modelling 45*, 340-354.

Idelchik, I. E. (2005). *Handbook of hyraulic resistance.*

Inaguma, Y., & Hibi, A. (2005). Vane pump theory for mechanical efficiency. *Journal of Mechanical Engineering Science.*

Ippoliti, I., & Hendrick, P. (2013). Influence of the supply circuit on oil pump performance in an aircraft engine lubrication system. *Proceedings of ASME Turbo Expo 2013: Turbine Technical Conference and Exposition.* San Antonio, TX, USA.

Ivanovic, L., & Jositovic, D. (2006). Specific sliding of trochoidal gearing profile in the gerotor pumps. *FME Transactions 34 (3)*, 121-127.

Ivanovic, L., Devedzic, G., Cukovic, S., & Miric, N. (2012). Modeling of the meshing of the trochoidal profiles with clearances. *Journal of Mechanical Design 134 (4).*

Ivanovic, L., Devedzic, G., Miric, N., & Cukovic, S. (2010). Analysis of forces and moments in gerotor pumps. *Proceeding of the Institution of Mechanical Engineers, Part C: JMES 224 (10)*, 2257-2269.

Jae-Hun, K., Chul, K., & Chang, Y. J. (2006). Optimum design on lobe shapes of gerotor oil pump. *Journal of Mechanical Science and Technology 20 (9)*, 1390-1398.

Janikow, C. J., & Michalewicz, Z. (1991). An experimental comparison of binary and floating point representation in genetic algorithms. *Proceedings of the 4th International Conference on Genetic Algorithms*, (p. 31-36). Los Altos, CA.

Jelali, M., & Kroll, A. (2003). *Hydraulic servo-systems.* Springer.

Johnson, D. N., Edge, K. A., & Vaughan, N. D. (1991). Experimental investigation on flow and force characteristics of hydraulic poppet and disc valves. *Proceedings of the Institution of Mechanical Engineering, part A: Journal of Power and Energy 205.*

Johnson, D. N., Edge, K. A., & Vaughan, N. D. (1992). Numerical simulation of fluid in poppet valves. *Proceedings of the Institution of Mechanical Engineering, part A: Journal of Power and Energy 206.*

\

Johnson, K. L. (1985). *Contact Mechanics.* Cambridge, UK: Cambridge University Press.

Jung, S. Y., Han, S. M., Cho, H. Y., & Kim, C. (2009). Automated design system for a rotor with ellipse lobe profile. *Journal of Mechanical Science and Technology 23 (11)*, 2928-2937.

Karamooz Ravari, M. R., Forouzan, M. R., & Moosavi, H. (2012). Flow irregularity and wear optimization in epitrochoidal gerotor pumps. *Meccanica 47 (4)*, 9178-9928.

Kelner, V., & Léonard, O. (2004). Application of genetic algorithms to lubrication pump stacking design. *Journal of Computational and Applied Mathematics 168 (1-2)*, 255-265.

Kim, J. H., Kim, C., & Chang, Y. J. (2006). Optimum design on lobe shapes of gerotor oil pump. *Journal of Mechanical Science and Technologye 20 (9)*, 1390-1398.

Konak, A., Coit, D. W., & Smith, A. E. (2006). Multi-objective optimization using genetic algorithms: a tutorial. *Reliability Engineering and System Safety 91*, 992-1007.

Kwon, S., Kim, C., & Shin, J. (2011). Optimal rotor wear design in hypotrochoidal gear pump using genetic algorithm. *Journal of Central South University of Technology 18 (3)*, 718-725.

Kwon, S., Kim, M. S., & Shin, J. H. (2008). Analytical wear model of a gerotor pump without hydrodynamic effect. *Journal of Advanced Mechanical Design, Systems and Manufacturing 2*, 230-237.

Litvin, F. L., & Feng, P. H. (1996). Computerized design and generation of cycloidal gearings. *Mechanism and Machine Theory 31 (7)*, 891-911.

Litvin, F. L., Demenego, A., & Vecchiato, D. (2001). Formation by branches of envelope to parametric families of surface and curves. *Computer Methods in Applied Mechanics and Engineering 190 (35-36)*, 4587-4608.

Litving, F. L. (1989). *Theory of gearing.* Whashington D.C.: NASA.

Lizhen, H. (2004). Tooth profiles analysis for internal pump gear with straight line-conjugate curve profile. *Journal of Mechanical Transmission*.

Mancò, G., Mancò, S., Rundo, M., & Nervegna, N. (2000). Computerized generation of novel gearings for internal combustion engines lubricating pumps. *International Journal of Fluid Power 1*, 49-58.

Mancò, S., Nervegna, N., & Rundo, M. (2001). Crticial issues on performance of lubricating gerotor pumps at high rotational speed. *7th Scandinavian International Conference on Fluid Power*, (p. 23-38). Stockolm, Sweden.

Matuishi, M., & Endo, T. (1968). Fatigue of metals subjected to varying stress. *Japan Society of Mechanical Engineering*.

Meng, H. C., & Ludema, K. C. (1995). Wear models and predictive equations: their form and content. *Wear 181*, 443-457.

Metropolis, N., Rosenbluth, W., Teller, A. H., & Teller, E. (1955). Equation of state calculation by fast computing machines. *Journal of Chemical Physics 21 (6)*, 1087-1092.

Meyr, N., Cardé, C., Nitta, C., & Garas, D. (2002). Design and development of the 2002 UC Davis future truck. *SAE Technical Paper 2002-01-1210*.

Mimmi, G., & Pennacchi, P. (1997). Rotor design and optimization in internal lobe pumps. *Applied Mechanics Reviews 50*, 133-141.

Mimmi, G., & Pennacchi, P. (2000). Non-undercutting conditions in internal gears. *Mechanism and Machine Theory 35*, 477-490.

Muir, D., & Howe, B. (1996). In-line oil debris monitor (ODM) for the advanced tactical fighter engine. *Technology Showcase: Integrated Monitoring, Diagnostics and Failure Prevention*. Mobile, Alabama, USA.

Nervegna, N., & Rundo, M. (2016). *Fluid Power*. Torino: Politeko.

Niemann, G., Winter, H., & Hohn, B.-R. (2006). *Manuale degli organi delle macchine (in Italian)*. Hoepli.

\

Oshima, S. (1989). An experimental study on the several poppet valves with difference in shape. *Proceedings of the JFPS International Symposium on Fluid Power*.

Rabinowicz, E. (1965). *Friction and Wear of Materials.* Wiley.

Rechenberg, I. (1994). *Evolutionsstrategie 94.* Stuttgart, Germany: Fromman-Holzboog.

Rychlik, I. (1987). A new definition of the rainflow cycle counting method. *Internation Journal of Fatigue 9*, 119-121.

Schwefel, H. P. (1977). *Numerische Optimierung von Computer-Modellen mitels der Evolutionsstrategie.* Basel, Switzerland: Birkhaeuser.

Shung, J. B., & Pennock, G. R. (1994). Geometry for trochoidal-type machines with conjugate envelopes. *Mechanism and Machine Theory 29 (1)*, 25-42.

Singh, T. (1991). Design of vane pump suction porting to reduce cavitation at high operation speeds. *SAE Technical Paper 911937*.

Srinivas, N., & Deb, K. (1994). Multiobjective optimization using nondominated sorting in genetic algorithms. *Journal of Evolutionary Computation 2 (3)*, 221-248.

Stachowiak, G. W., & Batchelor, A. W. (2005). *Engineering Tribology.* Butterworth-Heinemann.

Steimes, J., Gruselle, F., & Hendrick, P. (2013). Study of an air-oil pump and separator solution for aero engine lubrication systems. *Proceedings of ASME Turbo Expo 2013: Turbine Technical Conference and Exposition.* San Antonio, Texas, USA.

Stone, J. A. (1960). Discharge coefficients and steady-state flow forces for hydraulic poppet valves. *Transactions of the American Society of Mechanical Engineers*.

Tallian, T. E. (1967). On competing failure modes in rolling contact. *ASLE Transactions 10*, 418-439.

Tauber, T. (1981). Full-flow debris monitoring in gas turbine engines. *ASME - GT - 60*.

Tong, S.-H., Yan, J., & Yang, D. C. (2009). Design of deviation function based gerotors. *Mechanism and Machine Theory 44 (8)*, 1595-1606.

U.S.Army. (1956). MIL-P-19131(SHIPS). *Pumps, Rotary, Power Driven, Miscellaneous*.

U.S.Army. (1994). MIL-L-23699E, Military Specification: Lubricating Oil, Aircraft Turbine Engine, Syntethic base, NATO Code Number O-156.

U.S.Army. (1997). MIL-PRF-62180D(AT). *Semitrailer, Fuel Tankers: 5000 Gallon, Bulkhaul, Automotive and Aircraft Fuel Servicing*.

U.S.Army. (2004). DOD-PRF-85734A. *Lubricating Oil, Helicopter Transmission System, Synthetic Base*.

U.S.Army. (2011). Aviation Critical Safety Item Management Handbook. *NAVAIR Public Release 11-515*.

U.S.Army. (2014). MIL-PRF-32080F. *Truck, Aircraft Fueling-Defueling, 6000 Gallon, A/S32R-11*.

Urata, E. (1969). Thrust of poppet valve. *Bulletin of the JSME 12*.

Vecchiato, D., Demenego, A., Argyris, J., & Litvin, F. L. (2001). Geometry of a cycloidal pump. *Computer Methods in Applied Mechanics and Engingeering 190*, 2309-2330.

Vecchiato, D., Demenego, A., Argyris, J., & Litvin, F. L. (2001). Geometry of a cycolidal pump. *Computer Methods in Applied Mechanics and Engineering 190*, 2309-2330.

Viersma, T. J. (1980). *Analysis, synthesis and design of hydraulic servosystems and pipelines*. Elsevier.

Von Mises, R. (1917). Berechnung von Ausfluss - und - Uberfallzahlin. *VDI 17*.

Weixiang, S., Binggang, C., & Zhiyong, T. (1993). Review and progress of a poppet valve. *Fluid Power*.

\

Williams, J. A. (1999). Wea modelling: analytical, computational and mapping: a continuum mechanics approach. *Wear 225*, 1-17.

Xu, X. Z., & Song, T. (2008). Analysis of flow characteristics of gear pump with straight line conjugate curve profile. *Coal Mine Machinery*.

Xu, X., & Song, T. L. (2007). Optimization design of internal gear pump with straight line conjugate curve profile. *Journal of Mechanical Transmission*.

Yan, J., Tong, S.-H., & Yang, D. C. (2007). A new gerotor design method with switch angle assignability. *10th ASME International Power Transmission and Gearing Conference*.

Yan, J., Yang, D. C., & Tong, S.-H. (2009). On the generation of analytical noncircular multilobe internal pitch curves. *Journal of Mechanical Design 130 (9)*.

Yang, D. C., Yan, J., & Tong, S.-H. (2010). Flowrate formulation of deviation function based gerotor pumps. *Journal of Mechanical Design 132 (6)*.

Yung, S. Y., Bae, J. H., Kim, M. S., & Kim, C. (2011). Development of new gerotor oil pumps with multiple profiles. *International Journal of Precision Engineering and Manufacturing 12 (5)*, 835-841.